

Quantifying the C/O Ratio in the Planet-forming Environments around Very Low Mass stars

JAVIERA K. DÍAZ-BERRÍOS ¹, CATHERINE WALSH ¹, AND EWINE F. VAN DISHOECK ^{2,3}

¹*School of Physics and Astronomy, University of Leeds, Leeds, LS2 9JT, UK*

²*Leiden Observatory, Leiden University, P. O. Box 9513, 2300 RA Leiden, The Netherlands*

³*Max-Planck Institut für Extraterrestrische Physik (MPE), Giessenbachstrasse 1, 85748, Garching, Germany*

(Received February 18, 2025; Revised February 5, 2026; Accepted February 5, 2026)

ABSTRACT

The material in planet-forming disks determines the composition of planets; hence, it is crucial to understand the physical and chemical processes that set the abundance and distribution of key volatiles. James Webb Space Telescope observations of disks around very low mass ($\sim 0.1 M_{\odot}$) stars (VLMSs) have revealed their hydrocarbon-rich inner regions (e.g., C_2H_2), with column densities significantly higher than predicted. We employ chemical kinetics models using the physical structure of the inner disk around an M dwarf star with an X-ray luminosity of $L_X \sim 10^{29}$ erg s⁻¹. We adopt initial abundances that mimic the effects of carbon enhancement and oxygen depletion (C/O from 0.44 to 87.47) and quantify how the abundances and distributions of key volatiles respond. The column density and number of molecules (\mathcal{N}) of hydrocarbons and oxygen-bearing species are highly sensitive to the C/O ratio, with the largest increases in hydrocarbons occurring when carbon increases by a factor of 2, and/or oxygen decreases by a factor of 10, relative to solar. In the IR-emitting region ($T_{\text{gas}} > 200$ K), a range of C/O ratios can reproduce the observed \mathcal{N} and ratios relative to CO_2 . The disk-integrated molecular ratio with respect to CO_2 is highly sensitive to the underlying C/O ratio. However, our results apply only to a source with a single X-ray luminosity value at the middle of that observed for VLMSs; hence, a degeneracy between the stellar L_X and the C/O ratio cannot be discarded. Nonetheless, our findings support that an enhanced C/O is required to drive the hydrocarbon-rich chemistry observed in the inner disks around VLMSs.

Keywords: Astrochemistry — Protoplanetary disks — ISM: molecules

1. INTRODUCTION

As the most populous stars, M dwarf stars are likely the most common hosts of exoplanets (e.g., Henry & Jao 2024). Thus, the protoplanetary disks around these very low mass stars (VLMSs) are interesting targets. In particular, studying the distribution and abundance of different species reveals the composition of the material available to form planets, and understanding the chemical processes dominating and controlling the detected abundances can illuminate the physics taking place within the planet-forming regions of these sources (e.g., Öberg et al. 2023).

The inner disk (less than a few au), characterized by its high densities and temperatures, is where terrestrial planets form (Dullemond & Monnier 2010). Important results characterizing the inner disk came from previous works using the Spitzer Space Telescope. Studies such as those by Salyk et al. (2008), Pontoppidan et al.

(2010), and Carr & Najita (2008, 2011) reported detections of OH, CO_2 , HCN, C_2H_2 , and H_2O emission in the innermost disk regions around T Tauri stars, indicating that the inner disk is a chemically rich environment for planet formation (see Pontoppidan et al. 2014 for review). However, these results are not only applicable to T Tauri stars. Pascucci et al. (2013) reported the detection of HCN and C_2H_2 (as well as CO_2 and H_2O) toward disks around M dwarf and brown dwarf stars, suggesting that the inner regions of disks around VLMSs are particularly rich in hydrocarbon species. In summary, observations of the inner disk with Spitzer gave us the first indicators of the rich chemistry in the inner disk and revealed the abundances of key carriers of important elements (O, C, and N) for planet formation.

Recent James Webb Space Telescope (JWST) observations have confirmed the results suggested by Spitzer, but have also provided new insights about the rich

chemical environment that is the inner region of planet-forming disks (Kamp et al. 2023). Water was previously detected in the inner regions of disks by Spitzer and thanks to the higher spectral resolution of JWST, it is now possible to study the water reservoirs in disks in more detail. These studies have focused on the water enrichment within the water snowline and its relation to the presence of substructures (Banzatti et al. 2017; Kalyaan et al. 2021; Banzatti et al. 2023; Kalyaan et al. 2023; Gasman et al. 2023; Temmink et al. 2025). Other studies, such as those by Grant et al. (2023) and Vlasblom et al. (2024), have focused on the structure of the inner disk. Grant et al. (2023) presented JWST observations of the disk around a low-mass T Tauri star, detecting $^{12}\text{CO}_2$, $^{13}\text{CO}_2$, H_2O , HCN , C_2H_2 , and OH emission. In addition, a high $\text{CO}_2/\text{H}_2\text{O}$ ratio was derived, suggesting not only a chemically rich inner disk but also a structured one (Grant et al. 2023; Vlasblom et al. 2024). These studies show how spatially unresolved observations of molecular line emission with JWST can reveal the presence of structure in the inner regions of planet-forming disks.

JWST has also enabled the increased detection of carbon-bearing species in inner-disk regions. Previous studies using Spitzer reported the detection of CO , CO_2 , and C_2H_2 (Salyk et al. 2008; Pascucci et al. 2013; Carr & Najita 2011), which are thought to constitute the most abundant carbon carriers. JWST has also allowed the first detection of additional, and more complex, hydrocarbon species such as C_4H_2 , C_6H_6 , C_2H_4 , and C_3H_4 toward several disks around VLMSs, indicating that the inner-disk region may be carbon-rich (Tabone et al. 2023; Arabhavi et al. 2024; Kanwar et al. 2024b; Kaeufer et al. 2024).

Motivated by the Spitzer results, Walsh et al. (2015) investigated the chemical composition of the inner planet-forming regions of disks for a range of stellar spectral types: M dwarf, T Tauri, and Herbig Ae. They concluded that the inner-disk region is influenced by the relative UV and X-ray luminosities of the stars, i.e., the photochemistry and X-ray chemistry play an important role in setting the chemical composition. Walsh et al. (2015) suggested that a higher abundance of hydrocarbons is expected in disks around low-mass stars since the inner regions of disks around cooler stars (i.e., M dwarf stars) are more carbon-rich owing to the release of carbon from CO via X-ray-induced processes. However, these models did not predict the large column densities of all the hydrocarbons reported in very recent work by Tabone et al. (2023), Arabhavi et al. (2024), Kanwar et al. (2024b), and Kaeufer et al. (2024), with one reason being that those models assumed the solar abundance

of C and O, i.e., oxygen-rich conditions. Kanwar et al. (2024b) and Colmenares et al. (2024) support this idea, suggesting that a higher-than-solar C/O ratio could explain the high abundance of hydrocarbons in the disks around the low-mass star Sz28 and the low accretion rate ($\sim 10^{-10} M_\odot \text{ yr}^{-1}$) T Tauri star DoAr 33 (Cieza et al. 2010), respectively.

In a recent study, Raul et al. (2025) found that the abundance of hydrocarbons has a strong dependence on the mechanisms that lead to an X-ray- or UV-driven chemistry, suggesting that X-ray-dominated chemistry can result in a higher production of C_2H_2 , CO , HCN , and long carbon chains (LCCs), similar to the conclusions reached by Walsh et al. (2015). Raul et al. (2025) also suggest that hydrocarbons such as C_2H_2 are more abundant in a water-rich disk, while species such as CH_4 and CH_3 reach higher abundances in a disk where the water is depleted. Other studies, such as Sellek & van Dishoeck (2025), have found that the destruction of gas-phase CO can deplete oxygen while producing hydrocarbons to explain observations, indicating a high C/O ratio. Kanwar et al. (2026) modeled the disk structure of J160532, testing the effect of variation in the C/O ratio, and found that the presence of a gap better explains the observations. Houge et al. (2025) studied the effect of the variation in C/H and C/O ratios, finding that the thermal decomposition process of refractory organics allows the carbon-rich gas to survive throughout the disk and over time. Given that each of the models discussed so far uses a distinct chemical network, cross-checks of the main results with an independent chemical network are warranted. More recently, the survey of 10 VLMS disks by Arabhavi et al. (2025a) showed that high columns of hydrocarbon molecules are common. In addition, Grant et al. (2025) found an anticorrelation between the flux ratio of $\text{C}_2\text{H}_2/\text{H}_2\text{O}$ and the stellar luminosity, with disks around VLMSs showing a spectra dominated by C_2H_2 emission.

In light of the hydrocarbon-rich inner disks around VLMSs revealed by JWST, we revisit the M dwarf models of Walsh et al. (2015) to quantify the changes in chemical structure and abundances expected for cases where we have an increased relative abundance of carbon to oxygen. We compare the predicted abundances, column densities, total number of molecules, and molecular ratios of the key species observed in the inner regions of protoplanetary disks, paying special attention to those reported by Tabone et al. (2023), Arabhavi et al. (2024), Kanwar et al. (2024b), and Arabhavi et al. (2025b). We investigate possible explanations for the high column densities of hydrocarbons detected around VLMSs reported in the listed works. We focus solely

on the response of the chemistry and trends in composition to variations in C/O ratio for a generic model of a disk around an M dwarf star, i.e., we do not aim to reproduce absolutely the observations toward any specific source. Note that in this work we test a wide range of C/O ratio values, investigating carbon enrichment, oxygen depletion, and the combination of both.

Section 2 describes the chemical model used, including the chemical network. Section 3 presents the results from the different scenarios investigated. In Section 4 we analyze the results, compare the different cases, and identify trends. We also compare these trends with the results from Tabone et al. (2023), Arabhavi et al. (2024), and Kanwar et al. (2024b) and present possible explanations for the observed trends. Finally, Section 5 presents a summary of the key points and the conclusions of this work.

2. DISK MODEL

In this section, we describe the physical model and chemical network used. We also include details about the parameters adopted in the different models used to motivate the initial abundances that mimic the proposed physical mechanisms responsible for the high abundance of hydrocarbons in the inner disks around VLMSs.

2.1. Physical Model

We use the physical structure for a disk of mass $0.6 M_{\text{Jup}}$ and radius 10 au around an M dwarf star from Walsh et al. (2015), which is calculated using the methods from Nomura & Millar (2005) with the addition of X-ray heating as outlined in Nomura et al. (2007). Here we outline the most important parameters of the system only, and we refer to Walsh et al. (2015) for further details on the disk physical model. The star-disk system properties can be found in Table 1. The radiation field of the star (with mass and radius of $0.1 M_{\odot}$ and $0.7 R_{\odot}$, respectively) is simulated as a blackbody at the stellar effective temperature (3000 K). UV excess emission is included, which has two components: a diluted blackbody spectrum to simulate bremsstrahlung emission ($T_{\text{br}} \sim 25,000$ K) and Ly α line emission (see Fig. 1 in Walsh et al. 2015). We assume that the X-ray luminosity of the star is $L_X \sim 10^{29}$ erg s $^{-1}$, which is at the middle of the observed values for VLMSs (e.g., Preibisch & Feigelson 2005). The far-UV flux through the disk has contributions from both the star and interstellar medium and is calculated over the range $6 \text{ eV} < h\nu < 13 \text{ eV}$ (Nomura & Millar 2005). The dust grain size distribution adopted is that which reproduces the extinction curve observed in dense clouds (Weingartner & Draine 2001). Additionally, we assume that

Table 1. Physical model parameters

Parameter	Description	Value
M_{\star}	Stellar mass	$0.1 M_{\odot}$
R_{\star}	Stellar radius	$0.7 R_{\odot}$
T_{\star}	Effective temperature	3000 K
\dot{M}	Accretion mass rate	$10^{-9} M_{\odot} \text{ yr}^{-1}$
$\Sigma_{0.04\text{au}}$	Surface density at 0.04 au	$1.9 \times 10^{25} \text{ cm}^{-2}$
$\Sigma_{10\text{au}}$	Surface density at 10 au	$3.0 \times 10^{23} \text{ cm}^{-2}$
$M_{\text{disk},10 \text{ au}}$	Disk mass out to 10 au	$0.6 M_{\text{Jup}}$

NOTE—Star-disk system physical properties (Walsh et al. 2015).

the gas and small dust grains are fully mixed. The gas temperature is calculated assuming thermal balance between the heating and cooling of the gas. The initial abundances assumed to compute the gas temperature for carbon and oxygen were 7.86×10^{-5} and 1.8×10^{-4} , respectively, which are the same as those used by Nomura & Millar (2005) and Walsh et al. (2015).

Figure 1 shows the gas density (cm $^{-3}$), gas and dust temperature (K), UV and X-ray fluxes (erg cm $^{-2}$ s $^{-1}$), and total ionization rate (s $^{-1}$) for the M dwarf disk model. The ionization rate includes contributions from X-rays and cosmic rays. The cosmic-ray ionization rate adopted is 1×10^{-17} s $^{-1}$. The model follows the common protoplanetary physical structure; the gas temperature and density show a radial and vertical gradient with cooler temperatures near the midplane and in the outer disk ($\sim 50 - 500$ K), and higher densities near the midplane and close to the star ($\sim 10^9 - 10^{13}$ cm $^{-3}$). Note that the disk structure used in our model includes accretion heating, which produces a temperature inversion in the midplane (for further discussion see Appendix A). The dust temperature follows a similar gradient to the gas temperature but with lower temperatures in the disk atmosphere due to inefficient cooling of the gas in this region. The UV and X-ray fluxes are set by the surface density of the disk and the relative penetration strengths of UV and X-ray photons. Note that the more energetic X-rays are able to penetrate to greater depths toward the disk midplane such that the X-ray flux is larger than that for UV photons at $z/r \sim 0.1 - 0.2$ and is an important driver of chemistry in this region.

2.2. Chemical Network

The disk model uses the RATE12 version of the UMIST Database for Astrochemistry (UDfA) chemical network,

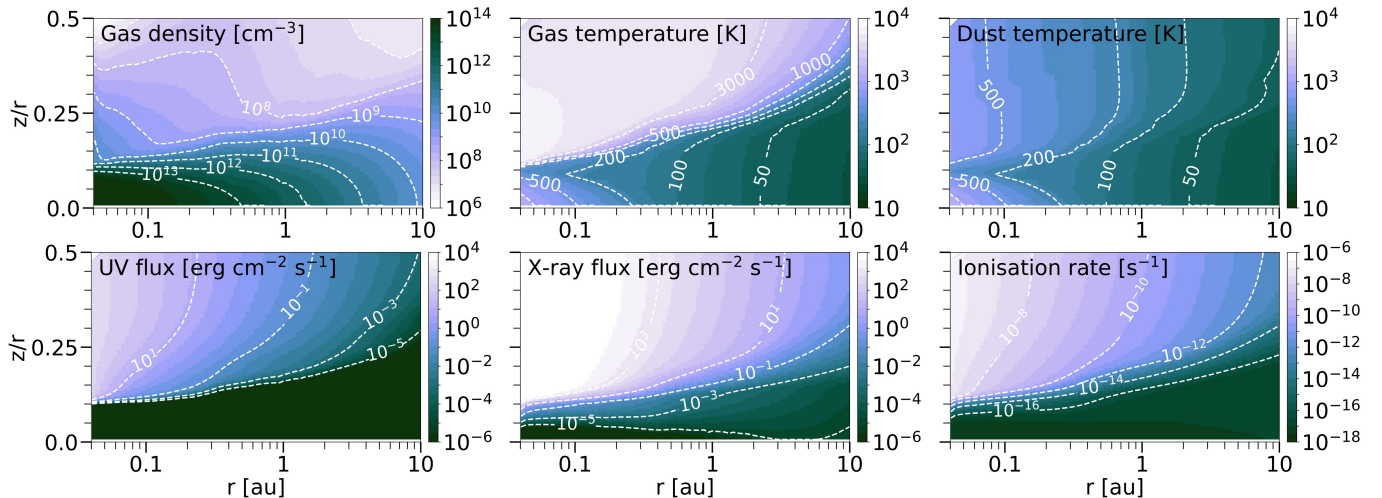


Figure 1. Physical structure of the M dwarf disk model used in this work, which is the same as that used in Walsh et al. (2015). Presented are the gas density, gas temperature, and dust temperature (top row) and the UV flux, X-ray flux, and total ionization rate (bottom row). Each panel shows the dependence of each parameter as a function of disk radius (up to 10 au) and disk height (scaled by the radius; z/r). White contours on each panel represent the same information as the color bar. For ease of comparison, the gas and dust temperatures, as well as the UV and X-ray fluxes, share the same color scales.

which includes 6173 gas-phase reactions involving 467 species (McElroy et al. 2013). The gas-phase network includes two-body reactions, direct cosmic-ray ionization, cosmic-ray-induced photodissociation and ionization, photodissociation and photoionization, direct X-ray ionization, and X-ray-induced ionization and dissociation. This network is supplemented with additional dissociative recombination reactions and photoreactions, collisional dissociation reactions, and three-body reactions necessary because of the higher densities and temperatures in the inner disk. Also included are reactions with excited H_2 which are important for setting the composition in the hot atmosphere of the inner disk (Bruderer 2013). Gas-grain chemistry is also included, allowing freeze-out to form ices and thermal and non-thermal desorption for release back into the gas phase. A grain-surface chemical network is included with all associated reactions taken from the OSU2008 database (Garrod et al. 2008). Additional glyoxal ($(HCO)_2$) reactions are adopted from Woods et al. (2013). The Langmuir-Hinshelwood mechanism is assumed to set the grain-surface reaction rates. Table 2 presents the binding energies that we adopt for species of interest in this study.

2.3. Initial Abundances

We use the same initial abundances adopted in Walsh et al. (2015) as our fiducial model (M0.44F). This model has a C/O ratio of ~ 0.44 , and C/H and O/H ratios of 1.4×10^{-4} (Cardelli et al. 1996) and 3.2×10^{-4} (Meyer et al. 1998), respectively (see Table 3). We also as-

Table 2. Binding energies for key species

Species	E_{bind} [K]	Species	E_{bind} [K]
C_2H_2	2090	OH	3210
CH_4	1252	CO	855
C_6H_6	7587	CO_2	2267
CH_3	1040	H_2O	4880
C_4H_2	4187	HCN	3610
C_2H_4	2010	NH_3	2715
C_3H_4	4287	HC_3N	4580
C_2H_6	2320	N_2	790

NOTE—Binding energies used here are mostly from the compilations by Penteado et al. (2017) and McElroy et al. (2013). We adopt the values for CO, N_2 , and HCN from the experimental work by Öberg et al. (2005) and Noble et al. (2013).

sume that He/H and N/H have values of 9.75×10^{-2} and 7.5×10^{-5} , respectively (Meyer 1985; Cardelli et al. 1991). To generate the suite of initial abundances for the disk model, we run a dark cloud model with $T_{\text{gas}} = T_{\text{dust}} = 10$ K, $n_{\text{gas}} = 10^4$ cm^{-3} , and $A_v = 10$ mag, and adopt the abundances at a time of 3.2×10^5 yrs. The initial atomic abundances used for the dark cloud model are the low-metallicity (i.e., depleted) values from Graedel et al. (1982) for a diffuse cloud. Thus, we begin our disk chemical model with molecular material and interstellar abundances of ice species, thus mimicking the

scenario where the disk has inherited interstellar material. Whilst the chemistry through much of the inner disk is expected to be at or close to steady state, this is not true for the colder midplane, where ice formation can be efficient (Eistrup et al. 2016).

To investigate different scenarios for the observed high abundances of hydrocarbons in the inner regions of VLMSs, we then run variations of the model in which we modify our initial abundances by increasing the carbon abundance (C/H) and/or decreasing the oxygen abundance (O/H). This is done to mimic elemental redistribution that might take place within the disk following the dark cloud stage. To increase C/H, we simply add additional carbon to the initial atomic carbon abundance, increasing that adopted in the fiducial model. On the other hand, when decreasing oxygen, we homogeneously deplete all oxygen-bearing species by the stated factor. Because this also depletes any species with both carbon and oxygen, we set the final C/O ratio by adding any depleted carbon to the initial atomic carbon abundance. This leads to the final C/H, O/H, and thus C/O ratios shown in Table 3. Note that rounding errors are responsible for small variations in C/H and O/H across models.

The scenarios that we explore are the following and are based on those proposed by Tabone et al. (2023), van Dishoeck et al. (2023), and Arabhavi et al. (2024).

- (i) *Carbon grain destruction releasing carbon into the gas phase.* We mimic this by increasing the elemental carbon abundance everywhere in the disk by a factor of 2.
- (ii) *Oxygen depletion due to icy pebble trapping in the outer disk.* To mimic this, we retain the fiducial carbon elemental abundance and decrease the oxygen abundance everywhere in the disk by factors of 10 and 100.
- (iii) *Carbon enrichment and oxygen depletion.* To simulate the combined case, we increase the carbon elemental abundance by a factor of 2 and decrease the oxygen abundance everywhere by factors of 10 and 100.

In the first case, the choice of the factor of 2 was based on Wei et al. (2019) and Asplund et al. (2021). In Wei et al. (2019) they simulated the effects of carbon grain destruction in disks by increasing the elemental abundance of carbon from 7.30×10^{-5} (the abundance in diffuse clouds; Woodall et al. 2007) to 2.95×10^{-4} which is the solar abundance of carbon (Asplund et al. 2009). As we have adopted more recent estimates for the carbon abundance as measured in the diffuse interstellar

medium, this translates to increasing the carbon abundance by a factor of ~ 2 for our model when using the updated solar C/H reported by Asplund et al. (2021), 2.88×10^{-4} . This is considered an extreme case that assumes that all the carbon in the grains has been destroyed and released into the gas phase. The oxygen depletion factor in the disk has a broader range of values motivated by the depletion factors proposed for water and CO in the outer disks of nearby stars (e.g., Schwarz et al. 2016; Du et al. 2017; Zhang et al. 2021). See Section 4.6 for further discussion on physical scenarios that can (re)set the C/O ratio in disks. We adopt two levels of oxygen depletion: 10 and 100. Table 3 shows the different models we investigated with the model names used in this work. Note that hereafter we also refer to the models as carbon-poor/rich or oxygen-poor/rich. This criterion is based on the C/O ratio being higher than or lower than 1 (i.e., carbon-rich means $C/O > 1$). We extract and analyze the abundances at a time of 10^6 yr.

3. RESULTS

3.1. Abundance maps and column density profiles

Figures 2, 4, 5, and 6 present the fractional abundance with respect to the gas number density, n_{gas} , ($n(X)/n_{\text{gas}}$), as a function of disk radius, r , and height/radius, z/r , for the different carbon and oxygen initial abundances (see Table 3). We present vertical distributions in Appendix B. Figures B.1, B.2, B.3, and B.4 present the ionization rate, gas temperature, and number density of the same set of molecules as a function of height at radii of 0.1 and 1 au.

We focus here on a set of hydrocarbons (C_2H_2 , CH_4 , C_6H_6 , CH_3 , C_4H_2 , C_2H_4 , C_3H_4 , and C_2H_6), oxygen- (OH, CO, CO_2 , H_2O) and nitrogen-bearing species (HCN , NH_3 , HC_3N , and N_2). These species either have been previously detected in the inner region of protoplanetary disks (Najita et al. 2003; Salyk et al. 2008; Pontoppidan et al. 2010; Carr & Najita 2008, 2011; Pascucci et al. 2013; Tabone et al. 2023; Banzatti et al. 2023; Arabhavi et al. 2024; Kanwar et al. 2024b; Kaeufer et al. 2024; Colmenares et al. 2024) or are considered to be key carriers of carbon, oxygen, and nitrogen (Walsh et al. 2015). Figure 3 shows the column densities as a function of disk radius, r , for the same set of species, for all six models. We show the column density integrated down to either the $\tau = 1$ surface at $14 \mu\text{m}$ or where the gas temperature reaches 200 K. This is what we define as the IR-emitting region, where the temperature boundary is consistent with the lowest excitation tempera-

Table 3. Initial abundances and models

Model	Description	C/O ratio	C/H	O/H
M0.44F	Fiducial model ^a	0.44	1.4×10^{-4}	3.2×10^{-4}
M0.88C	↑ C × 2	0.87	2.8×10^{-4}	3.2×10^{-4}
M4.4	↓ O × 10	4.37	1.5×10^{-4}	3.3×10^{-5}
M8.8C	↑ C × 2 ↓ O × 10	8.75	2.9×10^{-4}	3.3×10^{-5}
M44	↓ O × 100	43.72	1.5×10^{-4}	3.3×10^{-6}
M88C	↑ C × 2 ↓ O × 100	87.47	2.9×10^{-4}	3.3×10^{-6}

^aSame initial abundances used in [Walsh et al. \(2015\)](#).

NOTE—Initial abundances for the different models. The up and down arrows represent enrichment and depletion, respectively. All of the initial abundances were made with respect to the fiducial model M0.44F.

ture derived for molecules from observations with JWST (e.g., [Tabone et al. 2023](#); [Arabhavi et al. 2024](#); [Kanwar et al. 2024b](#); [Arabhavi et al. 2025b](#); [Arulanantham et al. 2025](#)). The adoption of this temperature boundary may slightly underestimate the number of molecules in the IR-emitting region for the case in which the reported excitation temperatures are an average over a distribution. We discuss the implications of this assumption in Section 4.2. For interest, versions of the same figure integrated down to the $\tau = 1$ surface at $14 \mu\text{m}$ and to the midplane are available online.

Different species have different distributions through the disk, and their abundances can vary radially and vertically, which can affect the radial column density distributions. However, there is a general abundance map pattern for most species with two primary reservoirs: one reservoir in the disk atmosphere at elevated $z/r \gtrsim 0.1$ and generally elevated temperature $\gtrsim 300$ K, and a second in the inner-disk midplane $z/r \lesssim 0.1$. The specific region where the species resides will depend on what physical properties determine the appropriate conditions for its formation. The radial extent of this midplane reservoir is dependent on the volatility of the molecule (more volatile species will generally have a greater radial extent) and whether or not efficient gas-phase synthesis is possible in the shielded midplane region. Exceptions to this pattern are the small radicals CH_3 and OH , which are only abundant in the disk atmosphere (see Figs. 2 and 5), and the hypervolatile species CO and N_2 , which have a wider distribution through the disk, as they are depleted onto dust grains at low temperatures only ($\lesssim 20$ K; see Figs. 1, 2, and 6). As another volatile species, CH_4 also has a more widespread distribution through the disk than most other hydrocarbons, e.g., C_2H_2 (see Fig. 2). CO_2 also has a slightly different distribution in that its molecular layer in the disk atmosphere lies at slightly lower temperatures ($\gtrsim 50$ K)

than most other species considered here (see Fig. 5). These general abundance patterns are reflected in the column density profiles and vertical distributions (see Appendix B).

In the next subsections, we discuss how the abundance and distribution of each member of each family of species considered here (hydrocarbons, O-bearing, and N-bearing) respond to the imposed variations in the global C/O ratio. A more detailed description for each hydrocarbon species is available in Appendix C, with the exception of CH_4 and CH_3 which have different distributions than the other hydrocarbons.

3.1.1. Hydrocarbons

We find that most hydrocarbons are abundant in the atmosphere between 300 and 4000 K. The upper boundary in the distribution of hydrocarbons (around 4000 K) is mainly determined by the gas temperature (see Figs. 1, 2, and 4) and is controlled by neutral-neutral and ion-molecule reactions (e.g., [Walsh et al. 2015](#); [Kanwar et al. 2024a](#)). This is true for both carbon-poor and carbon-rich scenarios. On the other hand, the lower boundary (around 300 K) is determined by different physical properties depending on the C/O ratio value. This boundary moves to lower heights in the disk for some species and models; however, in most of those cases, the abundance reached toward the boundary is at least one order of magnitude lower than that in the peak abundance region. For species such as C_6H_6 and C_4H_2 in the fiducial model, the lower boundary is shaped by gas temperatures higher than 200 K (~ 500 K). The upper boundary of the peak abundance region in the disk atmosphere for all the species mentioned is shaped by the gas temperature, X-ray flux, UV flux, and ionization rate depending on the radius and height. For C_2H_4 and C_2H_6 , gas temperatures lower than 3000 K (~ 1000) shape the upper boundary. For $\text{C/O} < 1$, the

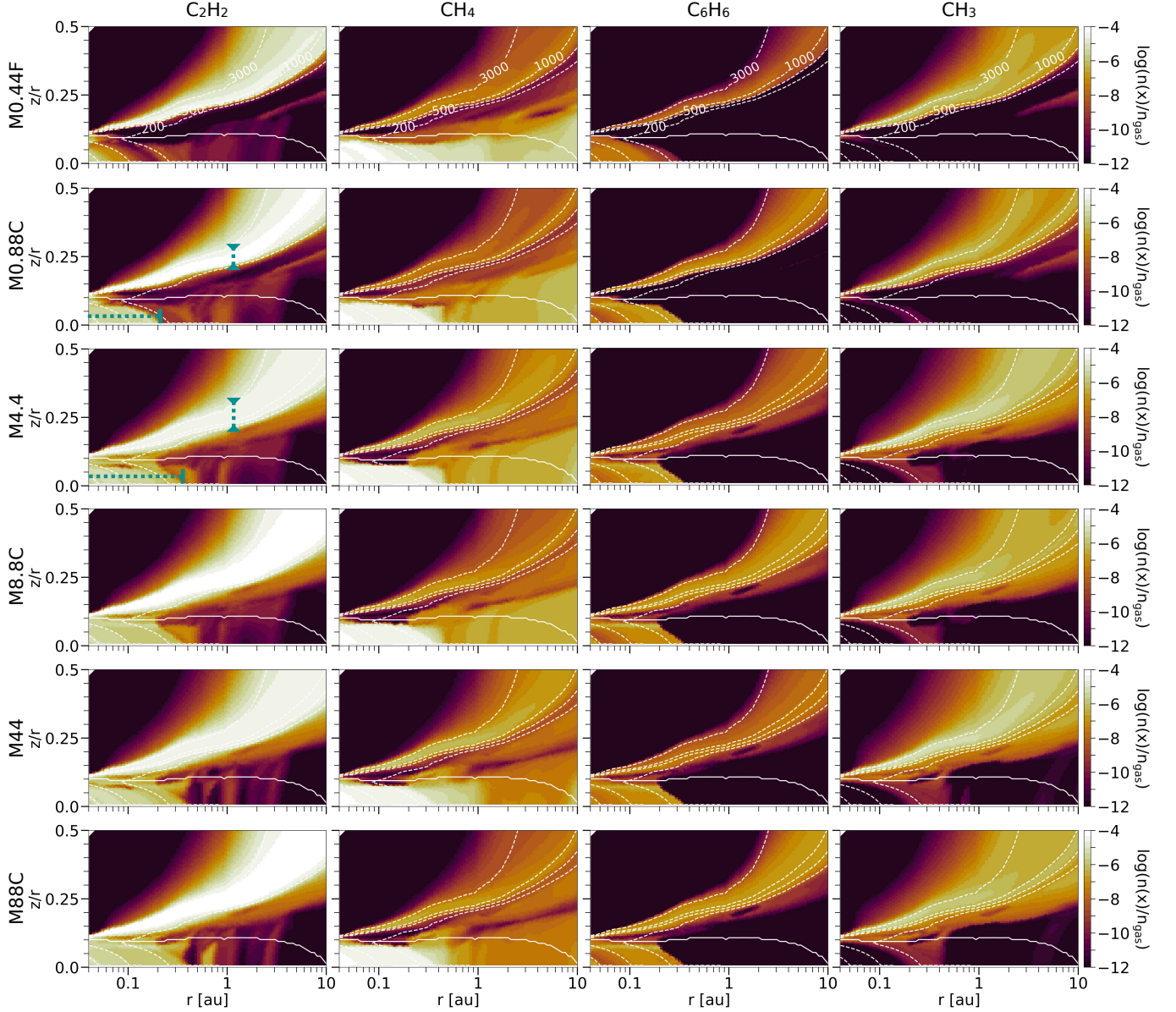


Figure 2. Fractional abundance with respect to the gas number density n_{gas} of the carbon-bearing species (hydrocarbons), C_2H_2 , CH_4 , C_6H_6 , and CH_3 (left to right) as a function of disk radius r and disk height scaled by the radius z/r . First row: fiducial model (M0.44F), following the same initial conditions of [Walsh et al. \(2015\)](#). The C/O ratio in this case is 0.44. Second row: model M0.88C; increasing initial carbon abundance by a factor of 2 (C/O = 0.87), this is the extreme case of carbon enrichment. Third row: model M4.4; decreasing the initial oxygen abundance by a factor of 10 (C/O = 4.37). Fourth row: model M8.8C; the combination of oxygen depletion by a factor of 10 and carbon enrichment by a factor of 2, resulting in a C/O ratio of 8.75. Fifth row: model M44; strong oxygen depletion by a factor of 100 resulting in a C/O = 43.72. Sixth row: model M88C; oxygen depletion by a factor of 100 and a carbon enrichment by a factor of 2 resulting in a C/O = 87.47. Light-green arrows in two panels illustrate the variations in vertical and radial extent with varying C/O ratio.

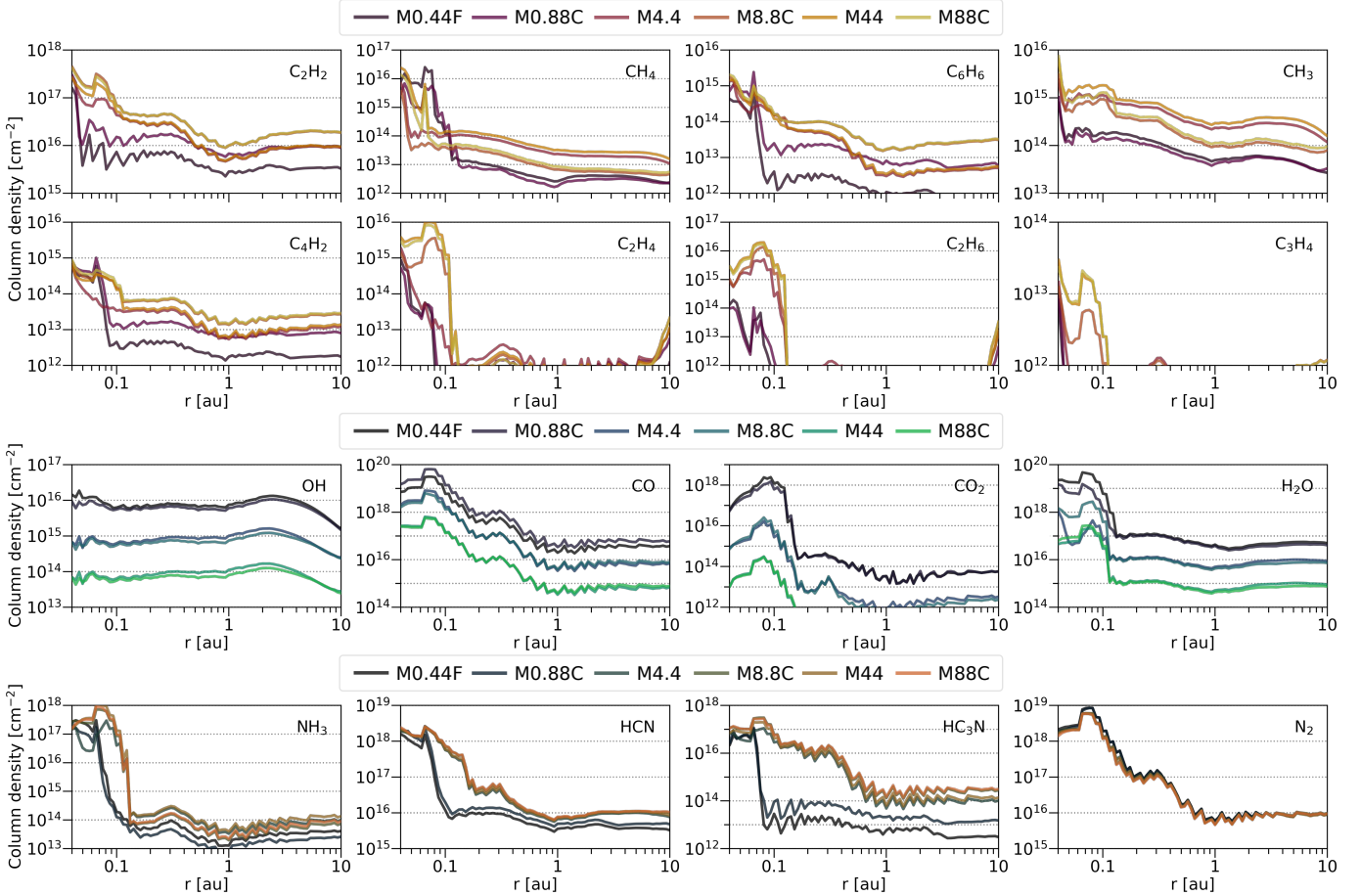


Figure 3. Column density as a function of disk radius, r , for each species integrated vertically from the disk surface to the boundary defining the IR-emitting region (either down to $\tau = 1$ surface at $14 \mu\text{m}$ or to where the gas temperature reaches 200 K). Equivalent figures showing the column density integrated vertically from the disk surface to the $\tau = 1$ surface at $14 \mu\text{m}$ (atmosphere component) and integrated vertically down to the midplane (midplane component) are available online. The line colors from dark to light have increasing values of C/O ratio. (The complete figure set (2 images) is available in the online article.)

lower boundary of the peak abundance of C_2H_2 , CH_3 , C_4H_2 , C_2H_4 , and C_2H_6 is shaped by the gas temperature (200 K) and ionization rate ($\zeta_{\text{XR}+\text{CR}} \approx 10^{-12} \text{ s}^{-1}$). For C_6H_6 and C_3H_4 , only the gas temperature appears to determine the same region (~ 500 K). The abundance of CH_4 is shaped by the gas temperature in the region where this ranges between 500 and 4000 K, the X-ray flux in the region where $z/r < 0.25$ (10^{-3} to $10^{-4} \text{ erg cm}^{-2} \text{ s}^{-1}$), the UV flux ($10^{-5} \text{ erg cm}^{-2} \text{ s}^{-1}$), and ionization rates (for values $< 10^{-12} \text{ s}^{-1}$ within ~ 4 au). For the fiducial model, the fractional abundance map for some species (C_2H_2 , CH_4 , CH_3 , C_2H_4 , C_3H_4 , and C_2H_6) shows a depletion layer below 500 K, which in all cases is then ‘filled in’ as C/O increases. The lower boundary of this layer seems to be determined by the X-ray ($10^{-1} \text{ erg cm}^{-2} \text{ s}^{-1}$) and UV flux ($10^{-5} \text{ erg cm}^{-2} \text{ s}^{-1}$) within ~ 4 au and by the gas temperature (~ 50 K) beyond that radius. For C/O > 1 , the

lower boundary of C_2H_2 , CH_3 , C_4H_2 , C_2H_4 , and C_2H_6 is determined by the gas temperature (a lower temperature than those for C/O < 1 , $\sim 40 - 50$ K), the X-ray and UV fluxes (10^{-1} and $10^{-5} \text{ erg cm}^{-2} \text{ s}^{-1}$, respectively), and the ionization rate ($\sim 10^{-16}$ to 10^{-14} s^{-1}), with species going into ices. For C_6H_6 and CH_4 , the gas temperature contours do not match with either of the fractional abundance maps within 3 au, which suggests that only the X-ray flux, UV flux, and the ionization rates shape its abundance in that region, with the same values as those for C_2H_2 , CH_3 , C_4H_2 , C_2H_4 , and C_2H_6 . The fractional abundances of other species such as C_3H_4 better fit with the contours of gas temperature (~ 3000 K) and ionization rates ($\sim 10^{-16} \text{ s}^{-1}$) for the upper and lower boundary, respectively, and within ~ 4 au. The reason behind this is that each molecule has different routes of formation and destruction that can be enhanced not only by the individual different physical

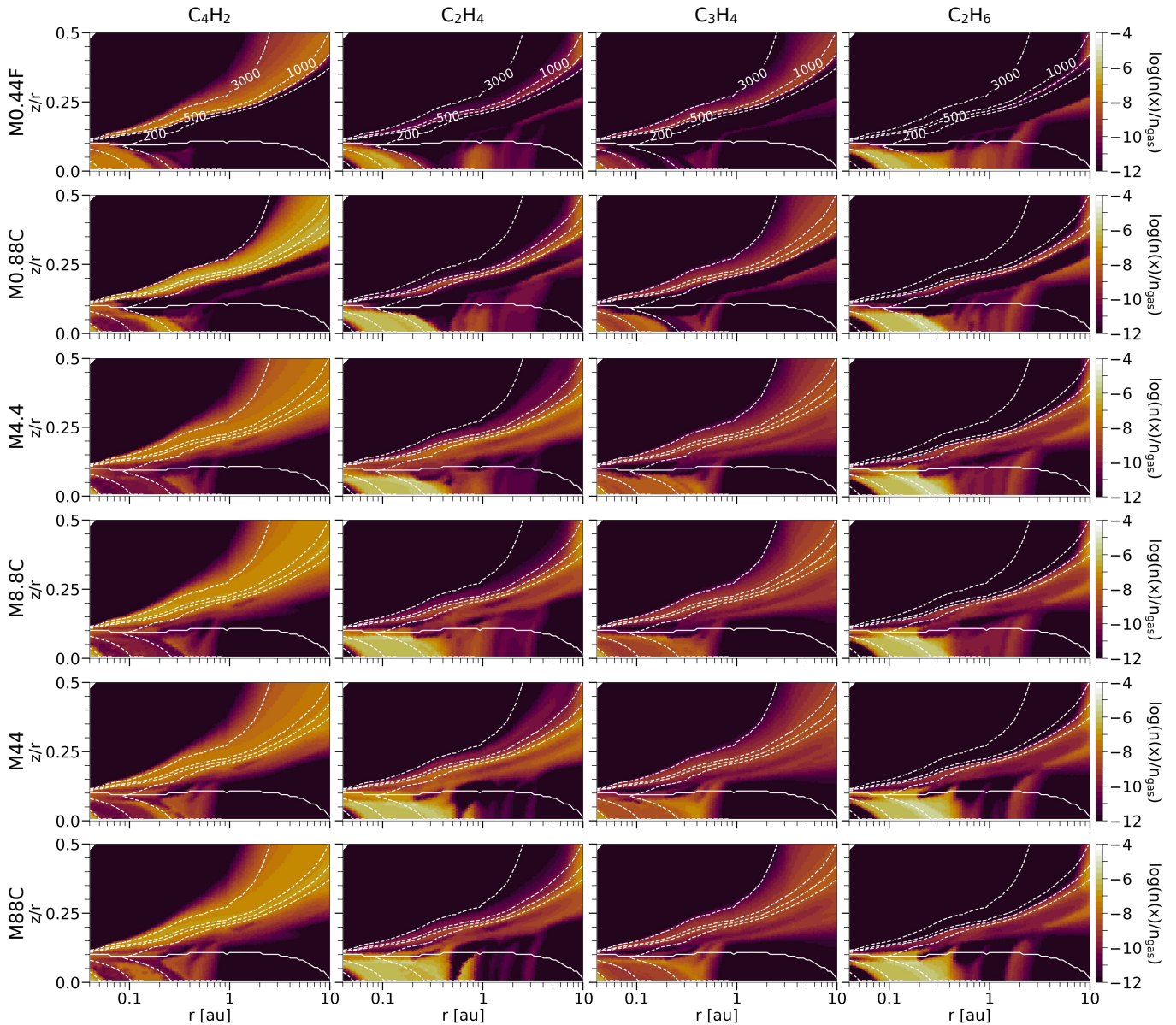


Figure 4. Same as Fig. 2, but for C_4H_2 , C_2H_4 , C_3H_4 (propyne), and C_2H_6 .

conditions but also by the combination of them. Additionally, the reservoir in the inner-disk midplane seems to be determined by the high temperatures and densities in that region of the disk, where neutral-neutral and ion-molecule gas-phase chemistry dominates.

C_xH_y —All of the hydrocarbons, C_xH_y , follow the general abundance pattern discussed above (see Figs. 2 and 4). C_2H_2 reaches a higher peak abundance in the disk atmosphere than the disk midplane (i.e., $\sim 10^{-5}$ in the fiducial model). On the other hand, C_2H_4 and C_2H_6 reach a higher peak abundance in the midplane than in the atmosphere. In the fiducial model, the peak abundance in the midplane takes values of $\sim 10^{-7}$ and $\sim 10^{-6}$ for C_2H_4 and C_2H_6 , respectively. C_6H_6 , C_4H_2 ,

and C_3H_4 reach a similar peak abundance ($\sim 10^{-8}$) in both components.

A general trend with increasing C/O is that for the cases with enhanced carbon (M0.88C, M8.8C, and M88C) the vertical width of the atmospheric component increases with respect to the equivalent reference model and models with oxygen depletion only (M4.4 and M44), with the peak abundance region expanding to denser and colder regions (see Figs. B.1 and B.3). Exceptions to this are the results for C_3H_4 and C_2H_6 , for which the fractional abundance maps show that the vertical width remains constant. This is because the formation pathways of these species are associated not to C_2H_2 but instead with CH_x ions, built up from C^+ and C. This

suggests that once $C/O > 1$, no matter the mechanism behind the increase in C/O , carbon will be more easily incorporated into large hydrocarbons, instead of CH_x ions. Another exception is C_2H_4 , for which the vertical width shrinks with respect to the models with oxygen depletion only, in particular, the upper boundary moves to colder layers (from ~ 3000 to ~ 1000 K). Note that we consider a vertical or radial width expansion (or shrinkage) to be significant when the abundance changes by at least one order of magnitude. Another general trend is that for several species the radial extent of the midplane component increases with increasing C/O (see Appendix D). This is the case for C_2H_2 , C_4H_2 , C_2H_4 , and C_3H_4 . We also see an increase in the vertical extent of the midplane component with the increase of C/O , which is most significant for C_2H_2 , C_2H_4 , and C_2H_6 . A further general observation is that the biggest impact on the distribution and peak abundance reached for all species comes in the first two perturbations, i.e., in the enhancement of carbon (M0.88C) and/or the depletion of oxygen by a factor of 10 (M8.8C/M4.4). Further oxygen depletion, i.e., by a factor of 100, does not result in any further significant increases in peak abundance of the hydrocarbons. This suggests that the chemistry becomes limited by the availability of carbon, i.e., C/H , rather than depletion of oxygen.

The described changes in abundance pattern are reflected in column densities presented in Fig. 3. We provide a more detailed and quantitative description of the response to C/O of each individual hydrocarbon considered in Appendix C. In the remainder of the results we provide this quantitative information for CH_4 and CH_3 , which have a different behavior, and for the O-bearing and N-bearing species, which also have more individual behaviors with increasing C/O .

CH_4 — CH_4 has a broader distribution over the disk than that for the hydrocarbons discussed thus far. It is more abundant in the midplane than in the disk atmosphere, reaching a peak fractional abundance of 10^{-4} across all models within the midplane ($z/r \lesssim 0.1$), and out to ~ 0.06 or 0.1 au, depending on the model. There is a 10 times increase in the abundance of CH_4 where the gas temperature is $\sim 100 - 500$ K and the abundance of CH_4 is lower than $\sim 10^{-10}$ in the fiducial model (M0.44F) when the C/O ratio increases to 0.87 (due to carbon enrichment). However, oxygen depletion has a bigger effect on the abundance of CH_4 in the upper layers of the disk atmosphere ($T_{\text{gas}} \sim 1000 - 3000$ K), with models M4.4 and M44 showing a higher abundance than those that include carbon enhancement. Hence, the abundance of CH_4 is more sensitive to the oxygen abundance in the atmosphere, with a reduced rate of

CH_4 destruction when oxygen is depleted (see also Raul et al. 2025, where similar results are reported). For C/O ratios greater than 1, the drop in abundance in the layer in the outer disk at $z/r \sim 0.1 - 0.2$, and beyond a radius of $\sim 0.8 - 0.9$ au becomes more prominent. This could be related to this region being a sweet spot for grain-surface chemistry ($\sim 20 - 70$ K). The behavior of the radial extent of the midplane component is somewhat sensitive to C/O . The largest radial extent is found for the fiducial model M0.44F (~ 1 au), with peak abundance values between 10^{-5} and 10^{-4} . An increase in C/O via carbon enhancement (M0.88C) shrinks this region to $\lesssim 0.4$ au (toward higher temperatures), which stays similar for all subsequent increases in C/O . This is likely to be due to other reactions in which atomic carbon is a reactant that are more efficient than those forming CH_4 , such as those forming hydrocarbon ices. Also note that in our model the snowlines for hydrocarbons all lie internal to that for CH_4 (see Table 2), which means that if CH_4 formation reactions are not as efficient, carbon can be readily incorporated into hydrocarbon ices.

In general, the column density of CH_4 in the IR-emitting region monotonically decreases with radius from $\sim 10^{16} \text{ cm}^{-2}$ at 0.04 au to $\sim 10^{13} \text{ cm}^{-2}$ at 10 au in all models. The column density of CH_4 in the fiducial model peaks at $\sim 10^{16} \text{ cm}^{-2}$ within ~ 0.1 au and then drops to $\sim 10^{12} - 10^{13} \text{ cm}^{-2}$. An increase in C/O does not necessarily lead to an overall increase in column density of CH_4 in the IR-emitting region. In fact, the opposite is true within 0.1 au: when the C/O ratio increases, the column density of CH_4 drops up to two orders of magnitude within 0.1 au, depending on the model. However, beyond that radius, the column density of CH_4 in oxygen-rich cases ($C/O < 1$) is generally at least a factor of three lower than that in the carbon-rich ($C/O > 1$) models. The drop in the column density within 0.2 au is a result of the depleted region between 0.1 and 0.2 au expanding radially when C/O increases. When C/O increases, the main destruction pathway of CH_4 changes from X-ray-induced photodissociation to the ion-molecule reaction with $C_8H_2^+$. As long chains of hydrocarbons are more abundant in the carbon-rich scenario, CH_4 is destroyed more efficiently. As a result, carbon goes into nitriles, hydrocarbons, and LCCs. Note that this is a feature of our adopted chemical network, where we observe a carbon sink effect in the largest unsaturated hydrocarbons in the network, such as $C_8H_2^+$.

CH_3 —As a radical, CH_3 has an appreciable abundance only in the disk atmosphere (see Fig. 2). The abundance in the fiducial model reaches high values of $\sim 10^{-6}$ in this layer, where the temperature ranges from 1000 to

3000 K. Fig. 2 shows that when increasing the C/O ratio the region over which CH_3 reaches its peak value expands vertically to colder and denser regions, and the peak abundance also increases (up to $\sim 10^{-5}$ in models M44 and M88C).

This enhancement is also visible in Fig. 3, where the column density increases by at least a factor of two at all radii when the C/O increases from oxygen-rich to carbon-rich values. However, again, the biggest effect (i.e., relative increase) comes from combining the first two perturbations (M8.8C, where we have both enhanced carbon and depleted oxygen by a factor of 10). Further increases in C/O do not significantly boost the column density of CH_3 in the IR-emitting region.

3.1.2. Oxygen-bearing Species

The behavior of oxygen-bearing species is somewhat different from that for the hydrocarbons, with a greater dependence on oxygen depletion, rather than carbon enhancement. There is an almost linear response in both peak abundance and column density to the oxygen depletion factor for most oxygen-bearing species.

OH—The fractional abundance of OH is high in the upper layers, where the temperature ranges from ~ 300 to ~ 3000 K, reaching a peak fractional abundance of $\sim 10^{-4}$ in the fiducial model (M0.44F). However, Fig. 5 shows that when C/O increases the peak fractional abundance decreases (reaching a peak $\sim 10^{-6}$ when C/O ~ 88). Similar to that found for the radical CH_3 , OH is also only abundant in the disk atmosphere above the dust photosphere at $14 \mu\text{m}$.

The column density profiles (Fig. 3) of OH across the disk have a close-to-linear response to the oxygen depletion factor. The peak value is $\sim 10^{16} \text{ cm}^{-2}$ in the fiducial model and drops by a factor of ~ 10 in the M4.4 model and by a factor of ~ 100 in the M44 model. Carbon enhancement (models M0.88C, M8.8C, and M88C), on the other hand, affects the OH column density very little, with almost indistinguishable results for models M4.4 and M8.8C and models M44 and M88C.

CO—The abundance of CO in the fiducial model (M0.44F) reaches a peak of $\sim 10^{-4}$ from the midplane to the layers where the temperature reaches 3000 K, with two layers of CO depletion (drop of the abundance by a factor of 10 to 100, depending on the model) at gas temperatures of ~ 1000 and $\lesssim 40$ K. As a hypervolatile, CO has one of the more expansive distributions across the disk, as it only freezes out at temperature $\lesssim 20$ K. The CO-depleted region in the layer between $z/r \sim 0.15$ and 0.25 beyond ~ 2 au is likely related to grain-surface chemistry transforming CO into other molecules, mostly

into CO_2 ice. On the other hand, the slightly depleted layer at ~ 1000 K is more related to photodissociation reactions. When the C/O ratio increases, the size of the region over which CO reaches its peak abundance in the disk atmosphere shrinks vertically, with the CO layer moving to lower gas temperature regions (below 200 K). The lower CO abundance in the atmosphere for these cases weakens the self-shielding of CO to photodissociation and causes the layer to shift downward. The CO-depleted region closer to the midplane also extends inward down to ~ 0.6 au. This is due to CO gas being efficiently converted to ices composed of CO, CO_2 , and LCCs. For models M44 and M88C, the peak abundance decreases by a factor of ~ 10 to $\sim 10^{-5}$.

This is reflected in the column density profiles in Fig. 3. The column density in the IR-emitting region within 0.1 au drops from $\sim 10^{19} \text{ cm}^{-2}$ (M0.44F) to $\sim 10^{17} \text{ cm}^{-2}$ (M88C). Similar to OH, carbon enhancement does not significantly increase the column density of CO relative to the M0.44F, M4.4, and M44 models.

CO₂—CO₂ is an interesting diagnostic, as it has been detected in the three sources discussed here and appears to be a prevalent O-bearing species that can survive and be emissive in an otherwise apparently carbon-rich environment. The fractional abundance of CO_2 in the model M0.44F reaches a peak value of $\sim 10^{-4}$ in the region near the midplane ($z/r < 0.2$) between 0.3 and 0.5 au (see Fig. 5). The peak decreases by a factor of 10 and expands inward radially to 0.05 au when C/O increases to 0.87. The region over which CO_2 reaches its peak abundance in the disk atmosphere is also generally at a lower temperature than that for other O-bearing species such as OH and H_2O . Above $z/r \sim 0.1$ and beyond $r \approx 0.5$ au, CO_2 generally resides in the region between 50 and 200 K with a peak abundance of $\sim 10^{-5}$ in the fiducial model (M0.44F). This lower temperature bound is likely tracing the location of the snow surface for CO_2 . The upper boundary of 200 K is shaped by the high abundance of ions that destroy CO_2 , such as H^+ and H_3^+ , and OH being driven into H_2O rather than CO_2 . Additionally, the ionization rate ($\sim 10^{-14} \text{ s}^{-1}$), X-ray flux ($\sim 10^{-1} \text{ erg cm}^{-2} \text{ s}^{-1}$), and UV flux ($\sim 10^{-5} \text{ erg cm}^{-2} \text{ s}^{-1}$) also shape that region (see Fig. 1 and 5).

When the C/O ratio increases to > 1 (models M4.4 and M8.8C), the abundance decreases by around a factor of 10 in the disk midplane. In particular, the peak abundance within 0.5 au decreases to $\sim 10^{-6}$. There is a similar drop in the atmosphere by almost an order of magnitude with respect to M0.44F and M0.88C. For the two higher values of the C/O ratio (models M44 and M88C), the peak fractional abundance drops to $\sim 10^{-7}$

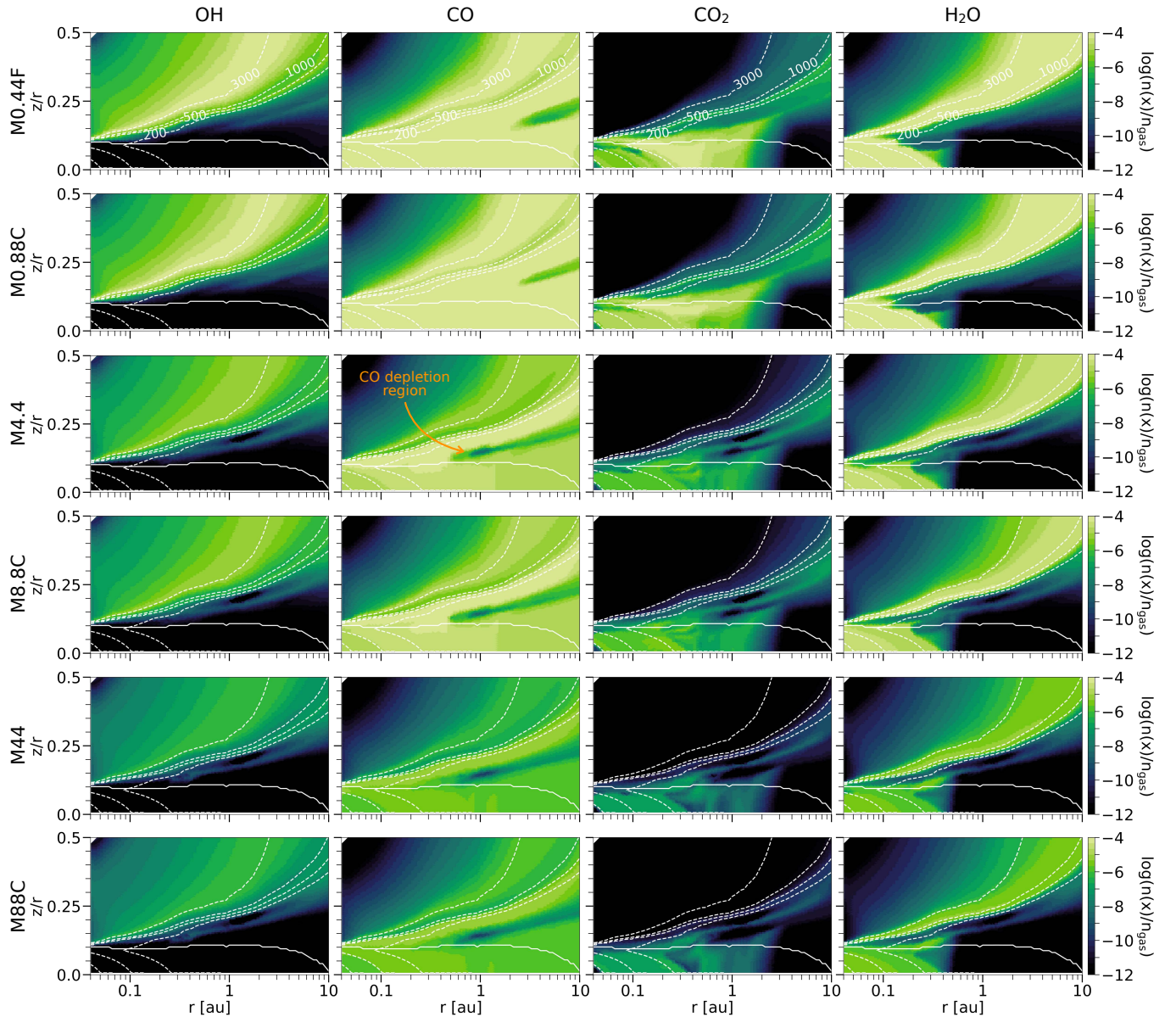


Figure 5. Same as Fig. 2, but for the oxygen-bearing species: OH, CO, CO₂, and H₂O.

in the midplane and $\sim 10^{-9}$ in the atmosphere, again demonstrating an almost linear response to the oxygen depletion factor.

This is also somewhat reflected in the column density profiles in Fig. 3, where the peak column density in the IR-emitting region reduces from $\sim 10^{18}$ cm⁻² within 0.1–0.2 au in the fiducial and oxygen-rich models (M0.44F and M0.88C) to values lower than 10^{12} cm⁻² at 0.2–0.3 au in models M44 and M88C. The column density profiles beyond 1 au are also affected by the CO₂ depletion in the middle layers of the disk (similar to that for CO), with the drop beyond this radius increasing in magnitude with increasing C/O. Again, oxygen depletion has the biggest effect on the CO₂ column densities

rather than carbon enhancement. This is the result of the linear response of CO₂ to the C/O ratio; when C/O increases, less oxygen is available to form CO₂ in the first place.

H₂O—The abundance of H₂O is high in the region where the temperature ranges from 100 to 3000 K, reaching a peak fractional abundance of $\sim 10^{-4}$ in the fiducial model (M0.44F), and its distribution has both the midplane component and the atmospheric component. The response of the abundance of H₂O to the C/O ratio is similar to that of the other oxygen-bearing species, e.g., CO₂: the peak abundance drops to $\sim 10^{-6}$ in model M88C (see Fig. 5) and is much more sensitive to oxygen depletion than carbon enhancement.

This is also reflected in the calculated column density shown in Fig. 3, where the profiles show a step-like structure. The column density of H₂O in the IR-emitting region when C/O = 0.44 reaches a peak value of $\sim 10^{19}$ cm⁻² within 0.1 au. When the C/O ratio increases, this drops by up to two orders of magnitude, to $\sim 10^{17}$ cm⁻² in the same region of the disk. Finally, as found for the other oxygen-bearing species, oxygen depletion has the biggest effect. Carbon enrichment has an effect only in the innermost region within 0.1 au (a variation by a factor up to 100 depending on the model). Beyond that radius, there is no effect of carbon enrichment on the column density profile of water, with the peak value of the column density showing a linear response to the oxygen depletion factor.

3.1.3. Nitrogen-bearing Species

HCN—The abundance distribution of HCN exhibits the same two-component morphology as most other species: a midplane component and an atmospheric component, with the peak fractional abundance in the atmosphere up to 10 times higher than in the midplane. In the fiducial model, the fractional abundance of HCN is high in the region where the temperature is around 1000 K, reaching a peak abundance of $\sim 10^{-4}$. A peak abundance of $\sim 10^{-5}$ is reached in the midplane within ≈ 0.3 au. The size of the disk atmosphere component that reaches values higher than 10^{-8} expands vertically when the C/O ratio increases, with the upper and lower boundaries moving to higher ($\gtrsim 3000$ K) and lower (~ 50 K) gas temperatures, respectively. The models with carbon enhancement have an increased vertical extent when compared with the models with oxygen depletion only (e.g., M88C vs. M44); hence, excess carbon is important for boosting the abundance of HCN in the disk atmosphere. However, the peak fractional abundance reached in the IR-emitting region does not vary with C/O (similar to, e.g., C₂H₂). The peak abundance region in the midplane component also expands radially and vertically, with increasing C/O “filling in” the region between the midplane and $z/r \approx 0.1$ within ≈ 0.3 au. This radial expansion is also observable beyond the mentioned radius for each model, but with a lower abundance.

The column density profiles show a similar shape to those for H₂O (i.e., a steplike behavior). The peak column density is the same in all models, with values of $\sim 10^{18}$ cm⁻² at 0.04 au in the IR-emitting region. The column density drops to $\sim 10^{16}$ cm⁻² beyond ≈ 0.1 au in the oxygen-rich models (M0.44F and M0.88C). The carbon-rich models reach a higher column density beyond ~ 0.1 au, which ranges from more than one or-

der of magnitude higher within 0.2 au to a factor of a few higher beyond. The effects of the “filling in” of the HCN reservoir toward the midplane are evident in the smoothing of the column density profiles within ≈ 1 au as C/O increases. The reason behind this effect is that when C/O increases, nitrogen that was in form of N, N₂, NH₃, and NO is now incorporated into nitriles (e.g., NCCN, HC₃N, HC₅N, HC₉N, and HCN).

NH₃—The distribution of NH₃ shows the same two-component morphology as HCN; however, NH₃ is significantly more abundant in the disk midplane than in the disk atmosphere in the fiducial model (M0.44F). The abundance of NH₃ reaches a peak value of $\sim 10^{-5}$ in the midplane within 0.3 au and a value of $\sim 10^{-7}$ in the disk atmosphere, where the temperature is ~ 1000 K. NH₃ is more sensitive to oxygen depletion than to carbon enhancement. When oxygen is decreased by a factor of 10 (M4.4 and M8.8C), the peak abundance in the atmosphere increases by around the same factor, and the midplane component increases in vertical extent (similar to HCN). Further oxygen depletion (M44 and M88C) does not significantly boost the abundance in the atmospheric component, but the midplane region expands radially outward to 1 au to colder and less dense regions.

This behavior is also reflected in the column density profiles (Fig. 3). The column density at 0.04 au in the IR-emitting region is $\sim 10^{17}$ cm⁻² in all models. When the C/O ratio increases to carbon-rich values (M4.4, M8.8C, M44, and M88C) there is a boost in the column density of NH₃ within ~ 0.1 au by almost one order of magnitude. Beyond that radius, models with a C/O > 1 have a higher column density by a factor of a few, with all models ranging between $\sim 10^{13}$ and $\sim 10^{14}$ cm⁻².

HC₃N—The behavior of HC₃N is very similar to that for NH₃. The fractional abundance of HC₃N reaches a peak value of $\sim 10^{-6}$ in the innermost regions of the disk and a value of $\sim 10^{-8}$ in layers where the temperature ranges from 500 to 1000 K in the fiducial model. The response of the abundance of HC₃N to the C/O variations is somewhat similar to that for HCN, in that the region size where the abundance peaks expands radially (in the disk midplane to lower temperatures and less dense regions) and vertically (in both components, filling up the region between these two components) when C/O increases (see Fig 6). For the first perturbation, there is an increase in the peak abundance reached in the disk midplane by a factor of a few between ~ 0.1 and ~ 0.2 au. For higher values of C/O ratio, there is no increase in the peak abundance; however, the peak in the atmospheric component does increase to $\sim 10^{-6}$ in models with C/O ≥ 4.4 . The distribution of HC₃N

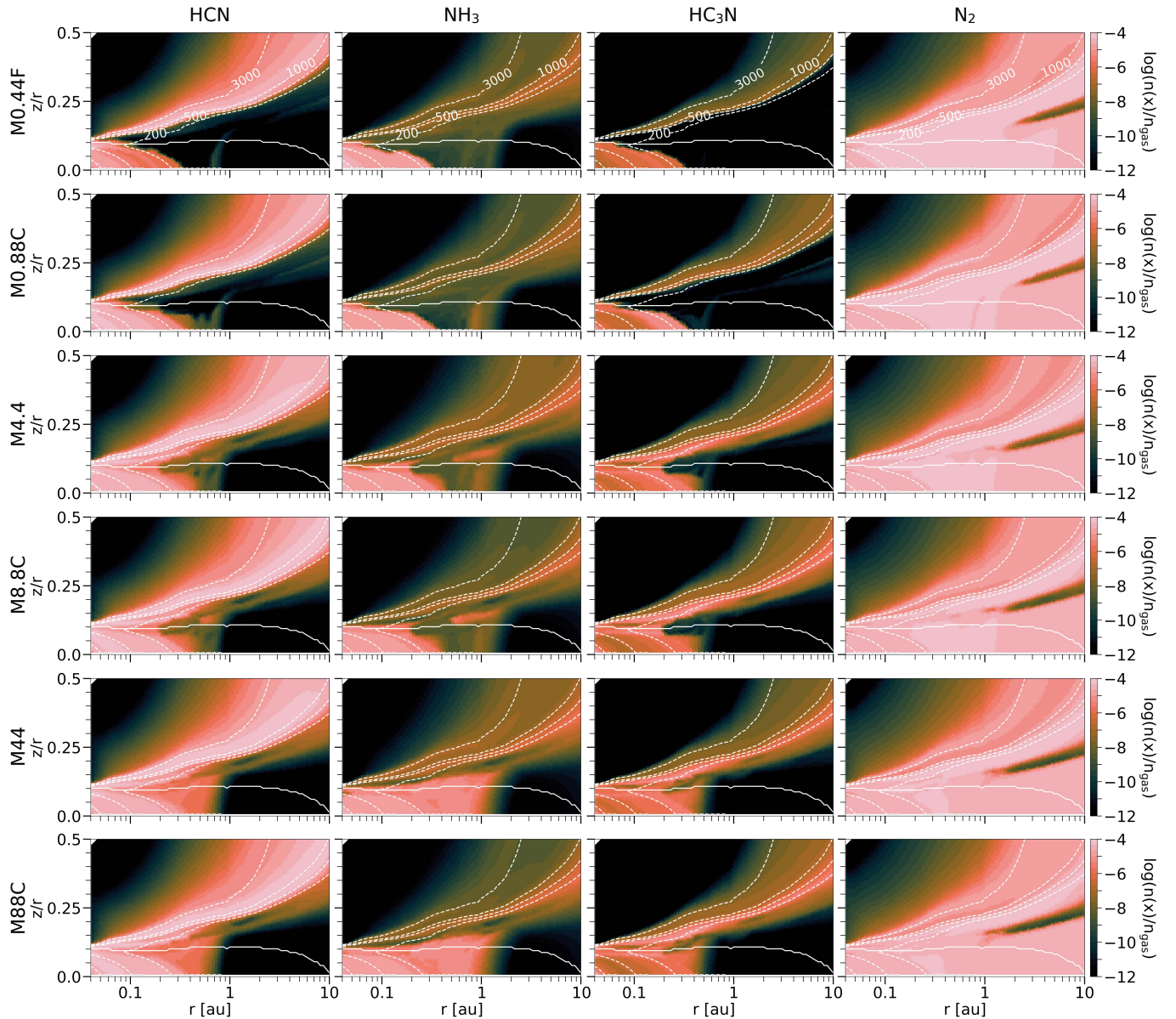


Figure 6. Same as Fig. 2, but for the nitrogen-bearing species: HCN, NH_3 , HC_3N , and N_2 .

is also sensitive to the enhancement of carbon, with the carbon-enriched models having a slightly greater vertical extent of atmospheric HC_3N (moving to higher gas temperatures and less dense regions) than the equivalent models with oxygen depletion only; however, this effect is very subtle.

This behavior with C/O is also seen in the column density profiles in Fig. 3. The peak column density in the fiducial model is $\sim 10^{17} \text{ cm}^{-2}$ within 0.07 au and reduces to $\sim 10^{13} \text{ cm}^{-2}$ beyond. The peak column density in the inner disk does not change with C/O; only the region over which this is reached increases in radial extent. Again, the behavior of carbon-rich models differs from the oxygen-rich cases. Beyond 0.1 au, the

column density for M0.44F and M0.88C is lower than $\sim 10^{14} \text{ cm}^{-2}$. The column density in the carbon-rich models, on the contrary, decreases monotonically out to 1 au and thereafter remains flat at $\sim 10^{14} \text{ cm}^{-2}$.

N_2 —The fractional abundance of N_2 reaches peak values ($\sim 10^{-4}$) in the region from the midplane to the layers where the temperature reaches 500 K (see Fig. 6). Similar to CO, N_2 shows a depleted region that expands inward (to denser and colder regions) when the C/O ratio increases. This is the only major effect of increasing C/O. This is because the chemistry is driving nitrogen into N-bearing ices, such as NH_3 , HCN , CH_3NH_2 , and HC_3N . The column density for the IR-emitting region has similar profiles for all C/O values. In general, the

column density profile decreases with radius, reaching a constant value beyond ~ 0.8 au ($\sim 10^{16}$ cm $^{-2}$).

3.2. Potentially Observable Species

Other molecules have been previously predicted to be abundant enough to be detected in the inner disk (Bast et al. 2013). This is the case of the nitriles CH₃CN and HNC, which are also commonly detected at millimeter wavelengths. Kanwar et al. (2024b) also suggest that the abundance of C₂, C₂H, C₃, C₃H, and CH₂CCH may reach observable abundances in the IR-emitting region at elevated C/O.

We present the fractional abundance maps and column density profiles predicted by our models for the different C/O scenarios for these potentially observable species in Figs. E.1, E.2, and E.3 in Appendix E. As shown in these figures and in Fig. F.3, the abundance and number of molecules of C₂, C₂H, C₃, C₃H, CH₂CCH, CH₃CN, and HNC increase when C/O increases with respect to the fiducial model (M0.44F). However, similar to the case of C₂H₂ and most of the hydrocarbons mentioned so far in this work, the abundance does not increase linearly with the C/H and O/H variations.

4. DISCUSSION

Here we more closely compare the model results with the observations in order to determine whether any conclusions can be drawn on the C/O ratio needed to explain the observations of the sources considered here. Because we have adopted a generic model, rather than one tailored to a particular source, we also compare the total number of emitting molecules, as well as their ratios. This is because this removes, to some extent, the dependence on physical properties such as the disk gas mass and radial distribution, as well as degeneracies that are often met when trying to fit both column densities and emitting areas for optically thin emission (see discussion in Kamp et al. 2023 and Arulanantham et al. 2025).

4.1. Observational Trends

In Table 4 we show the total number of molecules reported by Tabone et al. (2023), Arabhavi et al. (2024), Kanwar et al. (2024b), and Arabhavi et al. (2025b) for the species detected toward the hydrocarbon-rich disks of J160532, ISO-ChaI 147, and Sz28, respectively. We do not include estimates by Kaeufer et al. (2024) for Sz28, which are up to eight orders of magnitude higher than those reported by Kanwar et al. (2024b). To better visualize the range of molecular parameters derived from the observations, we present the data reported by

the papers above in Figure 7. Presented are excitation temperatures T_{ex} versus the total number of molecules \mathcal{N} for each source and each detected species. This highlights two by-eye interesting trends. First, the excitation temperatures toward ISO-ChaI 147 are lower than those for J160532, with Sz28 somewhat intermediate between the two. A second trend is that ISO-ChaI 147 generally has the largest number of molecules, with the values for Sz28 and J160532 generally lower.

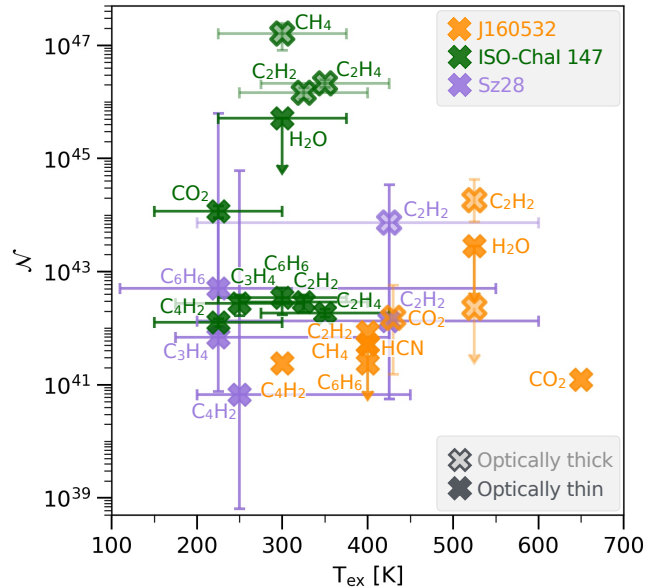


Figure 7. Summary of the results available in the literature for J160532 (Tabone et al. 2023; Arabhavi et al. 2025b), ISO-ChaI 147 (Arabhavi et al. 2024), and Sz28 (Kanwar et al. 2024b), using a 0D slab model to estimate the total number of emitting molecules, \mathcal{N} , and excitation temperature, T_{ex} . The different colors represent the different disks. The filled and open crosses represent the optically thin and thick components, respectively, for each species when available (C₂H₂ and CO₂ for J160532; C₂H₂, CH₄, and C₂H₄ for ISO-ChaI 147, and C₂H₂ for Sz28.) Note that some error bars for different species and/or sources might superpose. For more information see Table 4.

The number of molecules for hydrocarbons in the thin component ranges from $\sim 10^{41}$ to $\sim 10^{43}$. The values for the thick component for the same set of species are, in general, higher ($\sim 10^{44} - 10^{47}$). From Fig. 7, ISO-ChaI 147 is overall more rich in hydrocarbons and oxygen-bearing species than J160532 and Sz28. For example, the number of molecules of CO₂ is three orders of magnitude higher in ISO-ChaI 147 than in J160532. The total numbers of molecules in the optically thin component for hydrocarbons are similar for both ISO-ChaI 147 and J160532, while \mathcal{N} of H₂O is three orders of magnitude higher in ISO-ChaI 147 than in J160532.

Because the numbers of molecules in the optically thin component for the hydrocarbons in both J160532 and ISO-ChaI 147 are similar, this results in the latter being relatively more hydrocarbon-poor relative to CO₂ than the former.

The results also suggest that hydrocarbons and oxygen-bearing species in ISO-ChaI 147 and Sz28 are emitting mostly from regions colder than those in J160532. The excitation temperature for the optically thick component of C₂H₂ is 525 K in J160532 and 300 K in ISO-ChaI 147. In addition, the excitation temperature of CO₂ is ~ 200 and ~ 650 K for ISO-ChaI 147 and J160532, respectively. We also see that C₂H₂ tends to have a temperature higher than or equal to those of other hydrocarbons, such as C₆H₆, CH₄, C₄H₂, and C₃H₄ in the same disk.

We can compare these excitation temperatures with the gas temperature distribution and average temperature for each species predicted by our models (see Appendix H). Our results show that larger hydrocarbons such as C₃H₄, C₄H₂, C₂H₄, and C₆H₆ exhibit average temperatures in the IR-emitting region between 700 and 1200 K in the fiducial model (M0.44F). The lower and upper ends of this range decrease to 400 and 1000 K, respectively, when C/O increases to ~ 88 . Note that the upper end decreases even more (to 800 K) when only oxygen depletion by a factor of 100 is considered. CO₂ remains comparatively cooler ($\lesssim 300$ K) across all C/O values, whereas HCN, H₂O, and smaller hydrocarbons such as CH₄ and C₂H₂ cover a larger temperature range of 1000 – 1450 K. From the values derived from observations and shown in Fig. 7, larger hydrocarbons also cluster around intermediate temperatures, but significant differences between sources are observed for CO₂, HCN, and H₂O. For example, the derived excitation temperature for CO₂ is relatively low in ISO-ChaI 147 (225 K) but higher in J160532 (430 – 650 K).

4.2. Comparison with Observations

In this subsection, we compare the total number of molecules predicted by the model with those derived from the observations (see Table 4). To do this, we calculated the total number of molecules (\mathcal{N}) for each species by integrating our model abundances across the IR-emitting region (a gas temperature > 200 K and above the dust photosphere at 14 μm). For this, we used the following equation:

$$\mathcal{N} = \int_R N(r) 2\pi r dr, \quad (1)$$

where $N(r)$ is the vertically integrated column density as a function of the disk radius r , ranging from 0 to R , where R is the integration radius.

Figure 8 shows the comparison between the model number of molecules for the IR-emitting region and those reported for the species observed toward J160532, ISO-ChaI 147, and Sz28 with orange, green, and purple crosses, respectively (top panel), and the ratios for the same set of species with respect to CO₂ (bottom panel). We used CO₂ as our relative species because we find that it is more sensitive to the C/O ratio than others (e.g., C₂H₂). Both optically thin and thick components are included if available. The shaded squares represent the increasing C/O ratio value from dark to light, i.e., the different models tested in this work. From the ratios in the bottom panel of Fig. 8, it is clear that the ratio with respect to CO₂ is a potentially powerful diagnostic of the global C/O in the infrared-emitting region of the disk. Note that there is a spread of up to four orders of magnitude in the ratios with respect to CO₂ for a spread of only two orders of magnitude in the C/O ratio. For reference we present the column density ratio for C₂H₂/CO₂ as a function of radius in Fig. I.1.

From the top panel of Fig. 8 we see that the model reproduces (around the same order of magnitude) the total number of molecules for CH₄ (thin component), C₆H₆, C₄H₂, CO₂, and H₂O but only for some disks and for different values of C/O, depending on the species. For example, we can reproduce \mathcal{N} of J160532 for CO₂ but only for the moderately enhanced C/O models (M4.4 and M8.8C). This is also achieved for CH₄ for the fiducial model (M0.44F) and cases that included carbon enrichment (M0.88C, M8.8C, and M88C) and for C₆H₆ for the carbon-enriched-only (M0.88C) and oxygen-depleted-only models (M4.4 and M44). The number of molecules in the IR-emitting region for these three species up to 10 au varies differently with increasing C/O; it decreases for CO₂ and oscillates for CH₄ and C₆H₆, with the carbon-rich models having a larger number of molecules than the equivalent oxygen-depleted models (see Figs. F.1 and F.2). All models overestimate the number of molecules in the thin component of C₂H₂, reaching values of the order of magnitude of the thick component in J160532. The fiducial model (M0.44F) is consistent with the upper limit reported for H₂O for ISO-ChaI 147, while the higher C/O ratio models (M44 and M88C) better fit that estimated for J160532. For all other species (C₂H₄, C₃H₄, and HCN), there is a difference of more than one order of magnitude between the models and observations for J160532, ISO-ChaI 147, and Sz28 from Tabone et al. (2023), Arabhavi et al. (2024), and Kanwar et al. (2024a), with the observations generally suggesting higher values than the models (with the exception of HCN). For the thin component of C₂H₂ and C₃H₄ in Sz28, the values obtained in the oxygen-

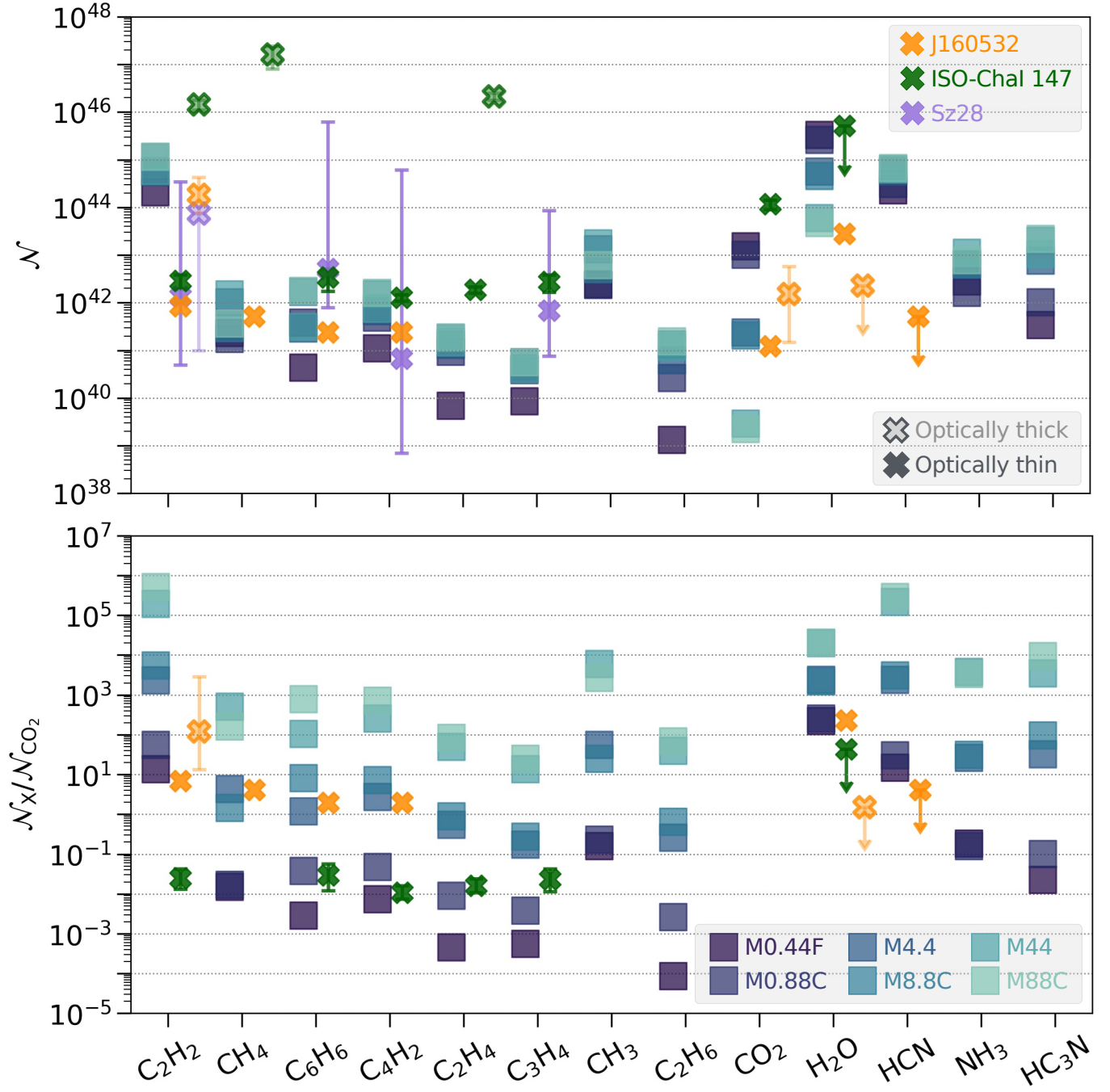


Figure 8. Top: total number of molecules of C_2H_2 , CH_4 , C_6H_6 , C_4H_2 , C_2H_4 , C_3H_4 , CH_3 , C_2H_6 , CO_2 , H_2O , HCN , NH_3 , and HC_3N . The values estimated here are the integrated total number of molecules up to 10 au, integrating over the IR-emitting region. Bottom: total number of molecule ratios of the same set of species with respect to CO_2 . The orange, green, and purple crosses represent the results from Tabone et al. (2023), Arabhavi et al. (2024), Kanwar et al. (2024b), and Arabhavi et al. (2025b) for J160532, ISO-Chal 147, and Sz28, respectively. The filled and open crosses represent the thin and thick components for each species when available, respectively. The shaded colored squares represent from dark to light the increase of the C/O ratio, i.e., the results from our chemical models with different C/O ratios. The bottom panel shows the ratio of the number of molecules with respect to CO_2 . (The complete figure set (2 images) is available in the online article.)

rich and carbon-rich models, respectively, are consistent with the uncertainties reported for these species. On the other hand, the observations for C_4H_2 in the same source do not constrain the C/O ratio, as all models fall within the corresponding error bars.

The bottom panel of Fig. 8 shows that the observed ratios for J160532 are consistent with a wide range of C/O ratios. In particular, solar-like C/O ratios can reproduce the \mathcal{N} ratios reported for C_2H_2 , HCN, and the oxygen-bearing species H_2O . On the other hand, CH_4 , C_6H_6 , and C_4H_2 are consistent with moderately enhanced C/O ratios ($\sim 4.4 - 8.8$). However, all the equivalent values for ISO-ChaI 147 are consistent with solar C/O or moderately enhanced C/O, i.e., similar to 1 or of order a few ($\lesssim 4.4$). We decided not to perform the same analysis for Sz28, because the values reported by Kanwar et al. (2024b) for CO_2 are not a best fit to the available data and are used for illustration of the detection of CO_2 only. Taking the values from Table B.1 in Kanwar et al. (2024b) suggests a very high total number of molecules of CO_2 ($\sim 10^{48}$), which is a factor 10^4 higher than that extracted for ISO-ChaI 147.

Our results suggest that efficient production of hydrocarbon species does not always require a $C/O > 1$. Despite ISO-ChaI 147 appearing significantly more hydrocarbon-rich than J160532 through the number of species detected, the model ratios in Fig. 8 suggest that this source could be globally less carbon-rich than J160532. We emphasize here that this is based on models assuming a single X-ray luminosity of $10^{29} \text{ erg s}^{-1}$, which is around the middle of the observed range for VLMSs. We cannot rule out any degeneracies in the results between X-ray luminosity and C/O, and we will explore this in future work.

In our definition of the IR-emitting region, we assume a lower temperature bound of 200 K. If this gas temperature constraint is relaxed and the integration to determine \mathcal{N} is extended down to the $\tau = 1$ surface at $14 \mu\text{m}$ over the whole disk, most species show only small, model-dependent increases, because they reach their peak abundance well above this temperature threshold. We find that CH_4 and CO_2 are the most strongly impacted, as they are more abundant than the other species considered here in the colder regions that would be now included in the integration. Thus, the ratios with respect to CO_2 that we present in Fig. 8 would be affected by a common factor. For interest, versions of Fig. 8 for the disk atmosphere and midplane components are available online.

Although we obtain reasonable agreement with the optically thin component based on number of molecule ratios, the numbers of molecules estimated from our mod-

els do overestimate C_2H_2 and HCN (see top panel of Fig. 8). This motivated the question of whether it is possible to obtain a better agreement if we use a different radius of integration, given that we do not know the size of these compact disks. To explore the sensitivity of the total number of molecules with the assumed IR-emitting area, we also estimate the total number of molecules integrated out to 0.1, 1, and 10 au, for one model (M8.8C) for which the number of molecules results have reasonable agreement with those for J160532. Additionally, to test the possible degeneracy between disk size and C/O ratio, we include the \mathcal{N} for the same sets of integration radius for the fiducial model (M0.44F). Fig. 9 presents these values and compares with the total number of molecules reported by Tabone et al. (2023) and Arabhavi et al. (2025b) for the species presented (C_2H_2 , CH_4 , C_6H_6 , C_4H_2 , CO_2 , H_2O , and HCN). For a solar-like C/O ratio (M0.44F), \mathcal{N} for the optically thin component of C_2H_2 is better reproduced with a smaller radius of integration (~ 1 au). In the carbon-rich scenario (M8.8C) a radius of integration of ~ 0.1 au better reproduces the number of molecules in the thin component. Other hydrocarbons such as CH_4 , C_6H_6 , and C_4H_2 are already well mimicked, with the full integration of the disk up to 10 au with the observed values lying close to the model values for both C/O ratios (e.g., CH_4) or in between the model predictions (e.g., C_6H_6 and C_4H_2).

The models predict a low dependence of \mathcal{N}_{CO_2} on the radius of integration for both the M0.44F and M8.8C models. The optically thin component of CO_2 is well reproduced for all integration radii for $C/O \sim 8.8$, but overestimated for the oxygen-rich model. The apparent convergence of \mathcal{N} when increasing the integration radius suggests that the optically thick component of CO_2 is not well reproduced for any of the models, being overestimated by M0.44F and underestimated by M8.8C; an intermediate C/O might achieve better agreement. However, both models (M0.44F and M8.8C) and all integration radii are consistent with the reported uncertainties. Figure 8 shows that \mathcal{N}_{CO_2} has a steplike behavior, only varying when O/H decreases, so C/O ratios of ~ 0.88 and ~ 4.4 will follow the M0.44F and M8.8C trends, respectively. H_2O is overestimated by the fiducial model but better reproduced for $C/O \sim 8.8$ with an integration radius of 0.1 – 1 au. Species such as HCN are overproduced by at least one order of magnitude in all cases. From these results, we see an overlap of the estimated \mathcal{N} for the different radii of integration and C/O ratios.

4.3. Carbon, Oxygen, and Nitrogen Reservoirs

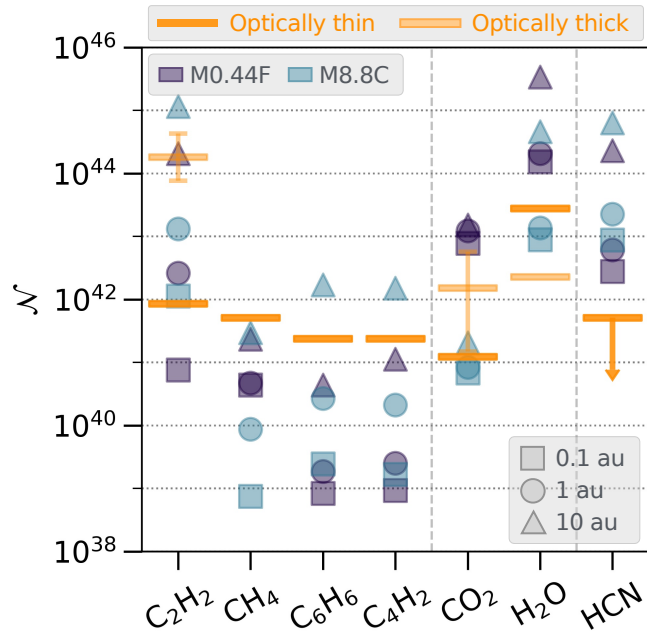


Figure 9. Total number of molecules in the IR-emitting region, estimated using eq. (1), for J160532 (orange horizontal lines; Tabone et al. 2023; Arabhavi et al. 2025b) and the fiducial (M0.44F) and carbon-rich (M8.8C) models (dark purple and light-blue shapes, respectively) for C_2H_2 , CH_4 , C_6H_6 , C_4H_2 , CO_2 , H_2O , and HCN . The values estimated for our model are the result of an integration up to 0.1 (squares), 1 (circles), and 10 au (triangles).

Here we discuss the main carriers for carbon, oxygen, and nitrogen and how they vary when different integration radii and C/O ratios are considered. This is worth exploring to check whether there are additional carriers of C, O, and N that are not probed by the observations. We focus on the effect of an increase of C/O by comparing the fiducial and solar-like model (M0.44F) with the first model that includes both oxygen depletion and carbon enrichment (M8.8C).

Figure 10 presents pie charts showing the percentage contribution of species to the total carbon (left), oxygen (middle), and nitrogen (right) budget for the IR-emitting region. We consider averages over the different integration radii (0.1, 1, and 10 au) and include a comparison with the very innermost radius of our model grid (at 0.04 au). We list individual species with more than a 5% contribution by molecular mass. For species with a smaller contribution, we sum up their contribution in a category called “Other.” We have an additional category called “LCC,” which stands for “long carbon chains” (Fig. J.1 presents the breakdown of this sector, showing in detail the most abundant species in the category). In many cases we find that a significant fraction of carbon is contained within multiple hydrocarbon

species with three or more carbon atoms, and we group these together in a single category.

For a solar-like C/O, in the innermost region of the disk in the IR-emitting region (at 0.04 au), carbon is mostly in CO ($\approx 65\%$), with smaller contributions from LCC and HCN (all $< 15\%$). When we integrate up to 0.1 au, CO remains as the main carrier (86%) and the contribution from LCC drops to ($\approx 1\%$). CO_2 also emerges as a main carbon carrier here ($\approx 10\%$). The results out to 1 au are similar to those out to 0.1 au. When integrating out to 10 au, because only regions where the gas temperature is higher than 200 K have been considered, the atomic carbon becomes a key carrier ($\approx 7\%$), along with C_2H_2 , HCN, and HCN ice, all with a contribution lower than 6%. However, CO remains the main carrier of carbon.

When C/O increases to ~ 8.8 , carbon is mainly contained in LCCs for all methods of calculation (i.e., at 0.04 au, and integrated out to 0.1, 1.0, and 10 au). CO and HCN show up as carbon carriers at 0.04 au and out to 10 au, but their individual contributions are lower than 16%.

In the innermost region of the disk (at 0.04 au) there is a high abundance of LCCs for both C/O < 1 and C/O > 1 . This is also seen in Kanwar et al. (2024b), who they report high column densities of hydrocarbons at small radii ($r < 0.1$ au) regardless of the C/O adopted, showing that carbon enrichment may not be necessary for the efficient synthesis of hydrocarbons in the very innermost region of the disk. Figures J.2 and J.3 show the fractional abundance maps for some of the most abundant LCC species (C_9H_2 , $C_{10}H_2$, CH_2CCH_2 ice, CH_3CCH ice, HC_5N , HC_7N , HC_9N , and HC_3N ice); see Fig. J.1. The fractional abundance maps for other abundant LCC species, such as HC_3N , C_3 , and C_3H , are shown in Figs. 6 and E.1. Note that the high abundance of large unsaturated hydrocarbon species is likely a carbon sink effect of the chemical network, with carbon piling up in the longest C-bearing species in the network. This effect may be exacerbated by the fact that our network does not include destruction routes from LCCs back to C_2H_2 or smaller hydrocarbons. We note here that the largest and most abundant LCCs in our models have not yet been detected, highlighting the need for future observations to test this scenario.

For oxygen, H_2O and CO are the main carriers in the inner disk (≤ 0.1 au). In the IR-emitting region CO is the main carrier for both the oxygen-rich case (M0.44F) and the carbon-rich scenario (M8.8C). Beyond 0.1 au, both models have different species as important oxygen carriers. For the oxygen-rich case, atomic oxygen becomes a key main carrier when integrating up to 1 and

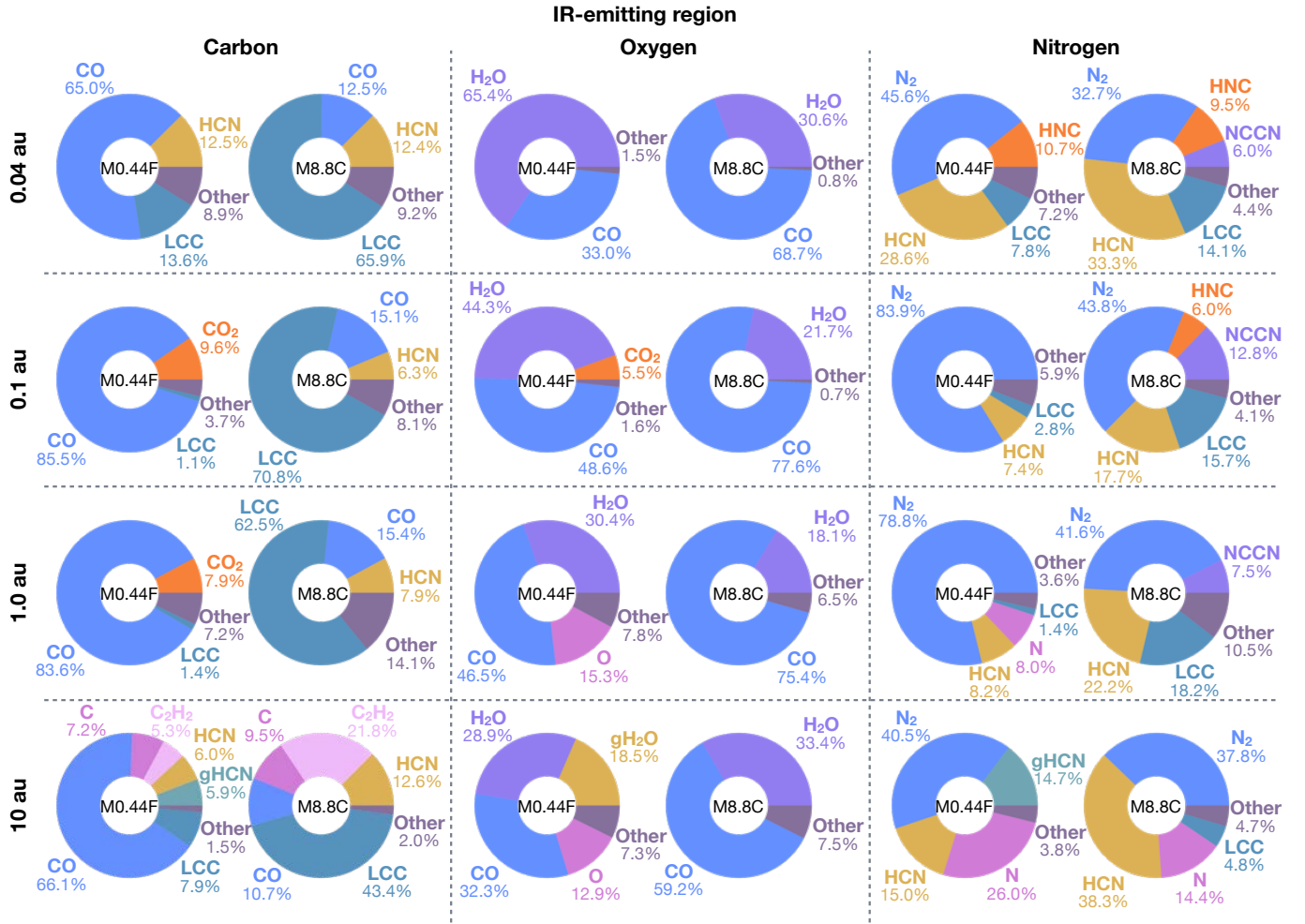


Figure 10. Pie charts showing the contribution of species by molecular mass to the total budgets for carbon (left), oxygen (middle), and nitrogen (right) for two C/O ratios: ~ 0.44 (M0.44F) and ~ 8.8 (M8.8C). We show values at a radius of 0.04 au (innermost region of the disk) and for integration up to radii of 0.1, 1, and 10 au. We present values for the *atmosphere* only considering the IR-emitting region. “LCC” represents the summation of LCCs with ≥ 3 carbon atoms with a contribution $\geq 1\%$ by molecular mass. “Other” represents the summation of all the species with a contribution $< 5\%$. (The complete figure set (2 images) is available in the online article.)

10 au. Additionally, H_2O ice emerges as a main carrier when integrating over all disk extent. None of this happens for the carbon-rich case M8.8C, which has H_2O and CO as key carriers across all methods of integration. When integrating up to 0.1 au, CO_2 emerges as an important carrier ($\sim 6\%$).

For nitrogen, in most cases N_2 is the main carrier across the models. Within 0.1 au, nitrogen is mainly in the form of N_2 , HCN, HNC, and NCCN (in the carbon-rich model only), and HC_5N in the innermost disk (at 0.04 au) for M8.8C. Beyond 0.1 au, HCN and N_2 remain as main carriers, although atomic nitrogen becomes a key contributor to the nitrogen budget for the oxygen-rich case, as well as more complex molecules such as cyanopolynes (e.g., HC_3N and HC_9N) in the carbon-rich model. For the outer-disk regions (> 1 au), nitro-

gen is mostly in its molecular and atomic form, with the appearance of HCN ice in the oxygen-rich model. The main carriers of nitrogen between the fiducial case and carbon-rich case do not differ significantly in nature and usually differ only in percentage contribution. For example, HCN has an increased contribution in the inner disk (≤ 0.1 au) in the carbon-rich case versus the oxygen-rich case ($\approx 33\%$ vs. $\approx 29\%$ at 0.04 au).

Our models predict a set of hydrocarbons and oxygen- and nitrogen-bearing species as key and main carriers for the C, O, and N reservoirs. In particular, CO, H_2O , and N_2 remain as key carriers for all radii of integration for both values of C/O. From these species, only H_2O has been detected in J160532 and ISO-ChaI 147. Other species such as C_2H_2 , CO_2 , and HCN also become key carriers under specific conditions. For example, C_2H_2 is

a key carbon carrier when the full disk extent is considered (up to 10 au) for both M0.44F and M8.8C models; however, when C/O increases from 0.44 to 0.88, its contribution to the carbon budget increases from $\approx 5\%$ to $\approx 22\%$, which suggests that an enhanced C/O ratio is needed to explain the high abundances of C_2H_2 in the three disks. However, CO_2 , an oxygen-bearing species detected in J160532, ISO-ChaI 147, and Sz28, is only a key carrier for a solar-like C/O and smaller radius of integration ($\sim 0.1 - 1$ au). Finally, our results suggest that other carbon carriers such as NCCN and LCCs (see Fig. J.1) would be good targets to look for in the IR spectra, as they are key carriers of carbon and not probed by current observations. Additionally, these species are likely to be good tracers of an enhanced C/O ratio. For example, C_9H_2 appears as a key contributor to LCCs when C/O ~ 0.44 , and increases to $\approx 52\% - 69\%$ when C/O increases to ~ 8.8 (when integrating up to 1 au). We also note with caution here that the chemistry in our network does not go to saturation for species with three or more carbons; thus, the unsaturated LCC species act as carbon sinks in the network.

4.4. Effects of C/O on Nitrogen-bearing Species

In the different scenarios that we have explored, we only vary the C/O ratio. However, from the fractional abundance maps (Fig. 6), column density profiles (Fig. 3) and number of molecules versus C/O ratio profiles of HCN, NH_3 , and HC_3N in Fig. F.2, we can see that nitrogen-bearing species do respond to C/O variations even though N/H is constant across the different models.

Overall, the total number of molecules of NH_3 increases when O/H decreases, and it slightly decreases when C/H increases. For all C/O ratios, the number of NH_3 molecules varies by less than one order of magnitude. For the case of N_2 , carbon enrichment and/or an oxygen depletion result in a constant \mathcal{N} with respect to the fiducial model (M0.44F).

Wei et al. (2019) suggest that the HCN abundance is a good tracer of the effect of carbon grain destruction within the soot line. From the fractional abundance maps in Fig. 6 we see that the HCN midplane abundance increases when C/H increases, which is consistent with the results from Wei et al. (2019). This increase in HCN with carbon enhancement is also evident in Figs. 3 and F.2; however, as found for many species, the biggest relative change in HCN total number of molecules comes in the first two perturbations, i.e., for a C/O of 0.47 and 0.87.

NH_3 is a potentially observable molecule, perhaps detected toward Sz28 in the reanalysis of the data by Kaeufer et al. (2024). Additionally, to compare with other published literature, albeit for T Tauri stars, Pontoppidan et al. (2019) present a comparison between the NH_3/H_2O and HCN/H_2O ratios in the inner disk of the protoplanetary disks around three solar-mass stars. They show that the HCN abundance is expected to be between one and two orders of magnitude larger than the NH_3 abundance. Potential future diagnostics of C/O in the inner regions of disks should include NH_3 . Further, the models suggest that the ratio of NH_3 to nitriles may depend on the X-ray ionization rate in the disk, with more carbon driven into nitriles for a higher X-ray ionization rate. We intend to explore these potential diagnostics in future work.

4.5. Chemical Pathways

In general, we find the same active chemical pathways as discussed in Walsh et al. (2015) and Kanwar et al. (2024a). Note that we use the full RATE12 version of the UMIST database for astrochemistry, whereas Kanwar et al. (2024a) adopt a subset of those reactions in their version of the network. We see that the main chemistry routes between an oxygen-rich and carbon-rich scenario are not so different. We noted that some formation and destruction routes are different, for example, oxygen-related reactions are not as efficient in the carbon-rich model as in the oxygen-rich one, due to the high oxygen depletion by a factor of 100. However, other pathways are preferred to form and destroy the same species. Kanwar et al. (2024a) reached a similar conclusion albeit for a C/O ratio of 2 when comparing with a model assuming C/O = 0.45. To better illustrate this, see Figs. 4 and 5 from Walsh et al. (2015) and Figs. 3 and 6 in Kanwar et al. (2024a). The main variation we see is in the percentage of the dominance of the different reactions, but there are few new chemical pathways for formation or destruction at higher C/O ratios.

As an example, Fig. K.1 illustrates the main formation pathways for C_6H_6 and C_4H_2 for both the M0.44F and M8.8C models. In this, we see a bottom-up scheme, where long hydrocarbons, such as C_6H_6 are formed starting with the reaction between atomic carbon and H_3^+ . Note that we only list reactions that have a contribution of at least 10% to the rate of formation of the different species. As mentioned before, the main chemistry routes do not change significantly as the C/O increases. In the oxygen-rich scenario (M0.44F), chemistry involving CO is important for the formation of C^+ , whereas in the carbon-rich case (M8.8C) this reaction is replaced by reactions involving CH_3 and C_3 .

4.6. *Physical Scenarios That Can (Re)set C/O in the Inner Disk and Implications for Planet Formation*

We have shown that the observations toward J160532 suggest a higher C/O ratio in the inner disk of this source than that for ISO-ChaI 147 when estimations of \mathcal{N} from observations are available for both sources (e.g., C_6H_6 and C_4H_2 ; see bottom panel of Fig. 8). In particular, we found that ISO-ChaI 147 could be consistent with solar, or a moderate enhancement in C/O. However, the picture for J160532 is not as simple, and it strongly depends on the species considered, ranging from solar-like values to highly enhanced C/O ratios. We reiterate again, that our results apply only for a model that has an assumed stellar X-ray luminosity of 10^{29} erg s $^{-1}$, which is in the middle of the observed range for VLMSs (Preibisch & Feigelson 2005). Here we briefly discuss the different mechanisms and events that could lead to an increase in the C/O ratio, due to both carbon grain destruction releasing carbon into the gas phase and oxygen depletion.

Several processes have been proposed to increase the C/O ratio as a consequence of the disk physical and chemical evolution and planet formation, which in synergy increase C/H and decrease O/H. One possible scenario is the presence of the soot line, which is a region within which polycyclic aromatic hydrocarbons (PAHs) and refractory carbon grains are destroyed via thermal reactions, resulting in the sublimation of these species, which injects excess carbon into the gas phase (Kress et al. 2010; van 't Hoff et al. 2020). Note that PAHs toward disks around VLMSs have not been detected with JWST. This is likely related to the weaker UV radiation field in these sources that is unable to excite PAHs, compared with T Tauri and Herbig Ae/Be stars (Geers et al. 2006; Sturm et al. 2024).

Mechanisms to inject excess carbon into the gas phase are (1) carbon being released from the grains to the gas phase by the collisions of hot oxygen atoms with carbonaceous dust grains (Lee et al. 2010), which mainly happens in the disk atmosphere, but the effect is spread through the disk by vertical mixing; (2) oxidation of carbon dust (Finocchi et al. 1997; Gail 2001, 2002), which is the reaction between carbon-rich grains and oxygen-bearing species, such as OH; (3) carbon released from PAHs through destruction by X-ray and high-energy photons (Siebenmorgen & Krügel 2010); and (4) carbon-rich grains being photochemically destroyed by far-UV photons (Alata et al. 2015; Anderson et al. 2017). The sublimation of refractory carbon is proposed to take place in regions with gas temperatures $\gtrsim 500$ K (Li et al. 2021). Reactions of carbon grains with atomic H can also liberate carbon into the gas phase (see Lenzuni

et al. 1995). In our M dwarf physical model (see Fig. 1) the gas temperature in the innermost region (≤ 0.1 au) is $\gtrsim 500$ K, as is that in the inner-disk atmosphere ($z/r \geq 0.1$). Hence, although we assume that carbon grain sublimation has occurred globally in the disk for simplicity, the temperature at which this effect should take place is also aligned with the region of enhanced hydrocarbon formation.

However, there are mechanisms that may destroy carbonaceous grains over a larger spatial area than suggested by the current gas temperature. Episodic accretion events in the early stages of disk formation and evolution due to an increased accretion rate will increase both the gas and dust temperature, pushing outward the snowline and the soot line (Audard et al. 2014; van 't Hoff et al. 2020). Carbon grain destruction is an irreversible process; hence, carbon grains could have been destroyed in an earlier evolutionary phase when episodic accretion is active. That the inner disks could be affected by such processes is hinted at in recent JWST results. Studies comparing JWST and Spitzer observations of disks around T Tauri stars have signs of highly dynamic inner disks, with the observations suggesting a temporal variability in the molecular line emission of species such as C_2H_2 , HCN, H_2O , OH, and CO_2 (Schwarz et al. 2024; Romero-Mirza et al. 2024a). A similar conclusion was made by Kóspál et al. (2023) when comparing the strength of the molecular emission during the quiescent epoch of EX Lup with the outburst event studied by Banzatti et al. (2012).

Wei et al. (2019) investigated this process of carbon grain destruction in a chemical model of a protoplanetary disk around a T Tauri star and proposed that the midplane abundances of HCN, c- C_3H_2 , and LCCs at 1 au are significantly enhanced when using an increased C/O of 1.7 owing to injection of carbon via carbon grain destruction. Other species, such as CH_4 and C_2H_2 , also show a positive response to carbon injection, although the contrast between the oxygen-rich and carbon-rich model is less pronounced. This is accompanied by a decrease in CO_2 , which is a similar trend to that found here (see Figs. F.1 and F.2). Tabone et al. (2023), van Dishoeck et al. (2023), and Arabhavi et al. (2024) proposed this scenario to explain the J160532 and ISO-ChaI 147 observations, suggesting that the increase in C_2H_2 abundance is occurring within the location of the “soot line,” where hydrocarbon grains are destroyed by the sublimation front. Here we tested this scenario by adopting the same assumption of carbon enrichment as Wei et al. (2019). We mimicked the effect of carbon grain destruction in the cases M0.88C, M8.8C, and M88C. However, in our models, we find that carbon

grain destruction is not always necessary to explain the high number of molecules of many hydrocarbons in the inner regions of the disk and that oxygen-depletion-only models are also a possible explanation (see below). This is supported by the fact that some \mathcal{N} ratios, such as $\text{H}_2\text{O}/\text{CO}_2$ and HCN/CO_2 , show that solar and oxygen depletion models (M0.44, M4.4, and M44) have similar results to their counterparts including carbon enrichment (M0.88C and M8.8). Note that this might also be driven by the strong sensitivity of CO_2 to O/H.

A second mechanism to increase C/O is oxygen depletion via the trapping of water-ice-coated pebbles beyond the water snowline. Models have shown that disk substructures such as gaps can trap icy pebbles in the outer disk, resulting in a decrease of the O/H ratio in the inner region of the disk (Kalyaan et al. 2021, 2023). This mechanism was also proposed by Tabone et al. (2023), Kamp et al. (2023), and van Dishoeck et al. (2023) to reproduce the high $\text{C}_2\text{H}_2/\text{H}_2\text{O}$ and $\text{HCN}/\text{H}_2\text{O}$ ratios inferred for disks around VLMSs by Tabone et al. (2023), attributing this to a low water abundance in the inner disk. We tested this scenario by depleting the available oxygen in the models by factors of 10 (M4.4 and M8.8C) and 100 (M44 and M88C). We find that our \mathcal{N} are also sensitive to oxygen depletion, with a particularly strong trend seen in the $\text{C}_6\text{H}_6/\text{CO}_2$ and $\text{C}_4\text{H}_2/\text{CO}_2$ ratios, suggesting oxygen depletion factors as high as 10, with a preference for a depletion of ~ 10 for J160532 and no oxygen depletion for ISO-ChaI 147 (see Fig. 8). However, again, this strongly depends on the species we are focusing on and the sensitivity of our model results to the assumed stellar X-ray luminosity. For example, $\text{C}_2\text{H}_2/\text{CO}_2$ suggests that neither oxygen depletion nor carbon enrichment is necessary to fit the estimations for J160532. Icy pebble trapping in the outer disk may explain these high oxygen depletion values for J160532. However, note that the new estimations for the H_2O column density in J160532 by Arabhavi et al. (2025b) suggest a “less water-depleted” inner disk, with $\text{C}_2\text{H}_2/\text{H}_2\text{O}$ and $\text{HCN}/\text{H}_2\text{O}$ ratios one order of magnitude higher than the upper limit inferred by Tabone et al. (2023).

In Kanwar et al. (2024b) models of the inner-disk composition are presented for two scenarios: one for their canonical C/O ratio of 0.45, and another in which oxygen has been depleted by a factor of ≈ 4 (C/O = 2). They calculated both the maximum column density reached for species of interest and the column density at 0.1 au, taking into consideration the full disk column. They find that C_4H_2 is the only maximum column density that increases significantly when oxygen is depleted, with an increase of a factor of ~ 300 . They also find that their maximum column density of OH decreases by

a factor of ~ 50 . The maximum column densities of all other species increase or decrease by a factor of a few at most. However, Kanwar et al. (2024b) do find that the column density at 0.1 au is very sensitive to C/O. The column densities of CH_3 , C_2H_2 , C_2H_6 , C_4H_2 , C_3H_4 , C_6H_6 , and HCN all increase by several orders of magnitude when oxygen is depleted. In this work, we do not find the same sensitivity for the maximum column densities and the column densities at 0.1 au for the hydrocarbons, with the canonical and C/O = 4.37 results differing by no more than a factor of 10. Differences in the adopted disk structure could explain the discrepancies. It is also possible that differences are due to the adopted chemistry (e.g., we use a gas-grain model) and how it is calculated (e.g., we calculate the chemistry in a time-dependent manner as opposed to assuming a steady state). In addition, we see that smaller hydrocarbons are more rapidly driven into the LCC reservoir in our model, which is likely related to the carbon sink effect.

The scenarios discussed above can result in a high C/O ratio in the inner region of the disk. However, the C/O ratio (and C/H ratio) can increase as a consequence of additional physics in the disk. Booth et al. (2017) and Booth & Ilee (2019) have shown that high metallicities and, in particular, C/O ratios can be reached as a consequence of gas accretion and the growth and radial drift of icy pebbles in the disk (see also Kalyaan et al. 2021, 2023). Mah et al. (2023) also suggest that the C/O ratio in the inner region of disks around VLMSs can increase from substellar to superstellar more rapidly than (after ~ 2 Myr), and up to higher values than, their higher-mass counterparts, T Tauri and Herbig Ae disks. This is a consequence of the close-in snowlines of water and CO_2 in the disks around low-mass stars coupled with the short distances and faster travel speeds for the superstellar C/O material to travel into the inner disk. These scenarios are mimicked by models M8.8C and M88C, which include both carbon enrichment and oxygen depletion. However, our results suggest that the trends in the observations can be reproduced with oxygen depletion or carbon enrichment alone. Furthermore, we see that for ISO-ChaI 147, the $\text{C}_2\text{H}_2/\text{CO}_2$ ratio in Fig. I.1 suggests that C/O > 1 is not always necessary, since the M0.44F and M0.88C results still reproduce observations in the innermost disk ($\lesssim 0.1$ au) and when only regions with gas temperature > 200 K are included.

Another mechanism to increase the C/O ratio is the destruction of gas-phase CO by dissociative ionization with He^+ , combined with radial drift and gas advection, which was recently studied by Sellek & van Dishoeck 2025. In this work, they find that this process would de-

plete O and liberate enough C to be incorporated into hydrocarbons (see [Sellek & van Dishoeck \(2025\)](#) for more details about the reactions). They find that this is more efficient and more likely to happen in a disk with a high ionization rate ($\gtrsim 10^{-17} \text{ s}^{-1}$). Another feature of the disk that would increase the chances of CO depletion is its size; compact disks are more likely to have efficient dust and ice trapping (e.g., [Banzatti et al. 2023](#)), which, as we discussed before, will also increase the C/O ratio. Future studies on the effects of the ionization rate in the formation of hydrocarbons in disks around VLMSs are needed to test these scenarios.

Regarding planet formation, the atmospheric composition of exoplanets is directly linked to the place where they are formed (e.g., [Öberg & Bergin 2021](#); [Öberg et al. 2023](#)). Planets can be formed early or late in the disk lifetime. If they form early in the inner disk, most of the material available to be accreted will have pristine compositions, similar to the host star (i.e., initial abundances of our models), whereas if they form late, the available material will be more similar to the abundances of our results. Therefore, understanding the dominating chemistry within the planet-forming region is key to also comprehending the diversity of chemical compositions of exoplanetary atmospheres. The scenarios explored in this work, mimicking the effects of carbon enrichment and oxygen depletion, will have a direct impact on the atmospheric composition of planets forming in this region.

5. SUMMARY

Recent JWST observations of disks around the low-mass stars reported unexpectedly high abundances of hydrocarbons species in the inner disk (e.g., [Tabone et al. 2021](#); [Arabhavi et al. 2024](#); [Kanwar et al. 2024b](#)), results that are not fully consistent with the currently available models. Motivated by these observations, we revisited the M dwarf chemical models by [Walsh et al. \(2015\)](#) and explored the different physical scenarios proposed by [Tabone et al. \(2023\)](#), [van Dishoeck et al. \(2023\)](#) and [Arabhavi et al. \(2024\)](#) that can lead to oxygen depletion (e.g., icy pebble trapping beyond the snowline) and carbon enrichment (e.g., destruction of carbon grains) and that would increase gas-phase C/O to possibly explain the observations. The C/O ratios ranged from solar values ($C/O = 0.44$) to an extreme case combining carbon enrichment and extreme oxygen depletion ($C/O = 87.47$). Our models indicate that reaching high abundances and numbers of hydrocarbon molecules generally requires a carbon enrichment of at least a factor of 2 and/or oxygen depletion by a factor of 10 or more. In general, we find that the peak abundance, column den-

sity, and number of molecules reached by both hydrocarbons (C_2H_2 , CH_4 , C_6H_6 , C_4H_2 , C_2H_4 , C_3H_4 , C_2H_6 , and CH_3) and nitriles (HCN , HC_3N , and CH_3CN) are sensitive to the C/O ratio, with both oxygen depletion and carbon enrichment increasing the values of the peak abundance and column density in the IR-emitting region. However, the largest relative increases in column density usually occur at moderately enhanced C/O ratios (up to 4.4). Increasing the C/O ratio to higher values (up to 87.47) does not always result in further enhancement. Hence, the chemistry becomes limited by C/H, rather than O/H, and higher depletion factors for oxygen are unlikely to change the results. This may not be true for higher C/H values, although we are already assuming that all carbon that is present in the disk is available in the gas phase by assuming that all carbon grains have been destroyed. To increase C/H further would require some additional mechanism to preferentially deliver carbon, and carbon alone, to the inner disk.

The peak abundance and column densities and number of molecules of O-bearing species (e.g., OH and H_2O) scale almost linearly with oxygen depletion, and their behavior is not as sensitive to C/H. This is true even for the carbon-bearing species CO and CO_2 , whose chemistry is limited more by O/H than C/H.

Overall, we find that the inner-disk chemistry of oxygen- and carbon-bearing species in disks around M dwarf stars can be strongly affected by the C/H and O/H ratios and that nitrogen-bearing molecules are also affected, even though we have used a constant N/H over all models.

Based on the total number of molecules, \mathcal{N} , no single model (i.e., value of C/O) completely fits the trends in the results reported in [Tabone et al. \(2023\)](#), [Arabhavi et al. \(2024\)](#), [Kanwar et al. \(2024b\)](#), and [Arabhavi et al. \(2025b\)](#). However, some molecules do achieve \mathcal{N} close to those inferred from the observations. We find that using the ratio of number of molecules with respect to CO_2 may allow a better discrimination of the underlying C/O in the inner disk. Considering the ratios calculated for the IR-emitting region, we find that a wide range of C/O values are required to reproduce the observed ratios depending on species and source. However, a comparison of the trends in the modeled and observed ratios of total number of hydrocarbons relative to CO_2 suggests that the C/O ratio might not be the same for the inner disk of J160532 and ISO-ChaI 147. This suggests that the systems observed so far show a range of C/O and metallicities even if they present similar species detected in their spectra. Given that the sources discussed here are not unique, our findings indicate that an enhanced C/O could explain the observations of not only J160532,

ISO-ChaI 147, and Sz28 but also the successful detection of abundant hydrocarbons in the disks around other VLMSs (e.g., Arabhavi et al. 2025a; Grant et al. 2025). Note that we use a generic inner-disk model around an M dwarf star with a single value for X-ray luminosity at the middle of the observed range (10^{29} erg s⁻¹). Hence, we cannot rule out any degeneracies that may arise in our results between the assumed accretion rate and X-ray luminosity and C/O ratio. We plan to investigate this in future work.

Finally, as the material available in disks will determine the atmospheric composition of planet formation therein, it is expected that the scenarios explored in this work are setting the initial conditions for planet formation.

ACKNOWLEDGMENTS

J.K.D.-B. acknowledges support from the Science and Technology Facilities Council via a doctoral training grant (grant No. ST/Y509711/1).

C.W. acknowledges financial support from the Science and Technology Facilities Council and UK Research and Innovation (grant Nos. ST/X001016/1 and MR/T040726/1).

EvD acknowledges funding from the European Research Council (ERC) under the European Union’s Horizon 2020 research and innovation program (grant agreement No. 101019751 MOLDISK) and the Danish National Research Foundation through the Center of Excellence “InterCat” (Grant agreement No. DNRF150).

REFERENCES

- Alata, I., Jallat, A., Gavilan, L., et al. 2015, *A&A*, 584, A123, doi: [10.1051/0004-6361/201526368](https://doi.org/10.1051/0004-6361/201526368)
- Anderson, D. E., Bergin, E. A., Blake, G. A., et al. 2017, *ApJ*, 845, 13, doi: [10.3847/1538-4357/aa7da1](https://doi.org/10.3847/1538-4357/aa7da1)
- Arabhavi, A. M., Kamp, I., Henning, T., et al. 2024, *Science*, 384, 1086, doi: [10.1126/science.adi8147](https://doi.org/10.1126/science.adi8147)
- Arabhavi, A. M., Kamp, I., Henning, T., et al. 2025a, *A&A*, 699, A194, doi: [10.1051/0004-6361/202554109](https://doi.org/10.1051/0004-6361/202554109)
- Arabhavi, A. M., Kamp, I., van Dishoeck, E. F., et al. 2025b, *ApJL*, 984, L62, doi: [10.3847/2041-8213/adc692](https://doi.org/10.3847/2041-8213/adc692)
- Arulanantham, N., Salyk, C., Pontoppidan, K., et al. 2025, *AJ*, 170, 67, doi: [10.3847/1538-3881/addr01](https://doi.org/10.3847/1538-3881/addr01)
- Asplund, M., Amarsi, A. M., & Grevesse, N. 2021, *A&A*, 653, A141, doi: [10.1051/0004-6361/202140445](https://doi.org/10.1051/0004-6361/202140445)
- Asplund, M., Grevesse, N., Sauval, A. J., & Scott, P. 2009, *ARA&A*, 47, 481, doi: [10.1146/annurev.astro.46.060407.145222](https://doi.org/10.1146/annurev.astro.46.060407.145222)
- Audard, M., Ábrahám, P., Dunham, M. M., et al. 2014, in *Protostars and Planets VI*, ed. H. Beuther, R. S. Klessen, C. P. Dullemond, & T. Henning, 387–410, doi: [10.2458/azu_uapress_9780816531240-ch017](https://doi.org/10.2458/azu_uapress_9780816531240-ch017)
- Banzatti, A., Pontoppidan, K. M., Salyk, C., et al. 2017, *ApJ*, 834, 152, doi: [10.3847/1538-4357/834/2/152](https://doi.org/10.3847/1538-4357/834/2/152)
- Banzatti, A., Meyer, M. R., Bruderer, S., et al. 2012, *ApJ*, 745, 90, doi: [10.1088/0004-637X/745/1/90](https://doi.org/10.1088/0004-637X/745/1/90)
- Banzatti, A., Pontoppidan, K. M., Carr, J. S., et al. 2023, *The Astrophysical Journal Letters*, 957, L22, doi: [10.3847/2041-8213/acf5ec](https://doi.org/10.3847/2041-8213/acf5ec)
- Bast, J. E., Lahuis, F., van Dishoeck, E. F., & Tielens, A. G. G. M. 2013, *Astronomy & Astrophysics*, 551, A118, doi: [10.1051/0004-6361/201219908](https://doi.org/10.1051/0004-6361/201219908)
- Booth, R. A., Clarke, C. J., Madhusudhan, N., & Ilee, J. D. 2017, *Monthly Notices of the Royal Astronomical Society*, 469, 3994, doi: [10.1093/mnras/stx1103](https://doi.org/10.1093/mnras/stx1103)
- Booth, R. A., & Ilee, J. D. 2019, *MNRAS*, 487, 3998, doi: [10.1093/mnras/stz1488](https://doi.org/10.1093/mnras/stz1488)
- Bruderer, S. 2013, *Astronomy & Astrophysics*, 559, A46, doi: [10.1051/0004-6361/201321171](https://doi.org/10.1051/0004-6361/201321171)
- Cardelli, J. A., Meyer, D. M., Jura, M., & Savage, B. D. 1996, *ApJ*, 467, 334, doi: [10.1086/177608](https://doi.org/10.1086/177608)
- Cardelli, J. A., Savage, B. D., & Ebbets, D. C. 1991, *ApJL*, 383, L23, doi: [10.1086/186232](https://doi.org/10.1086/186232)
- Carr, J. S., & Najita, J. R. 2008, *Science*, 319, 1504, doi: [10.1126/science.1153807](https://doi.org/10.1126/science.1153807)
- . 2011, *ApJ*, 733, 102, doi: [10.1088/0004-637X/733/2/102](https://doi.org/10.1088/0004-637X/733/2/102)
- Cieza, L. A., Schreiber, M. R., Romero, G. A., et al. 2010, *ApJ*, 712, 925, doi: [10.1088/0004-637X/712/2/925](https://doi.org/10.1088/0004-637X/712/2/925)
- Colmenares, M. J., Bergin, E. A., Salyk, C., et al. 2024, *ApJ*, 977, 173, doi: [10.3847/1538-4357/ad8b4f](https://doi.org/10.3847/1538-4357/ad8b4f)
- Du, F., Bergin, E. A., Hogerheijde, M., et al. 2017, *ApJ*, 842, 98, doi: [10.3847/1538-4357/aa70ee](https://doi.org/10.3847/1538-4357/aa70ee)
- Dullemond, C. P., & Monnier, J. D. 2010, *ARA&A*, 48, 205, doi: [10.1146/annurev-astro-081309-130932](https://doi.org/10.1146/annurev-astro-081309-130932)
- Eistrup, C., Walsh, C., & van Dishoeck, E. F. 2016, *Astronomy & Astrophysics*, 595, A83, doi: [10.1051/0004-6361/201628509](https://doi.org/10.1051/0004-6361/201628509)
- Finocchi, F., Gail, H. P., & Duschl, W. J. 1997, *A&A*, 325, 1264
- Franceschi, R., Henning, T., Tabone, B., et al. 2024, *A&A*, 687, A96, doi: [10.1051/0004-6361/202348034](https://doi.org/10.1051/0004-6361/202348034)
- Gail, H. P. 2001, *A&A*, 378, 192, doi: [10.1051/0004-6361:20011130](https://doi.org/10.1051/0004-6361:20011130)
- . 2002, *A&A*, 390, 253, doi: [10.1051/0004-6361:20020614](https://doi.org/10.1051/0004-6361:20020614)

- Garrod, R. T., Wicicus Weaver, S. L., & Herbst, E. 2008, *ApJ*, 682, 283, doi: [10.1086/588035](https://doi.org/10.1086/588035)
- Gasman, D., van Dishoeck, E. F., Grant, S. L., et al. 2023, *A&A*, 679, A117, doi: [10.1051/0004-6361/202347005](https://doi.org/10.1051/0004-6361/202347005)
- Geers, V. C., Augereau, J. C., Pontoppidan, K. M., et al. 2006, *A&A*, 459, 545, doi: [10.1051/0004-6361:20064830](https://doi.org/10.1051/0004-6361:20064830)
- Graedel, T. E., Langer, W. D., & Frerking, M. A. 1982, *ApJS*, 48, 321, doi: [10.1086/190780](https://doi.org/10.1086/190780)
- Grant, S. L., van Dishoeck, E. F., Tabone, B., et al. 2023, *ApJL*, 947, L6, doi: [10.3847/2041-8213/acc44b](https://doi.org/10.3847/2041-8213/acc44b)
- Grant, S. L., Temmink, M., van Dishoeck, E. F., et al. 2025, *A&A*, 702, A126, doi: [10.1051/0004-6361/202555862](https://doi.org/10.1051/0004-6361/202555862)
- Henry, T. J., & Jao, W.-C. 2024, *ARA&A*, 62, 593, doi: [10.1146/annurev-astro-052722-102740](https://doi.org/10.1146/annurev-astro-052722-102740)
- Houge, A., Johansen, A., Bergin, E., et al. 2025, *A&A*, 699, A227, doi: [10.1051/0004-6361/202555164](https://doi.org/10.1051/0004-6361/202555164)
- Kaeufer, T., Woitke, P., Kamp, I., Kanwar, J., & Min, M. 2024, *A&A*, 690, A100, doi: [10.1051/0004-6361/202450891](https://doi.org/10.1051/0004-6361/202450891)
- Kalyaan, A., Pinilla, P., Krijt, S., Mulders, G. D., & Banzatti, A. 2021, *ApJ*, 921, 84, doi: [10.3847/1538-4357/ac1e96](https://doi.org/10.3847/1538-4357/ac1e96)
- Kalyaan, A., Pinilla, P., Krijt, S., et al. 2023, *ApJ*, 954, 66, doi: [10.3847/1538-4357/ace535](https://doi.org/10.3847/1538-4357/ace535)
- Kamp, I., Henning, T., Arabhavi, A. M., et al. 2023, *Faraday Discussions*, 245, 112, doi: [10.1039/D3FD00013C](https://doi.org/10.1039/D3FD00013C)
- Kanwar, J., Kamp, I., Woitke, P., et al. 2024a, *A&A*, 681, A22, doi: [10.1051/0004-6361/202346262](https://doi.org/10.1051/0004-6361/202346262)
- Kanwar, J., Kamp, I., Jang, H., et al. 2024b, *A&A*, 689, A231, doi: [10.1051/0004-6361/202450078](https://doi.org/10.1051/0004-6361/202450078)
- Kanwar, J., Kamp, I., Woitke, P., et al. 2026, *A&A*, 705, A222, doi: [10.1051/0004-6361/202451844](https://doi.org/10.1051/0004-6361/202451844)
- Kóspál, Á., Ábrahám, P., Diehl, L., et al. 2023, *ApJL*, 945, L7, doi: [10.3847/2041-8213/acb58a](https://doi.org/10.3847/2041-8213/acb58a)
- Kress, M. E., Tielens, A. G., & Frenklach, M. 2010, *Advances in Space Research*, 46, 44, doi: <https://doi.org/10.1016/j.asr.2010.02.004>
- Lee, J.-E., Bergin, E. A., & Nomura, H. 2010, *ApJL*, 710, L21, doi: [10.1088/2041-8205/710/1/L21](https://doi.org/10.1088/2041-8205/710/1/L21)
- Lenzuni, P., Gail, H.-P., & Henning, T. 1995, *ApJ*, 447, 848, doi: [10.1086/175922](https://doi.org/10.1086/175922)
- Li, J., Bergin, E. A., Blake, G. A., Ciesla, F. J., & Hirschmann, M. M. 2021, *Science Advances*, 7, eabd3632, doi: [10.1126/sciadv.abd3632](https://doi.org/10.1126/sciadv.abd3632)
- Mah, J., Bitsch, B., Pascucci, I., & Henning, T. 2023, *A&A*, 677, L7, doi: [10.1051/0004-6361/202347169](https://doi.org/10.1051/0004-6361/202347169)
- McElroy, D., Walsh, C., Markwick, A. J., et al. 2013, *A&A*, 550, A36, doi: [10.1051/0004-6361/201220465](https://doi.org/10.1051/0004-6361/201220465)
- Meyer, D. M., Jura, M., & Cardelli, J. A. 1998, *ApJ*, 493, 222, doi: [10.1086/305128](https://doi.org/10.1086/305128)
- Meyer, J. P. 1985, *ApJS*, 57, 173, doi: [10.1086/191001](https://doi.org/10.1086/191001)
- Najita, J., Carr, J. S., & Mathieu, R. D. 2003, *ApJ*, 589, 931, doi: [10.1086/374809](https://doi.org/10.1086/374809)
- Noble, J. A., Theule, P., Borget, F., et al. 2013, *MNRAS*, 428, 3262, doi: [10.1093/mnras/sts272](https://doi.org/10.1093/mnras/sts272)
- Nomura, H., Aikawa, Y., Tsujimoto, M., Nakagawa, Y., & Millar, T. J. 2007, *ApJ*, 661, 334, doi: [10.1086/513419](https://doi.org/10.1086/513419)
- Nomura, H., & Millar, T. J. 2005, *Astronomy & Astrophysics*, 438, 923, doi: [10.1051/0004-6361:20052809](https://doi.org/10.1051/0004-6361:20052809)
- Öberg, K. I., & Bergin, E. A. 2021, *Physics Reports*, 893, 1, doi: [10.1016/j.physrep.2020.09.004](https://doi.org/10.1016/j.physrep.2020.09.004)
- Öberg, K. I., Facchini, S., & Anderson, D. E. 2023, *ARA&A*, 61, 287, doi: [10.1146/annurev-astro-022823-040820](https://doi.org/10.1146/annurev-astro-022823-040820)
- Öberg, K. I., van Broekhuizen, F., Fraser, H. J., et al. 2005, *ApJL*, 621, L33, doi: [10.1086/428901](https://doi.org/10.1086/428901)
- Pascucci, I., Herczeg, G., Carr, J. S., & Bruderer, S. 2013, *ApJ*, 779, 178, doi: [10.1088/0004-637X/779/2/178](https://doi.org/10.1088/0004-637X/779/2/178)
- Penteado, E. M., Walsh, C., & Cuppen, H. M. 2017, *ApJ*, 844, 71, doi: [10.3847/1538-4357/aa78f9](https://doi.org/10.3847/1538-4357/aa78f9)
- Pontoppidan, K. M., Salyk, C., Banzatti, A., et al. 2019, *The Astrophysical Journal*, 874, 92, doi: [10.3847/1538-4357/ab05d8](https://doi.org/10.3847/1538-4357/ab05d8)
- Pontoppidan, K. M., Salyk, C., Bergin, E. A., et al. 2014, in *Protostars and Planets VI*, ed. H. Beuther, R. S. Klessen, C. P. Dullemond, & T. Henning, 363–385, doi: [10.2458/azu_uapress_9780816531240-ch016](https://doi.org/10.2458/azu_uapress_9780816531240-ch016)
- Pontoppidan, K. M., Salyk, C., Blake, G. A., et al. 2010, *ApJ*, 720, 887, doi: [10.1088/0004-637X/720/1/887](https://doi.org/10.1088/0004-637X/720/1/887)
- Preibisch, T., & Feigelson, E. D. 2005, *ApJS*, 160, 390, doi: [10.1086/432094](https://doi.org/10.1086/432094)
- Raul, E., Alarcón, F., & Bergin, E. A. 2025, *ApJ*, 982, 155, doi: [10.3847/1538-4357/adaeae](https://doi.org/10.3847/1538-4357/adaeae)
- Romero-Mirza, C. E., Öberg, K. I., Banzatti, A., et al. 2024a, *ApJ*, 964, 36, doi: [10.3847/1538-4357/ad20e9](https://doi.org/10.3847/1538-4357/ad20e9)
- Romero-Mirza, C. E., Banzatti, A., Öberg, K. I., et al. 2024b, *ApJ*, 975, 78, doi: [10.3847/1538-4357/ad769e](https://doi.org/10.3847/1538-4357/ad769e)
- Salyk, C., Pontoppidan, K. M., Blake, G. A., et al. 2008, *ApJL*, 676, L49, doi: [10.1086/586894](https://doi.org/10.1086/586894)
- Schwarz, K. R., Bergin, E. A., Cleeves, L. I., et al. 2016, *ApJ*, 823, 91, doi: [10.3847/0004-637X/823/2/91](https://doi.org/10.3847/0004-637X/823/2/91)
- Schwarz, K. R., Henning, T., Christiaens, V., et al. 2024, *The Astrophysical Journal*, 962, 8, doi: [10.3847/1538-4357/ad1393](https://doi.org/10.3847/1538-4357/ad1393)
- Sellek, A. D., & van Dishoeck, E. F. 2025, *A&A*, 701, A239, doi: [10.1051/0004-6361/202555195](https://doi.org/10.1051/0004-6361/202555195)
- Siebenmorgen, R., & Krügel, E. 2010, *A&A*, 511, A6, doi: [10.1051/0004-6361/200912035](https://doi.org/10.1051/0004-6361/200912035)
- Sturm, J. A., McClure, M. K., Harsono, D., et al. 2024, *A&A*, 689, A92, doi: [10.1051/0004-6361/202450865](https://doi.org/10.1051/0004-6361/202450865)

- Tabone, B., van Dishoeck, E. F., & Black, J. H. 2024, *A&A*, 691, A11, doi: [10.1051/0004-6361/202348487](https://doi.org/10.1051/0004-6361/202348487)
- Tabone, B., van Hemert, M. C., van Dishoeck, E. F., & Black, J. H. 2021, *Astronomy & Astrophysics*, 650, A192, doi: [10.1051/0004-6361/202039549](https://doi.org/10.1051/0004-6361/202039549)
- Tabone, B., Bettoni, G., van Dishoeck, E. F., et al. 2023, *Nature Astronomy*, 7, 805, doi: [10.1038/s41550-023-01965-3](https://doi.org/10.1038/s41550-023-01965-3)
- Temmink, M., Booth, A. S., Leemker, M., et al. 2025, *A&A*, 693, A101, doi: [10.1051/0004-6361/202452175](https://doi.org/10.1051/0004-6361/202452175)
- van Dishoeck, E. F., Grant, S., Tabone, B., et al. 2023, *Faraday Discussions*, 245, 52, doi: [10.1039/D3FD00010A](https://doi.org/10.1039/D3FD00010A)
- van 't Hoff, M. L. R., Bergin, E. A., Jørgensen, J. K., & Blake, G. A. 2020, *The Astrophysical Journal Letters*, 897, L38, doi: [10.3847/2041-8213/ab9f97](https://doi.org/10.3847/2041-8213/ab9f97)
- Vlasblom, M., van Dishoeck, E. F., Tabone, B., & Bruderer, S. 2024, *A&A*, 682, A91, doi: [10.1051/0004-6361/202348224](https://doi.org/10.1051/0004-6361/202348224)
- Walsh, C., Nomura, H., & van Dishoeck, E. 2015, *Astronomy & Astrophysics*, 582, A88, doi: [10.1051/0004-6361/201526751](https://doi.org/10.1051/0004-6361/201526751)
- Wei, C.-E., Nomura, H., Lee, J.-E., et al. 2019, *ApJ*, 870, 129, doi: [10.3847/1538-4357/aaf390](https://doi.org/10.3847/1538-4357/aaf390)
- Weingartner, J. C., & Draine, B. T. 2001, *ApJ*, 548, 296, doi: [10.1086/318651](https://doi.org/10.1086/318651)
- Woitke, P., Thi, W. F., Arabhavi, A. M., et al. 2024, *A&A*, 683, A219, doi: [10.1051/0004-6361/202347730](https://doi.org/10.1051/0004-6361/202347730)
- Woodall, J., Agúndez, M., Markwick-Kemper, A. J., & Millar, T. J. 2007, *A&A*, 466, 1197, doi: [10.1051/0004-6361:20064981](https://doi.org/10.1051/0004-6361:20064981)
- Woods, P. M., Slater, B., Raza, Z., et al. 2013, *ApJ*, 777, 90, doi: [10.1088/0004-637X/777/2/90](https://doi.org/10.1088/0004-637X/777/2/90)
- Zhang, K., Booth, A. S., Law, C. J., et al. 2021, *The Astrophysical Journal Supplement Series*, 257, 5, doi: [10.3847/1538-4365/ac1580](https://doi.org/10.3847/1538-4365/ac1580)

APPENDIX

A. CAVEATS

There are some model assumptions and caveats we need to take into consideration when interpreting our results. First of all, our disk physical model is not self-consistent. When we change the C/O ratio, we assume a constant temperature structure across our models. We assume this for simplicity, so we are considering only the chemical changes with increasing C/O rather than more complex changes that may occur in the balance between heating and cooling when the metallicity of the gas changes. Note that this assumption is also made in the models presented in Kanwar et al. (2024b), where they explore C/O ratios of 0.45 and 2. Additionally, we are considering a smooth disk, without gas or dust substructures. However, in the models adopting different values of C/O, we are implicitly mimicking the effects that those substructures have, i.e. dust trapping, on the chemistry. We also do not assume that the disk model has an inner rim. If a warm inner rim is the origin of the mid-IR line emission as suggested for the case of EX Lupi in Woitke et al. (2024), the inner rim would be exposed directly to radiation from the central star and may reveal more of the warm molecular reservoir here, which could lead to the high number of molecules estimated from observations. Additionally, our model has a temperature inversion due to viscous heating in the mid-plane, which increases the abundances of hydrocarbons in that region (see Figs. 2, 4, and F.1). However, note that our main analysis focuses only on the IR-emitting region. Nonetheless, it is intended to test the inner-disk chemistry in a passively heated disk in future work.

In this work, we use a generic M dwarf disk model, which means that we are not modeling specifically the star-disk systems studied by Tabone et al. (2023), Arabhavi et al. (2024), Kanwar et al. (2024b), or Kaeufer et al. (2024). However, our M dwarf model properties are similar enough to the stellar and physical properties of J160532, ISO-ChaI 147, and Sz28 (see Tables 1 and 5) to allow a comparison with the data toward these sources. Nevertheless, some differences may be responsible for some of the discrepancies between the model total number of molecules and those derived from the observations. For example, perhaps the disk mass of our model is too low, and that may explain why we underpredict \mathcal{N} in the IR-emitting region. However, the total disk gas mass in our physical model is almost $0.6 M_{\text{Jup}}$ out to 10 au. The disks around the low-mass stars J160532, ISO-ChaI 147, and Sz28 have gas masses of $0.2 M_{\text{Jup}}$

(Tabone et al. 2023), $1.05 M_{\text{Jup}}$ (Arabhavi et al. 2024), and $0.08 M_{\text{Jup}}$ (Kanwar et al. 2024b; Kaeufer et al. 2024), respectively. Franceschi et al. (2024) estimate a total warm H_2 gas mass of J160532 of $2.3 \times 10^{-5} M_{\text{Jup}}$, confined to the emitting area within a radius of 0.033 au. Using our disk surface density at 0.04 au and assuming an emitting area of 0.04 au, we calculated a warm gas mass of $4 \times 10^{-5} M_{\text{Jup}}$, which is only a factor of two higher than that inferred for J160532. Hence, our model disk has a higher mass than either J160532 and Sz28. In addition, the mass distribution in these two low-mass sources may be different, with more mass concentrated in the innermost disk than the model we have adopted here.

A potential explanation for the discrepancy, in particular, in the difference in \mathcal{N} of HCN between our estimations and observations in J160532 is that we could be overestimating the X-ray ionization rate throughout the disk. An increase in the X-ray ionization rate would have the effect of driving more carbon into the nitriles (Walsh et al. 2015; Kanwar et al. 2024a). Note that our results only apply to a source with a single value of X-ray luminosity at the middle of the observed range for VLMSs, and any further conclusion would require new models to test these scenarios. Pascucci et al. (2013) estimate $L_X \sim 6.3 \times 10^{28} \text{ erg s}^{-1}$ for Sz28, which is a factor of only ≈ 1.6 weaker than the X-ray luminosity of our model ($\sim 10^{29} \text{ erg s}^{-1}$). However, it was not possible to compare our model results with \mathcal{N} ratios for that disk, as there is no estimation of $\mathcal{N}_{\text{CO}_2}$ available. Our model numbers of molecules achieve reasonable agreement with those derived for J160532 and ISO-ChaI 147 (depending on the species), which could be due to the similar X-ray luminosity for both sources ($\approx 6.3 \times 10^{28} \text{ erg s}^{-1}$ and $\lesssim 1.1 \times 10^{29} \text{ erg s}^{-1}$, respectively) to that assumed in our model ($10^{29} \text{ erg s}^{-1}$). Our preliminary tests indicate that even lower X-ray luminosities increase hydrocarbon abundances. A full investigation of these effects will be explored in future work.

The chemical network used in this work is extensive, includes both grain- and gas-phase reactions, and has been supplemented with reactions important in hot dense gas, e.g., collisional processes, neutral-neutral reactions that possess a large barrier, and reactions with excited H_2 . The inclusion of gas-grain chemistry is important in disks around such low-mass stars because they are colder than T Tauri disks and their snowlines will lie much closer to the star. We can see evidence of the importance of grain-surface chemistry in the deple-

tion region that emerges around the H_2O snow surface and that is also affected by the C/O ratio.

However, the chemistry follows a bottom-up scheme in that we can only build larger hydrocarbons from smaller species. Most of the column densities and numbers of molecules calculated for the IR-emitting region are lower than those derived from observations (e.g., CH_4 , C_6H_6 , C_2H_4 , and C_3H_4) which could be explained with the inclusion of a top-down chemical scheme, i.e., allowing the injection of carbon and hydrocarbon fragments from the breakdown of larger species, e.g., PAHs.

Finally, we are comparing our model results with numbers of molecules typically estimated using 0D slab models (Tabone et al. 2021; Kanwar et al. 2024b). Additionally, as discussed by van Dishoeck et al. (2023), Kamp et al. (2023), and Arulanantham et al. (2025), 0D slab models are a simplified approximation for the abundance retrieval, assuming a constant temperature and column density for each molecule. However, the physical structure from our model and the abundance map for the different species show that the gas temperature and density of the region where each molecule is abundant are unlikely to be represented by one value only, with emission likely arising over a radial and vertical gradient of the disk (Romero-Mirza et al. 2024b). Thus, this is another caveat to take into account when comparing between our model results with the column densities and number of molecules reported by the literature based on observational data. For instance, the emitting area is well constrained for optically thick emission of C_2H_2 and CO_2 , which means that it is likely not appropriate to compare these observed values with the results over the full radial range since the disk-averaged column density results are likely not representative. For this reason, for further comparison, we include the number of molecules as a function of C/O for the innermost region of the disk model at 0.4, 0.1, and 1 au in Fig. F.4, which may better represent the emitting area estimated from the observations.

However, retrieval models are becoming more complex. For example, Kaeufer et al. (2024) use Bayesian analysis and multiple 1D emission components in their abundance retrieval method and estimate higher column density values than those reported by Kanwar et al. (2024b) for the same source (Sz28). Future more sophisticated methods for abundance retrieval from observations using 2D models may use our models for comparison. Alternatively, generating directly the IR spectra from our 2D models, as done with other chemical models such as ProDiMo (e.g., Kanwar et al. 2024a) and DALI (e.g., Tabone et al. 2024), would provide another approach for interpreting observations.

B. VERTICAL DISTRIBUTIONS

Figures B.1, B.2, B.3, B.4 show the vertical distribution of the ionization rate, gas temperature, and total abundance of a set of carbon-, nitrogen-, and oxygen-bearing species. The vertical distributions for two radii of the disk (0.1 and 1 au) are presented.

C. QUANTITATIVE DESCRIPTIONS OF THE ABUNDANCE AND COLUMN DENSITY VARIATIONS FOR C_xH_y WITH C/O

In the main text, we present a summary of the behavior of C_xH_y with increasing C/O because the members of this group of species can exhibit similar responses to the change in metallicity. Here we provide a more quantitative description of how each individual species responds to the change in C/O.

C_2H_2 —The abundance distribution of C_2H_2 follows the general pattern as described in Section 3 with two reservoirs. The fractional abundance is high in the upper layers, where the temperature ranges from 300 to 3000 K, reaching a peak of $\sim 10^{-5}$ to 10^{-4} depending on the model. However, as we will later see in most of the species’ abundances, there is a correlation of the spatial extent over which the peak abundance is reached in the IR-emitting region with O/H and C/H separately, but not necessarily with C/O. Figures 2, B.1, and B.3 show that from model M0.44F (the fiducial model) to M0.88C (carbon enrichment), in which C/O increases from 0.44 to 0.88, the vertical width of the region over which C_2H_2 reaches its peak abundance expands. For the model in which we deplete oxygen by a factor of 10 (M4.4), leading to a C/O of 4.37, we also see that the peak abundance region is broader in vertical extent than that for the fiducial model. However we do see C_2H_2 reaching its peak abundance over a greater vertical extent and/or reaching a value ~ 10 times higher in the IR-emitting region for the carbon-enriched cases (M0.88C, M8.8C, and M88C) than for the models with oxygen depletion alone (M0.44F, M4.4, and M44). In conclusion, it appears that excess carbon and an increase in the C/H ratio lead to more efficient synthesis of C_2H_2 in the IR-emitting region.

The radial extent of the midplane reservoir of C_2H_2 is also affected by the increase in C/O. Whilst the peak fractional abundance here is not as high as reached in the disk atmosphere ($\sim 10^{-6}$ to 10^{-5}), increasing the C/O ratio first by carbon enhancement (M0.88C) extends the midplane reservoir from $\lesssim 0.1$ to $\lesssim 0.2$ au. An increase in C/O through oxygen depletion alone (M4.4) leads to the midplane reservoir extending out to $\lesssim 0.3$ au. The combined model (M8.8C) and further increases in C/O, do not significantly extend this reservoir further. Hence,

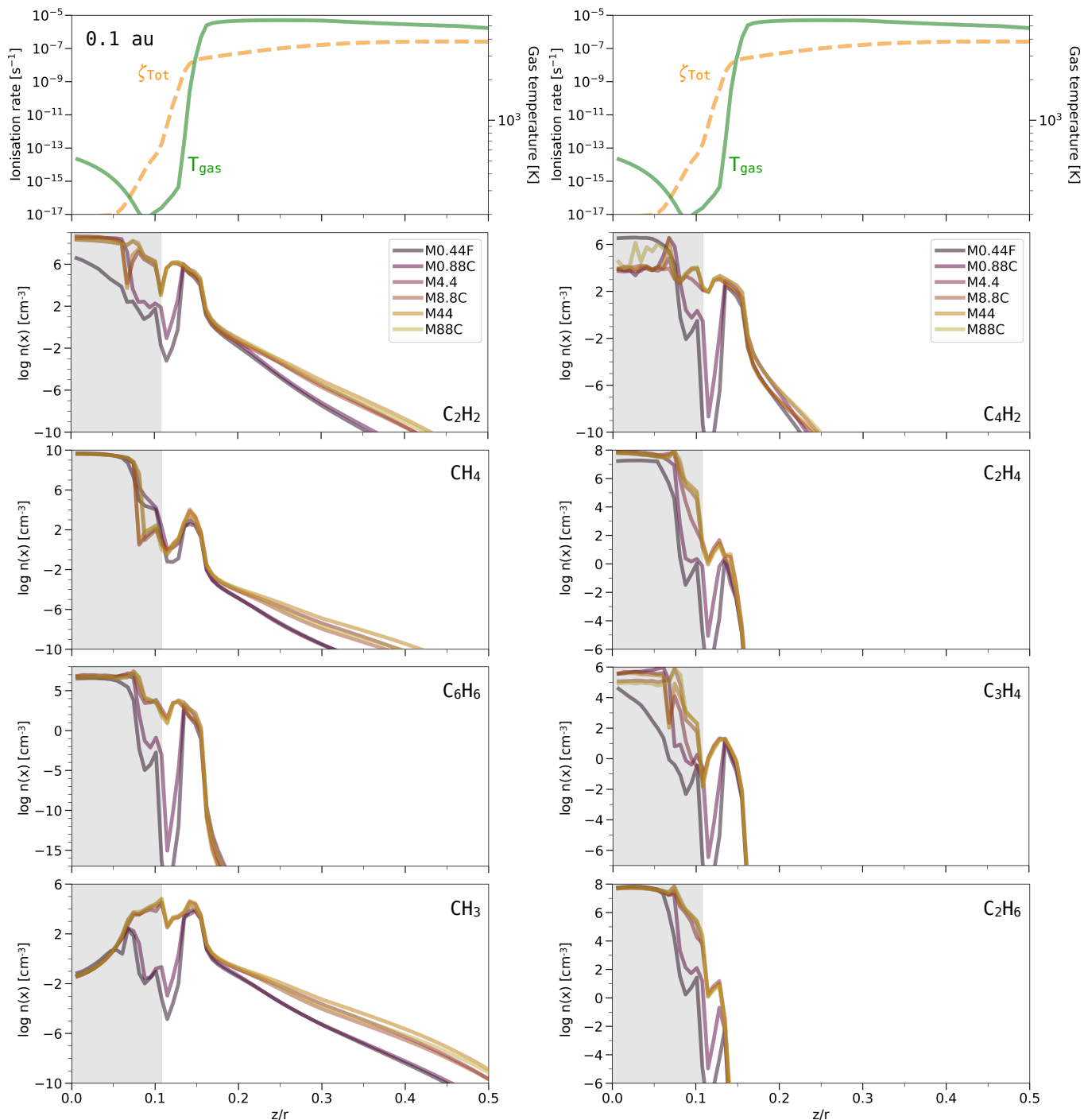


Figure B.1. First row: vertical distribution of the ionization rate (orange dashed curve) and gas temperature (green solid curve) at 0.1 au. Second to fifth rows: vertical distribution of the total abundance of the hydrocarbons: C_2H_2 , CH_4 , C_6H_6 , CH_3 , C_4H_2 , C_2H_4 , C_3H_4 , and C_2H_6 . The different colors represent the different models. The shaded region represents the z/r at which the dust photosphere at 14 μm is defined at that radius r .

an increase in C/O in the disk midplane does allow more efficient synthesis of C_2H_2 , but only out to a radius of ~ 0.3 au.

The behavior with C/O for C_2H_2 is reflected in the calculated column density shown in Fig. 3. The column density profile of C_2H_2 in the IR-emitting region is generally smooth, with a gentle increase in column density within ~ 1 au, by up to one order of magnitude, reaching a peak at the innermost point in our model (0.04 au).

The biggest increase in the column density in the IR-emitting region in the inner disk comes in the first three perturbations (enhancing C, C/O = 0.87; depleting O, C/O = 4.37; and both, C/O = 8.75). In the outer disk, the behavior is different. Here we see the column density increasing by a factor of ~ 2 when enhancing carbon (M0.88C, M8.8C, and M88C) with respect to their counterparts with oxygen depletion only (M0.44F, M4.4, and M44, respectively). This suggests that C/H becomes the limiting factor in setting the amount of C_2H_2 that can be synthesized in the disk.

C_6H_6 —The peak abundance of C_6H_6 in the disk atmosphere is lower than that for the hydrocarbons considered thus far, reaching a peak value of $\sim 10^{-8}$ in the disk atmosphere and midplane in the fiducial model (M0.44F). The spatial distribution exhibits the same double-component morphology as C_2H_2 . The abundance resides in a narrow layer in the disk atmosphere (see Fig. 2), which becomes wider in vertical extent when C/O increases from 0.44 (M0.44F) to 0.87 (M0.88C). The response of the C_6H_6 abundance to initial abundances is nonlinear with C/O, similar to that found for C_2H_2 . When an oxygen depletion factor of 10 is applied (M4.4), the C_6H_6 peak abundance region moves downward vertically compared to that for M0.44F; however, if the oxygen depletion factor increases to 100 (M44), the layer does not vary in vertical extent compared to M4.4 but remains broader than the fiducial model (M0.44F). This effect is also observed in the M8.8C and M88C scenarios, where the C_6H_6 peak fractional abundance increases compared with the fiducial model, and over a broader layer, in response to carbon enrichment. However, the two more extreme C/O ratios considered here (44 and 88) do not lead to the synthesis of significantly more C_6H_6 than found in the two moderate cases (4.4 and 8.8). For the midplane component, again, the first perturbation has the biggest effect: the midplane reservoir of C_6H_6 increases in radial extent from $\lesssim 0.2$ au in the fiducial model (M0.44F) out to $\lesssim 0.3$ au for all other cases.

In the column density profiles for C_6H_6 in Fig. 3, the initial abundances have an impact across the disk. The column density integrated over the IR-emitting region

in the outer disk, $\gtrsim 1$ au, ranges from $\ll 10^{12}$ cm^{-2} (M0.44F) to $\lesssim 10^{13}$ cm^{-2} (M88C). In the inner disk, the column density reaches a peak of $\sim 10^{15}$ cm^{-2} in all models within 0.05 au. Beyond 0.1 au, oxygen-rich models drop by almost two to three orders of magnitude (M0.44F and M0.88C, respectively). On the other hand, the column densities in the carbon-rich models decrease moderately by an order of magnitude and drop again beyond 1 au.

C_4H_2 — C_4H_2 exhibits the same abundance pattern as C_2H_2 and C_6H_6 (see Fig. 4). The fractional abundance in the fiducial model (M0.44F) peaks with a value $\sim 10^{-8}$ in the upper layers of the disk, where the temperature exceeds around 1000 K. The midplane reservoir reaches a similar peak value and extends out to ~ 0.2 au in the fiducial model. For higher C/O ratios, the layer where the abundance peaks extends vertically, similar to that found for C_2H_2 , C_6H_6 , and CH_3 . The cases in which C/H increases and O/H decreases (M8.8C and M88C) show a more vertically extended peak abundance region compared with the M0.88C model, where only carbon enrichment is considered. The molecular reservoir in the midplane also varies in shape and extent as C/O increases. There is a radial expansion from ~ 0.2 au (M0.44F) to ~ 0.7 au (M88C) combined with a drop in the peak abundance in the midplane. In these scenarios, it appears that increasing carbon and/or depleting oxygen increases the destruction rate (or slows down the production rate) of C_4H_2 in the disk midplane, with the conditions present therein likely sequestering carbon into other carriers. As we will discuss later, both C_2H_4 and C_2H_6 show the opposite behavior, lending credence to this theory.

The column density profiles in Fig. 3 reflect these variations in C_4H_2 abundance across the full radial extension.

C_2H_4 —The behavior of C_2H_4 is similar to C_2H_2 in its abundance distribution and is similar to CH_4 in that the midplane component reaches a larger peak fractional abundance than that in the disk atmosphere. The fractional abundance of C_2H_4 in the innermost region of the disk within ~ 0.2 au and below $z/r \approx 0.1$, reaches values of $\sim 10^{-7}$ in the fiducial model. On the other hand, the fractional abundance in the region where the temperature is $\sim 500 - 1500$ K reaches values of $\sim 10^{-10}$ within ~ 7 au, and then increases almost two orders of magnitude in the outermost region. As the C/O ratio increases, this region expands vertically and the peak abundance increases by around one order of magnitude (model M0.88C). The peak abundance in the innermost

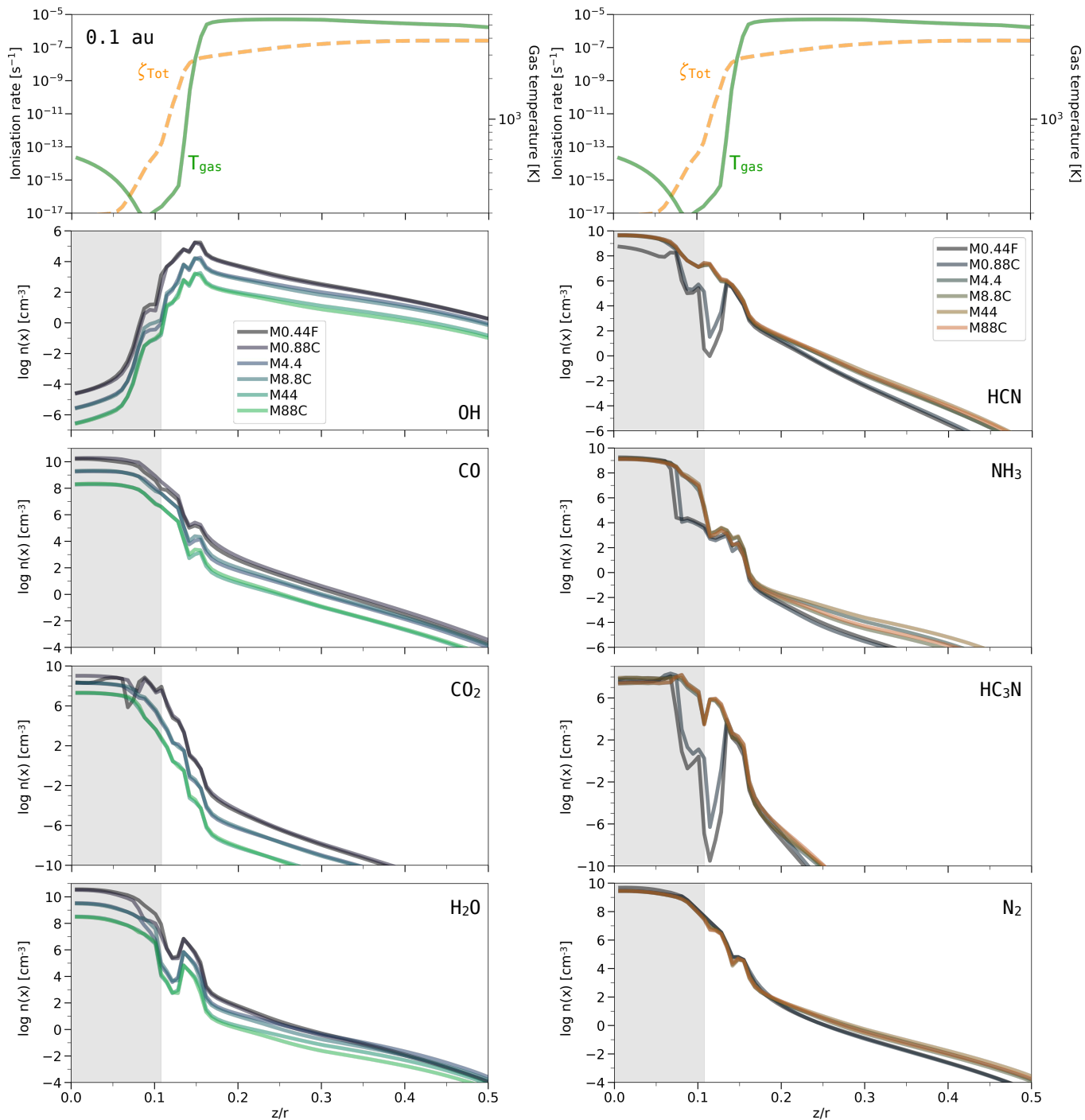


Figure B.2. Same as Fig. B.1, but for the oxygen (OH, CO, CO $_2$, and H $_2$ O) and nitrogen-bearing species (HCN, NH $_3$, HC $_3$ N, and N $_2$) at 0.1 au.

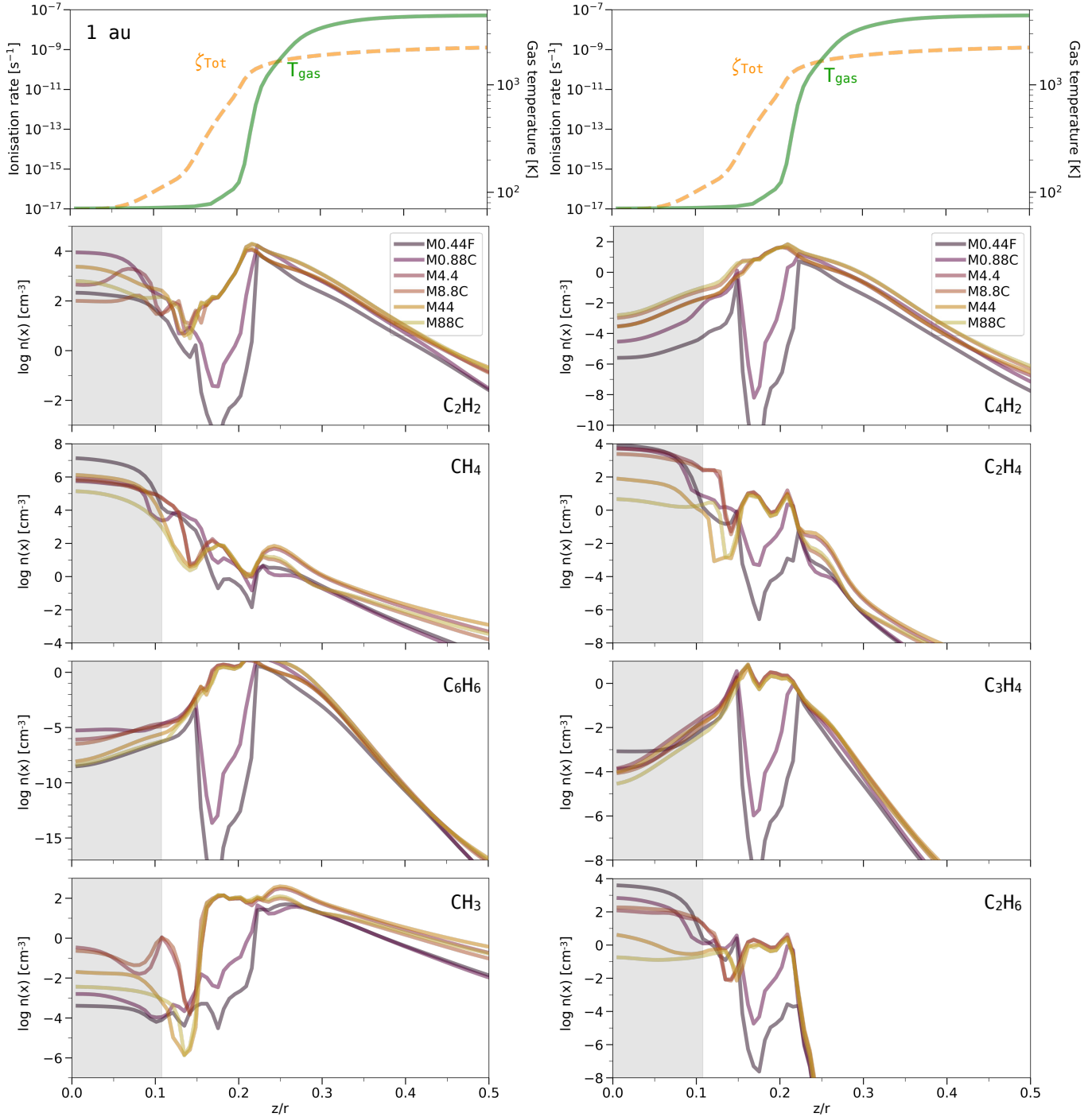


Figure B.3. Same as Fig. B.1, but at 1 au.

midplane region also radially expands from ~ 0.2 au (M0.44F) to ~ 0.5 au (M4.4 and higher C/O models).

We see for the M0.44F model in Fig. 3, that the column density over the IR-emitting region peaks at $\sim 10^{15} \text{ cm}^{-2}$ at ~ 0.04 au but is $\ll 10^{12} \text{ cm}^{-2}$ beyond 0.8 au. As the C/O ratio increases, the column density profiles reach higher values through the innermost disk (up to 10^{16} cm^{-2} for M88C) within ~ 0.1 au

and then decrease by around four orders of magnitude beyond 0.8 au.

C_3H_4 —The fractional abundance of C_3H_4 (propyne) follows a similar behavior to C_2H_4 , with a peak abundance in the atmosphere of $\sim 10^{-9}$. In the oxygen-rich models (M0.44F and M0.88C), C_3H_4 is abundant again only in a very narrow layer that expands in vertical ex-

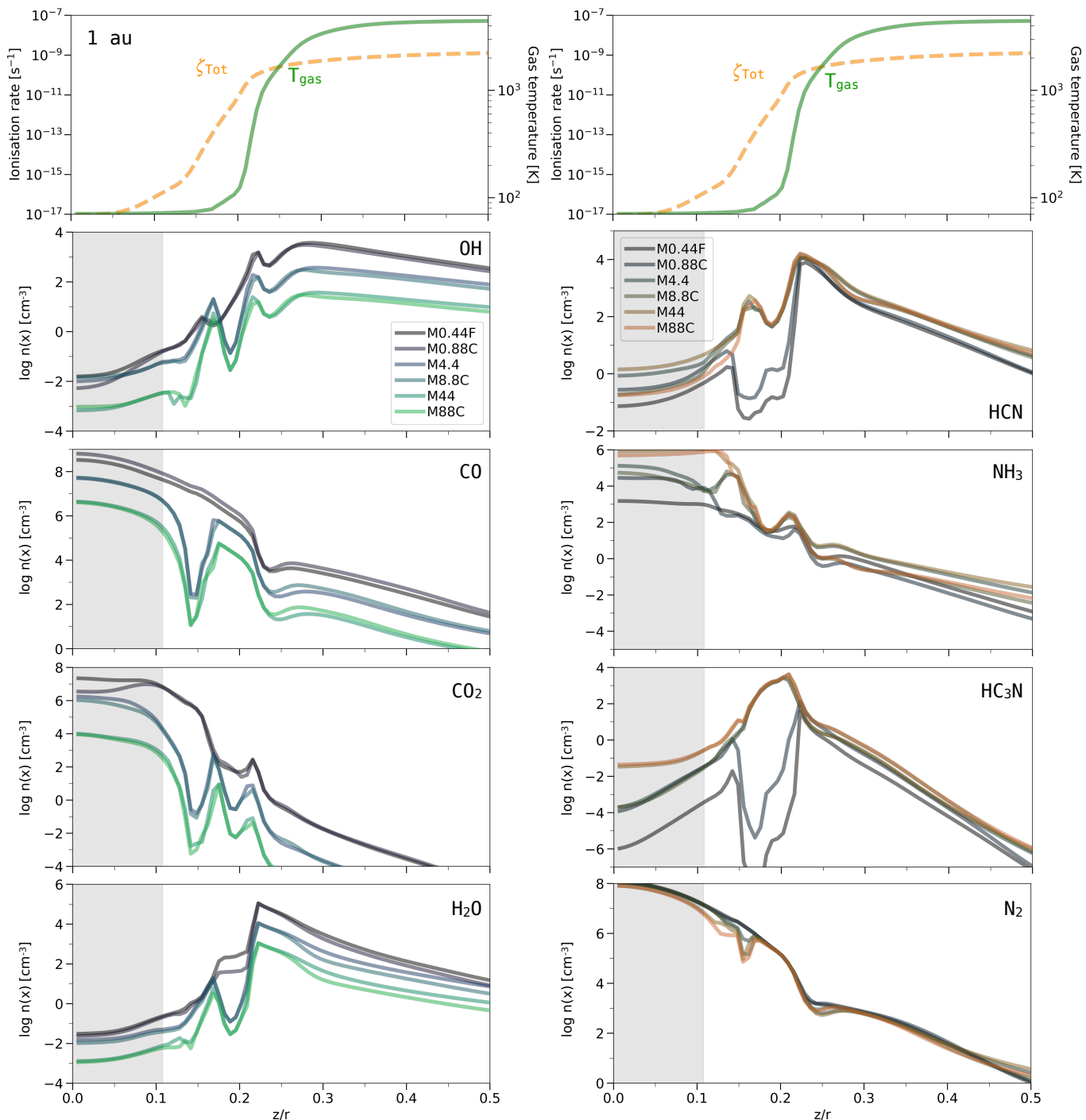


Figure B.4. Same as Fig. B.2, but at 1 au.

tent with increasing C/O. For the C/O scenarios above unity, the peak abundance value does not vary. On the other hand, the abundance in the midplane component increases by at least an order of magnitude when C/O increases.

In general, the column density across the IR-emitting region increases with increasing C/O, reaching values higher than 10^{12} cm^{-2} between ~ 0.05 and ~ 0.1 au for

C/O > 8.8 . Regarding the column density profiles, the differences between the cases where oxygen depletion is included with and without carbon enhancement (e.g., M4.4 and M8.8C or M44 and M88C) vary depending on the case. For example, for the moderate C/O models (M4.4 and M8.8C), we see that in the innermost region M8.8C reaches higher column density values than M4.4 by at least an order of magnitude. On the other hand,

for the more extreme C/O cases (M44 and M88C), the difference between those results is very subtle, similar to what we see in the other hydrocarbon cases.

C_2H_6 — C_2H_6 is also similar to CH_4 in that its peak abundance is reached in the midplane (see Fig. 4). C_2H_6 reaches a peak between 10^{-6} and 10^{-5} (depending on the model) in the innermost region of the disk midplane within a radius of ≈ 0.4 au, where the gas temperature is 150 – 500 K across all models (see Fig. 4). The very innermost region (within 0.07 au) is depleted in C_2H_6 , with the carbon preferring to be in C_2H_2 and CH_4 (see Fig. 4). When C/O increases, the abundance of C_2H_6 also increases in the disk atmosphere around $z/r \sim 0.2$ –0.4, reaching a peak abundance of $\sim 10^{-7}$ in the outer-disk region ($\gg 0.1$ au).

This is reflected in the calculated column density shown in Fig. 3, where the peak column density in the IR-emitting region increases from $\sim 10^{14}$ cm^{-2} in the fiducial model to $\sim 10^{16}$ cm^{-2} in the model M4.4 (and in models with higher C/O ratios) within ~ 0.2 au. Beyond ~ 0.2 au, there is no distinguishable variation in the column density, with values $\lesssim 10^{12}$ cm^{-2} in all models.

D. VARIATIONS IN MIDPLANE RESERVOIR SIZE

Figure D.1 illustrates the midplane sizes for those molecules that have a midplane reservoir, which varies radially and/or in the peak abundance reached when C/O increases. We show the results for two values of C/O only, 0.44 and 8.75, to illustrate the behavior and give a qualitative idea of the response of the extent and abundance of the midplane reservoir to the C/O variation. The midplane size was estimated by eye, based on where the abundance varies by a factor of 10 or more. For simplicity, we consider only the outer radius of the reservoir, which means that we do not capture radial variations in this simple illustration.

As discussed previously, there are two common variations for hydrocarbons: a radial expansion and an increase in the peak abundance value as C/O increases. CH_4 does not follow the same behavior, and the peak abundance in the midplane distribution instead shrinks from ~ 1.2 au to ≈ 0.45 au. In addition, the peak abundance of C_4H_2 drops by a factor of ~ 10 as C/O increases, despite an increase in the radial range over which the peak value is reached. For oxygen carriers such as CO, CO_2 , and H_2O , the radial extent does not vary as C/O increases; however, the peak abundance of all three species decreases by a factor of 10 – 100 as C/O changes from 0.44 to 8.75. Finally, for nitrogen-bearing species, all midplane reservoirs expand radially by a small amount, ≈ 0.1 au. The peak abundance for

HCN and CH_3CN also increases with increasing C/O. That for NH_3 , HC_3N , and HNC have a similar peak abundance for both values of C/O. Note that, as mentioned in Appendix A, our model has a temperature inversion in the midplane owing to viscous heating. However, these results are useful to compare with radial drift and accretion models, which are typically confined to the midplane (e.g., Sellek & van Dishoeck 2025).

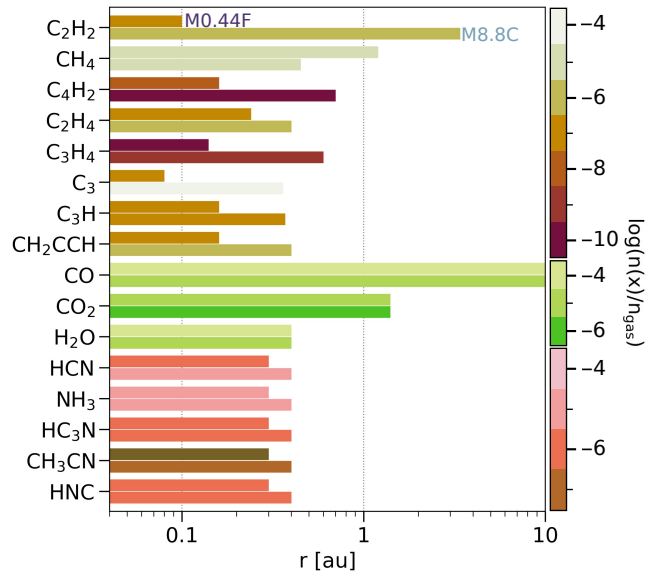


Figure D.1. Midplane radial ranges for those species that show a variation in the size and abundance in the midplane reservoir, using similar color palettes to those in Figs. 2, 5, and 6 for hydrocarbons and oxygen and nitrogen carriers, respectively. The two bars represent the midplane radial extension and abundance for M0.44F (top) and M8.8C (bottom), respectively.

E. POTENTIALLY OBSERVABLE SPECIES

Other hydrocarbons and nitrogen-bearing species have been proposed to be potentially observable in the inner region of the disk. Figures E.1 and E.3 show the fractional abundance maps for C_2 , C_2H , C_3 , C_3H , CH_2CCH , CH_3CN , and HNC. Figure E.2 show the column density profiles for the same set of species. Figure F.3 shows the total number of molecules integrated over the full disk model (out to 10 au) as a function of the C/O ratio.

As shown in Figs. E.1 and E.2, the abundances and column densities of C_3 are particularly enhanced when C/O increases, for example, the abundance is $\sim 10^{-4}$ in both the disk midplane and the IR-emitting region when C/O is greater than 0.44. One caveat of the chemical network used here is that the chemistry does not include processes that lead to full saturation of species that contain three or more carbon atoms. Whilst the predictions

for the IR-emitting region are likely robust, it is recommended to treat with caution the predictions for the disk midplane, where the temperatures and pressures should tend to move the chemistry toward equilibrium. The same is true for species with a higher number of carbon atoms (> 3). Figures E.1 and F.3 also show that the C_2 and C_2H abundance distribution is confined to the IR-emitting region, similar to that for CH_3 and OH .

F. TOTAL NUMBER OF MOLECULES WITH RESPECT TO C/O

Figures F.1, F.2, and F.3 show the total number of molecules over the full disk model out to 10 au for all the key species discussed in this work and potentially observed species, as a function of C/O ratio. These plots show nicely the general trends in total number of molecules, \mathcal{N} , with C/O as discussed in the text. The horizontal dashed and dotted lines represent the derived number of molecules for the optically thin and thick components, respectively, for J160532, ISO-ChaI 147, and Sz28 (Tabone et al. 2023; Arabhavi et al. 2024; Kanwar et al. 2024b; Kaeufer et al. 2024; Arabhavi et al. 2025b). Figure F.4 shows the same estimation at 0.04, 0.1, and 1 au of a subset of species (C_2H_2 , C_6H_6 , CO , CO_2 , H_2O , and HCN). We also include the \mathcal{N} calculations for the integration down to the dust photosphere at $14 \mu\text{m}$. This is because in some cases (e.g., CH_4 and C_2H_6) the abundance in the region below $T_{\text{gas}} = 200$ K and above the dust photosphere at $14 \mu\text{m}$ is not negligible. However, for other species, such as C_6H_6 and C_2H_4 , \mathcal{N} values are more similar to the estimations that include only the IR-emitting region.

G. SUMMARY OF M DWARF SYSTEMS OBSERVED WITH JWST

Table 4 summarizes the inferred number of molecules for the same sources reported by Tabone et al. (2023), Arabhavi et al. (2024), Kanwar et al. (2024b), and Kaeufer et al. (2024). Table 5 presents the star-disk system physical properties for the J160532, ISO-ChaI 147, and Sz28 disks.

H. TEMPERATURE DISTRIBUTION OF MOLECULES IN THE IR-EMITTING REGION

In Section 4.1 we discussed the observational trends of the excitation temperatures reported for the species detected in each disk. In this appendix, we focus on the results of our models regarding the gas temperature distribution for each molecule. We conducted this analysis

to check and compare whether or not the temperature of the region in which the molecules are mainly present in the disk is consistent with the excitation temperature derived from the observations. Note that the gas temperature structure is not recalculated for different elemental abundances (see Appendix A); therefore, the temperature variation with C/O discussed below should be taken with caution. Figure H.1 presents histograms of the number of molecules as a function of gas temperature for C_2H_2 , H_2O , and HCN according to the C/O ratio. We choose these species because they have slightly different behavior in their temperature distribution with the C/O variations. Note that we do not plot the equivalent data for CO_2 because our model predicts that the majority of CO_2 molecules reside at low temperatures, less than 250 K. That the observations derive excitation temperatures for CO_2 generally higher than this requires further investigation.

C_2H_2 —From Fig. H.1, we see that the bulk of C_2H_2 has a higher peak gas temperature between 1000 and 1750 K in the oxygen-rich cases (M0.44F and M0.88C) than in the carbon-rich cases, where a large fraction of C_2H_2 molecules also reside at low gas temperatures ($\lesssim 500$ K). When the C/O increases to > 1 , two distinct components at different temperatures appear. The colder component peaks between 200 and 600 K with a number of molecules of $\sim 5 \times 10^{43}$. The peak temperature in this component remains constant for higher C/O ratio. On the other hand, the peak temperature of the hotter component oscillates when increasing C/O ratios (~ 100 K between models). The number of C_2H_2 molecules in the same component also varies depending on the model; for oxygen-depleted-only models (M4.4 and M44), \mathcal{N} is $\lesssim 5 \times 10^{43}$ K, while for the carbon-enriched and oxygen-depleted models (M8.8C and M88C), it is nearly two times higher. From Fig. 7, the excitation temperature of C_2H_2 is 325 K in ISO-ChaI 147, to 425 K in Sz28, and 400 and ~ 525 K for the thin and thick components of J160532, respectively. Comparing with our gas temperature distributions, only for the carbon-rich cases is there a large fraction of C_2H_2 sitting in the colder region of the disk, which is more consistent with the excitation temperature from the observations. This is complementary evidence for the disks having a C/O > 1 in the IR-emitting regions of the disk. Note that the oxygen-depleted-only models (M4.4 and M44) have fewer molecules residing at high temperature (> 500 K) than those with carbon enrichment, which suggests that the models with carbon enrichment and oxygen depletion (M8.8C and M88C) may overestimate the abundance of C_2H_2 present in the hot molecular layer.

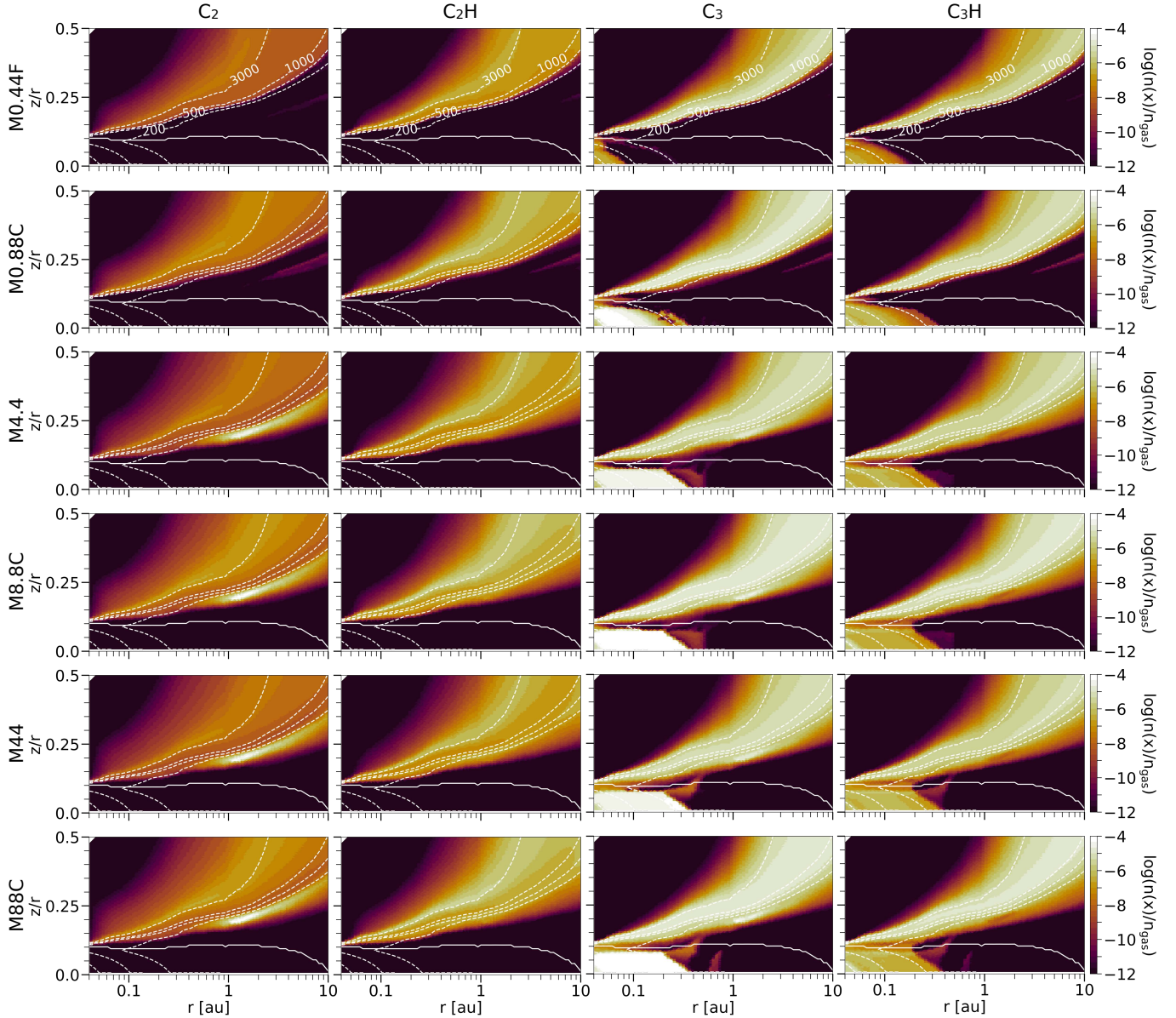


Figure E.1. Same as Fig. 2, but for the potentially observable species C_2 , C_2H , C_3 , and C_3H .

H_2O —The gas temperature distribution for water suggests that this molecule is more abundant at high temperatures, ranging from 1250 to 1750 K for the fiducial and carbon-enriched-only models (M0.44F and M0.88C). Once C/O exceeds 1, the shape of the histogram changes to a skewed Gaussian-like shape, peaking at ~ 1500 K. Compared with C_2H_2 the overall temperature distribution of H_2O does not significantly change with increasing C/O and only the total number of molecules is affected. From Fig. 7, the excitation temperature of H_2O ranges from 300 K in ISO-ChaI 147 to 525 K in J160532. In general, our models predict higher temperatures for H_2O .

HCN —The HCN gas distribution has a similar behavior to the hydrocarbon C_2H_2 . For $C/O < 1$, the histogram has a Gaussian-like shape, peaking between 1000 and 1750 K. For $C/O > 1$, the histogram changes to a skewed Gaussian-like shape, with M8.8C peaking between 750 and 1500 K, and M4.4 at 1250 – 1500 K. For the most extreme C/O values (~ 43.72 and ~ 87.47), two components appear. The colder component peaks at the lower end of the gas temperature, around 50 – 75 K. The hotter component for M44 and M88C remains similar in distribution to that for M4.4 and M8.8C, respectively. From Fig. 7, the excitation temperature of HCN is around 400 K in J160532. Our models predict a colder

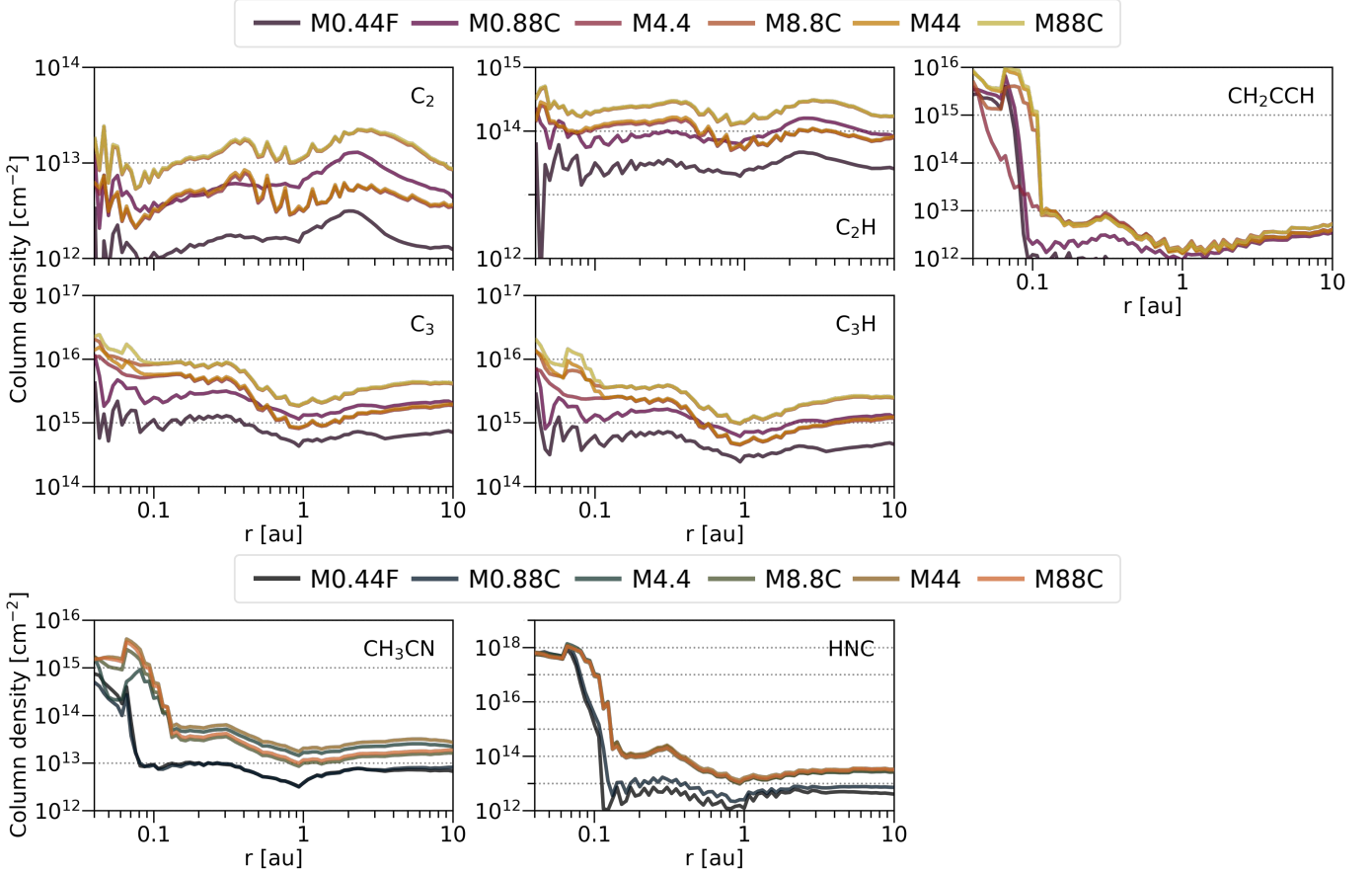


Figure E.2. Same as Fig. 3, but for the potentially observable species C_2 , C_2H , C_3 , C_3H , CH_2CCH , CH_3CN , and HNC . (The complete figure set (2 images) is available in the online article.)

and hotter component; however, neither of those peaks at ~ 400 K.

Other species—The histograms for other species detected in J160532, ISO-ChaI 147, or Sz28, such as C_2H_4 , C_4H_2 , C_6H_6 , C_3H_4 , and CH_4 , are not presented because their gas temperature distributions are somewhat similar to those presented before. For example, C_6H_6 shows a similar distribution to C_2H_2 , with a peak in the number of molecules at higher temperatures in the M8.8C model. Other molecules, namely C_2H_4 , C_4H_2 , C_3H_4 , and CH_4 , are mostly abundant in colder regions ($\lesssim 250$ K), similar to the cold component of HCN in the oxygen-poor models. Additionally, we find that as C/O increases C_6H_6 , C_4H_2 , CH_4 , and C_3H_4 have an increasing fraction of molecules at higher temperatures ($\sim 500 - 2000$ K) in the carbon-enriched cases, whereas C_2H_4 does not. The temperatures predicted for $C/O < 1$ are higher than those estimated from the observations, which in most cases remains true for carbon-rich scenarios. However, as C/O increases, the average temperature of C_2H_4 in the IR-emitting region reaches similar values to those observed in ISO-ChaI 147. For CH_4 , when C/O in-

creases owing to oxygen depletion (M4.4 and M44), the average temperature in the IR-emitting region is almost 400 K higher than their counterpart’s models with carbon enrichment (M8.8C and M88C).

I. COLUMN DENSITY RATIOS AND RADIAL INTEGRATION SENSITIVITY

Figure I.1 presents the C_2H_2/CO_2 ratio as function of radius (top panel) and the \mathcal{N} ratio as a function of radius, when the integration radius varies (bottom panel).

J. LONG CARBON CHAINS IN THE IR-EMITTING REGION

Figure J.1 presents pie charts showing the percentage contribution of long-carbon chains (LCC) to the total LCCs reservoir in the carbon budget for the IR-emitting region. Figures J.2 and J.3 show the fractional abundance maps for the set of LCCs with higher abundance in this category (C_9H_2 , $C_{10}H_2$, CH_3CCH ice, CH_2CCH_2 ice, HC_5N , HC_7N , HC_9N , and HC_3N ice).

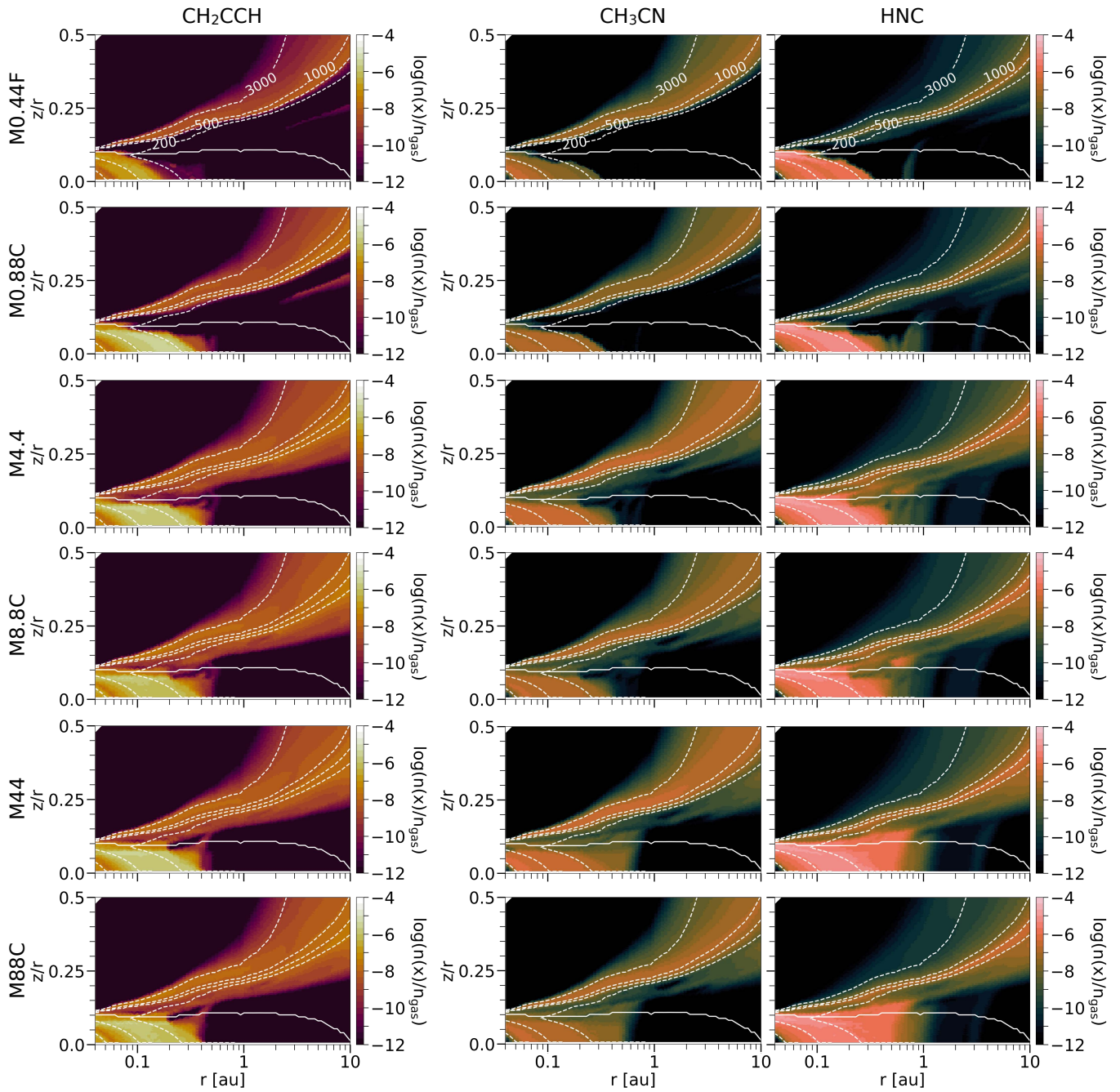


Figure E.3. Same as Fig. 2, but for the potentially observable species CH_2CCH , CH_3CN , and HNC .

K. FORMATION PATHWAYS FOR C_6H_6 AND C_4H_2

Figure K.1 illustrates the dominant gas-phase reactions controlling the formation of C_6H_6 and C_4H_2 at $r = 1$ au and $z/r = 0.23$ in the models M0.44F and M8.8C.

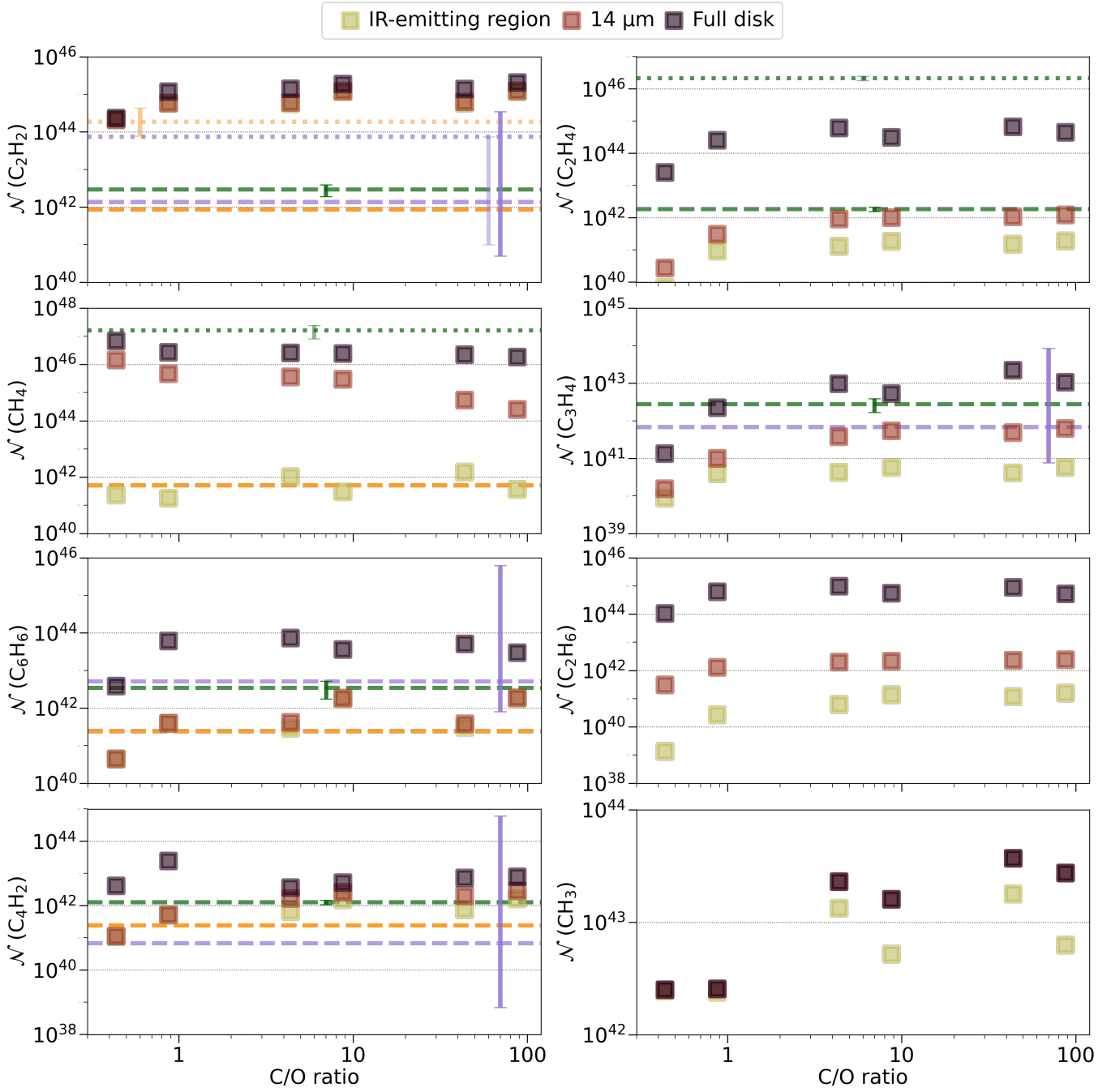


Figure F.1. Number of molecules (integrated over 10 au) for the hydrocarbon species (C_2H_2 , CH_4 , C_6H_6 , C_4H_2 , C_2H_4 , C_3H_4 , CH_3 , and C_2H_6) as a function of C/O. The different colors from light to dark represent the integration over the IR-emitting region, down to the dust photosphere at 14 μm , and over the full disk. The orange, green, and purple horizontal dashed lines represent the number of molecules reported for J160532, ISO-ChaI 147, and Sz28, respectively, for the optically thin component. If available, the optically thick component is represented by horizontal dotted lines for the same disks.

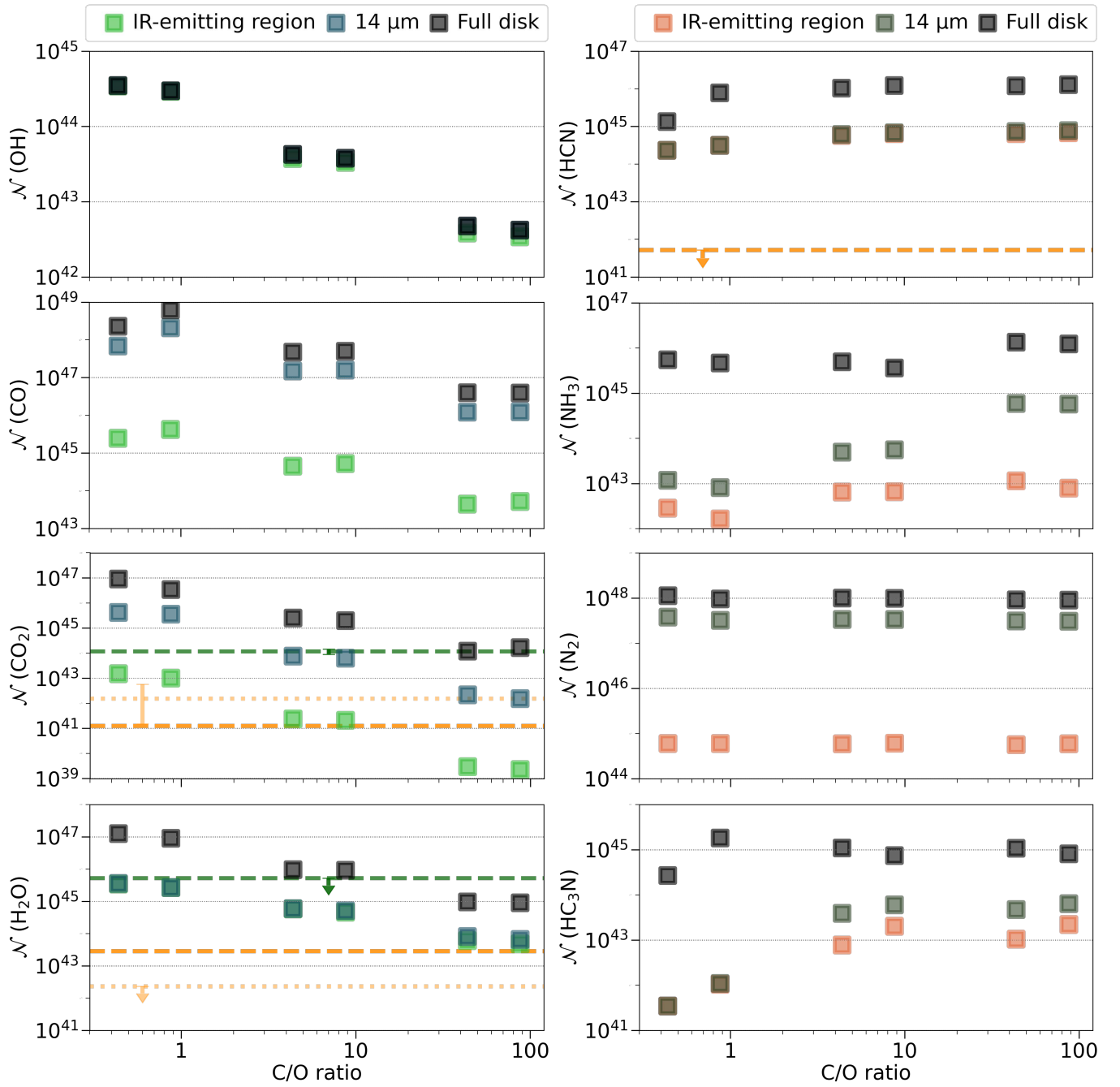


Figure F.2. Same as Fig. F.1, but for the oxygen- and nitrogen-bearing species (OH, CO, CO₂, H₂O, HCN, NH₃, N₂, and HC₃N).

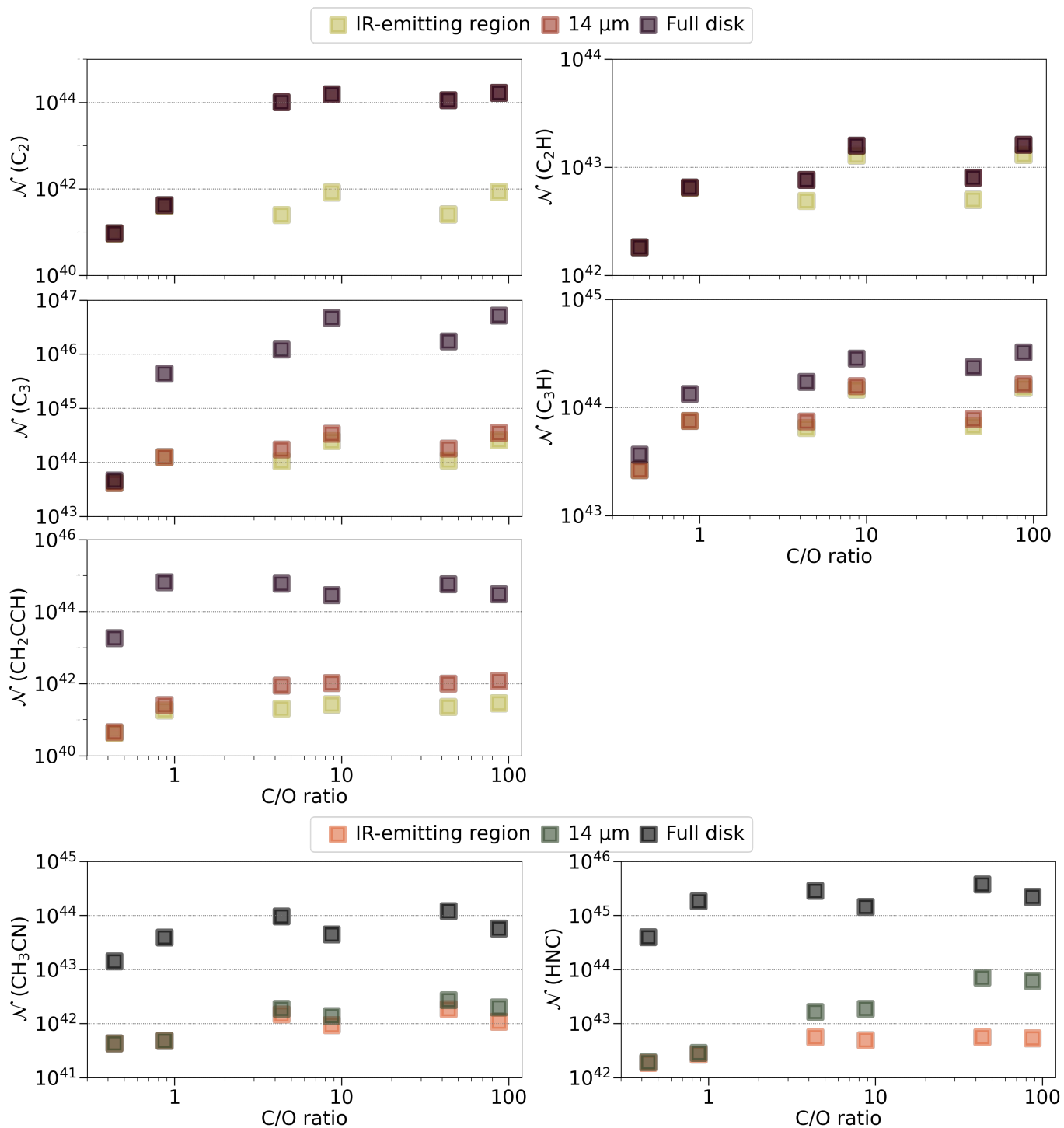


Figure F.3. Same as Fig. F.1, but for the potentially observable species C_2 , C_2H , C_3 , C_3H , CH_2CCH , CH_3CN , and HNC .

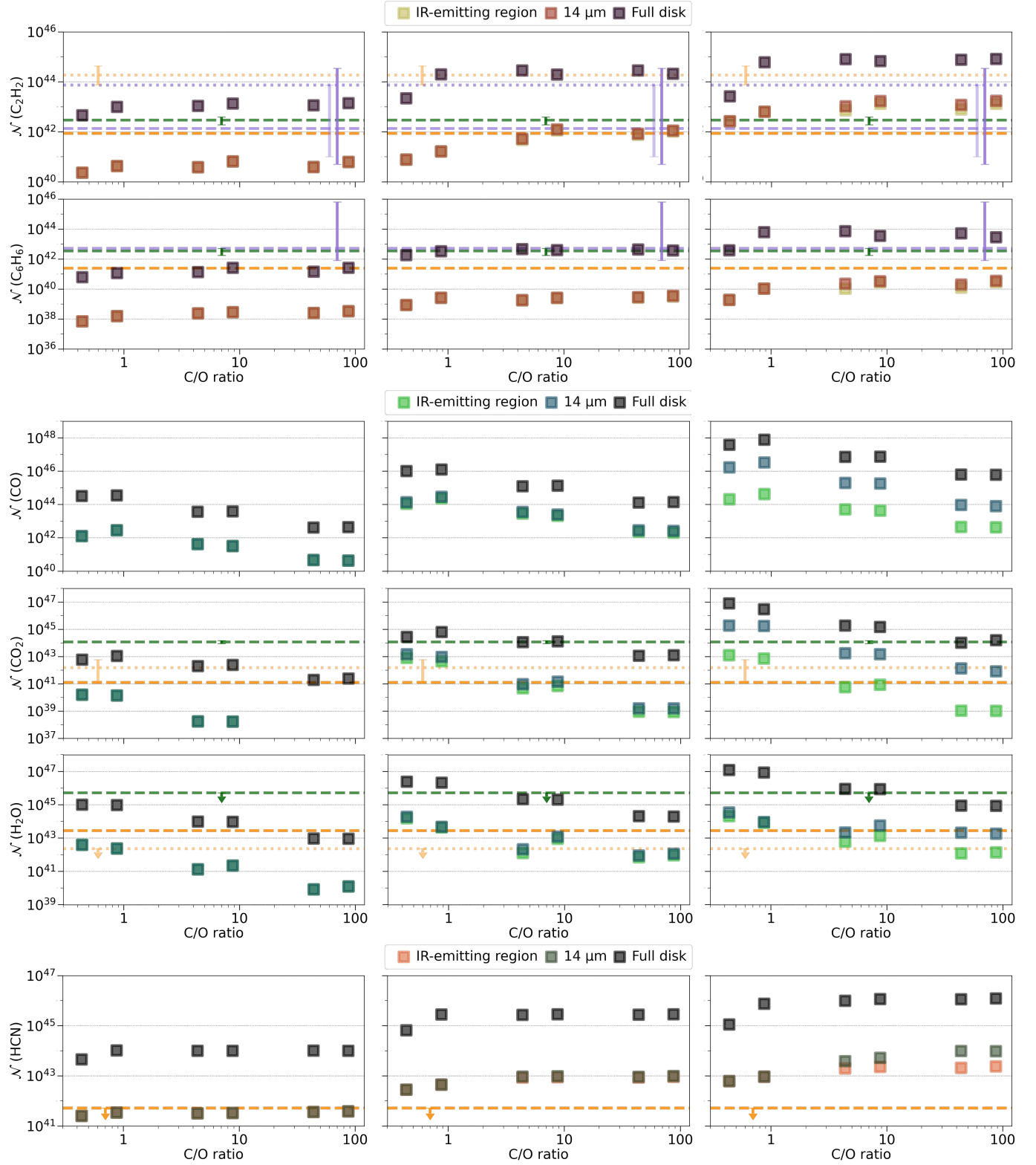


Figure F.4. Same as Figure F.1, but at 0.04 au (left) and averaged over 0.1 (middle) and 1 au (right) for C_2H_2 , C_6H_6 , CO , CO_2 , H_2O , and HCN (each row).

Table 4. Inferred number of molecules for J160532, ISO-ChaI 147, and Sz28.

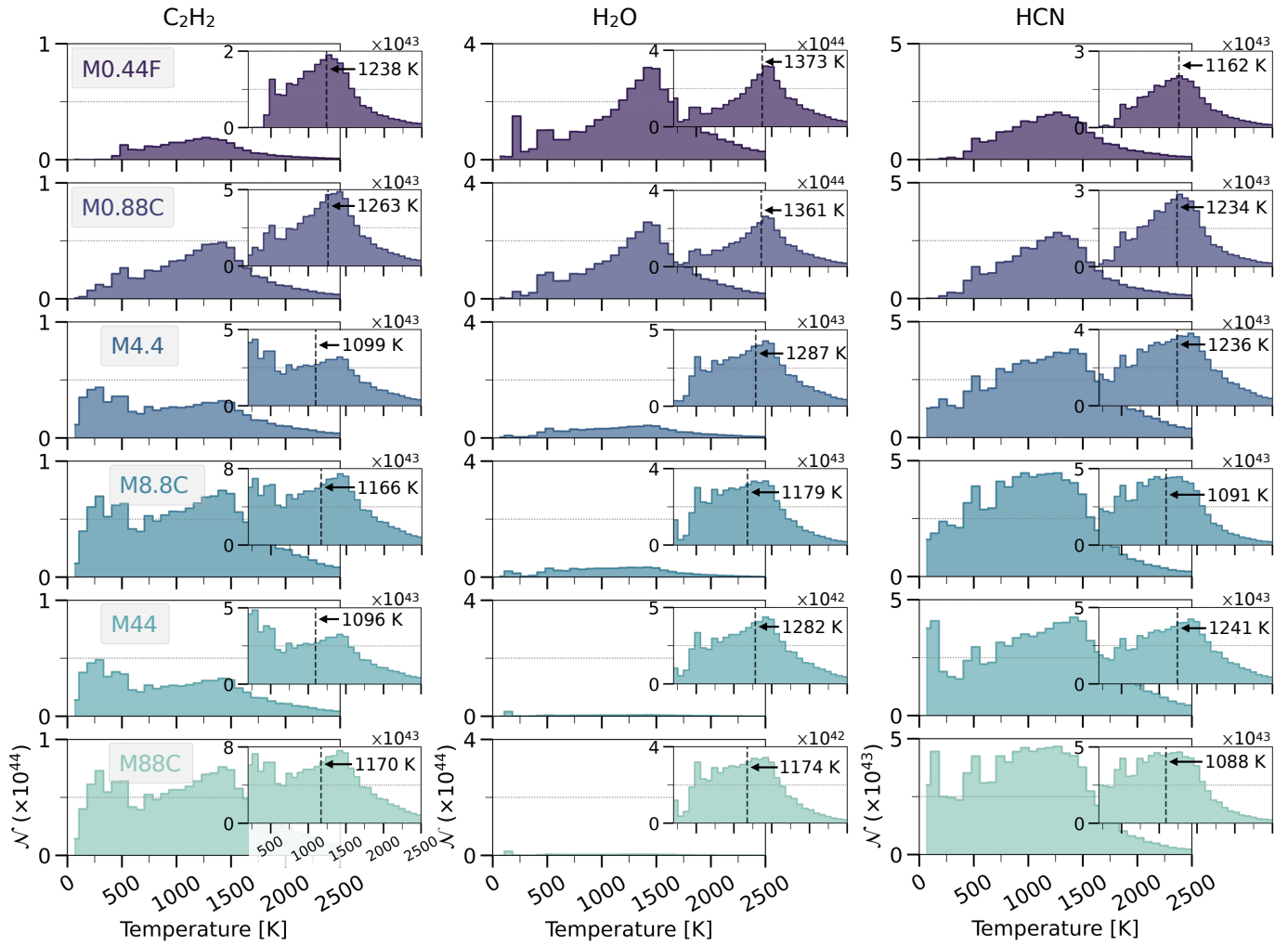
Molecule	Number of Molecules (\mathcal{N})		
	J160532 [1]	ISO-ChaI 147 [3]	Sz28 [4]
Hydrocarbons			
C ₂ H ₂ *	$1.84^{+2.45}_{-1.07} \times 10^{44}$	$1.45 \pm 0.34 \times 10^{46}$	$7.40_{-7.39} \times 10^{43}$
C ₂ H ₂	8.61×10^{41}	$2.90 \pm 0.99 \times 10^{42}$	$1.35^{+343}_{-1.30} \times 10^{42}$
C ₆ H ₆	2.41×10^{41}	$3.45 \pm 1.72 \times 10^{42}$	$5.10^{+6240}_{-4.30} \times 10^{42}$
C ₄ H ₂	2.41×10^{41}	$1.27 \pm 0.20 \times 10^{42}$	$6.75^{+6.08}_{-6.68} \times 10^{40}$
CH ₄ *	–	$1.62 \pm 0.81 \times 10^{47}$	–
CH ₄	5.17×10^{41}	Not detected	Detected
C ₂ H ₄ *	Not detected	$2.14 \pm 0.34 \times 10^{46}$	Not detected
C ₂ H ₄	Not detected	$1.87 \pm 0.30 \times 10^{42}$	Not detected
C ₃ H ₄	Not detected	$2.76 \pm 1.10 \times 10^{42}$	$6.86^{+848}_{-6.10} \times 10^{41}$
C ₂ H ₆	Not detected	Detected	Detected
CH ₃	Not detected	Detected	Detected
Oxygen-bearing Species			
H ₂ O*	$\leq 2.30 \times 10^{42}$	–	Not detected
H ₂ O	2.81×10^{43} [2]	$< 5.12 \times 10^{45}$	Not detected
CO ₂ *	$1.53^{+4.21}_{-1.38} \times 10^{42}$	–	Detected
CO ₂	1.24×10^{41}	$1.17 \pm 0.27 \times 10^{44}$	Detected
Nitrogen-bearing Species			
HCN	$\leq 5.17 \times 10^{41}$	Detected	Detected
NH ₃	Not detected	Not detected	Not detected
HC ₃ N	Not detected	Detected	Detected

NOTE—[1] Tabone et al. (2023); [2] Arabhavi et al. (2025b); [3] Arabhavi et al. (2024); and [4] Kanwar et al. (2024b). Optically thick values are indicated by the asterisk on the species named.

Table 5. Properties of the Low-mass Stars, J160532, ISO-ChaI 147, and Sz28.

Parameter	Description	Value		
		J160532	ISO-ChaI 147	Sz28
M_{\star} (M_{\odot})	Stellar mass	0.14	0.11	0.12
L_{\star} (L_{\odot})	Stellar luminosity	0.04	0.03	0.04
\dot{M} ($M_{\odot} \text{ yr}^{-1}$)	Accretion mass rate	7.9×10^{-10}	7×10^{-12}	1.8×10^{-11}
Age _∗ (Myr)	Stellar age	2.6 ± 1.6	1 – 2	3.5
SpT	Spectral type	M4.75	M5.5	M5.5
M_{grain} (M_{\oplus})	Dust grain disk mass	0.75	< 0.72	0.48
M_{gas} (M_{Jup})	Gas disk mass	< 0.2	< 1.05	0.08

NOTE—Physical properties of the J160532 (Pascucci et al. 2013; Tabone et al. 2023), ISO-ChaI 147 (Arabhavi et al. 2024), and Sz28 star-disk systems (Kanwar et al. 2024b).



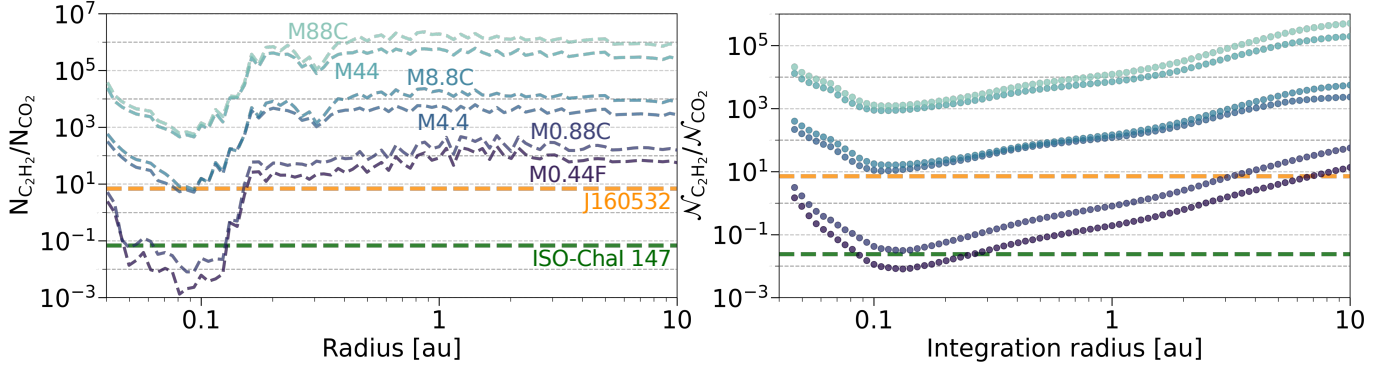


Figure I.1. Left: column density ratio for $\text{C}_2\text{H}_2/\text{CO}_2$ as a function of radius. Right: total number of molecule ratios up to a fixed integration radius (shown on the x -axis), where each circle represents an integration step. Both panels consider the IR-emitting region. The different colors represent the different C/O ratios. The horizontal dashed orange and green lines represent the number of molecule ratios from the results reported by Tabone et al. (2023) and Arabhavi et al. (2024), respectively.

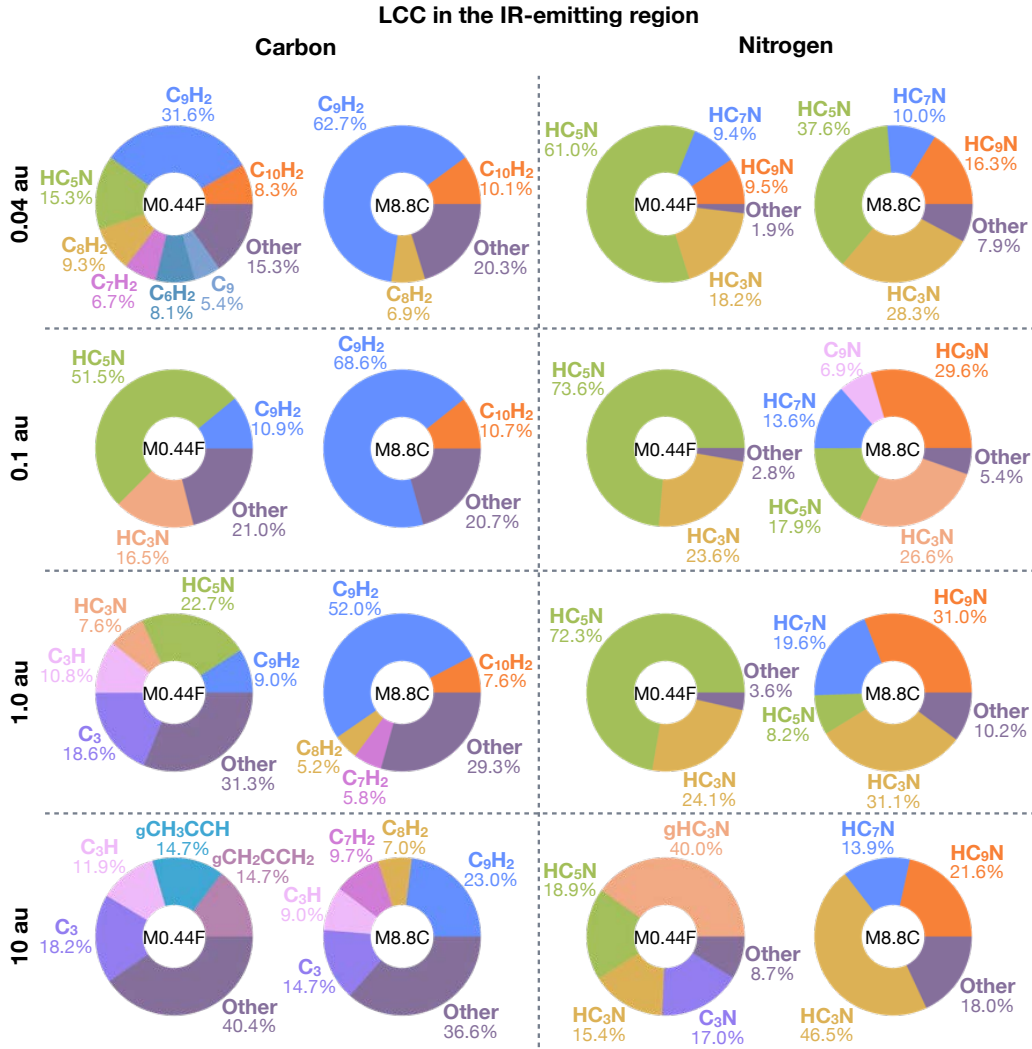


Figure J.1. Pie charts showing the contribution of LCCs by molecular mass to the LCC category in the carbon (left) and nitrogen (right) budgets for the same models (M0.44F and M8.8C) and integrations radii (0.04, 0.1, 1.0, and 10 au) as those in Fig. 10.

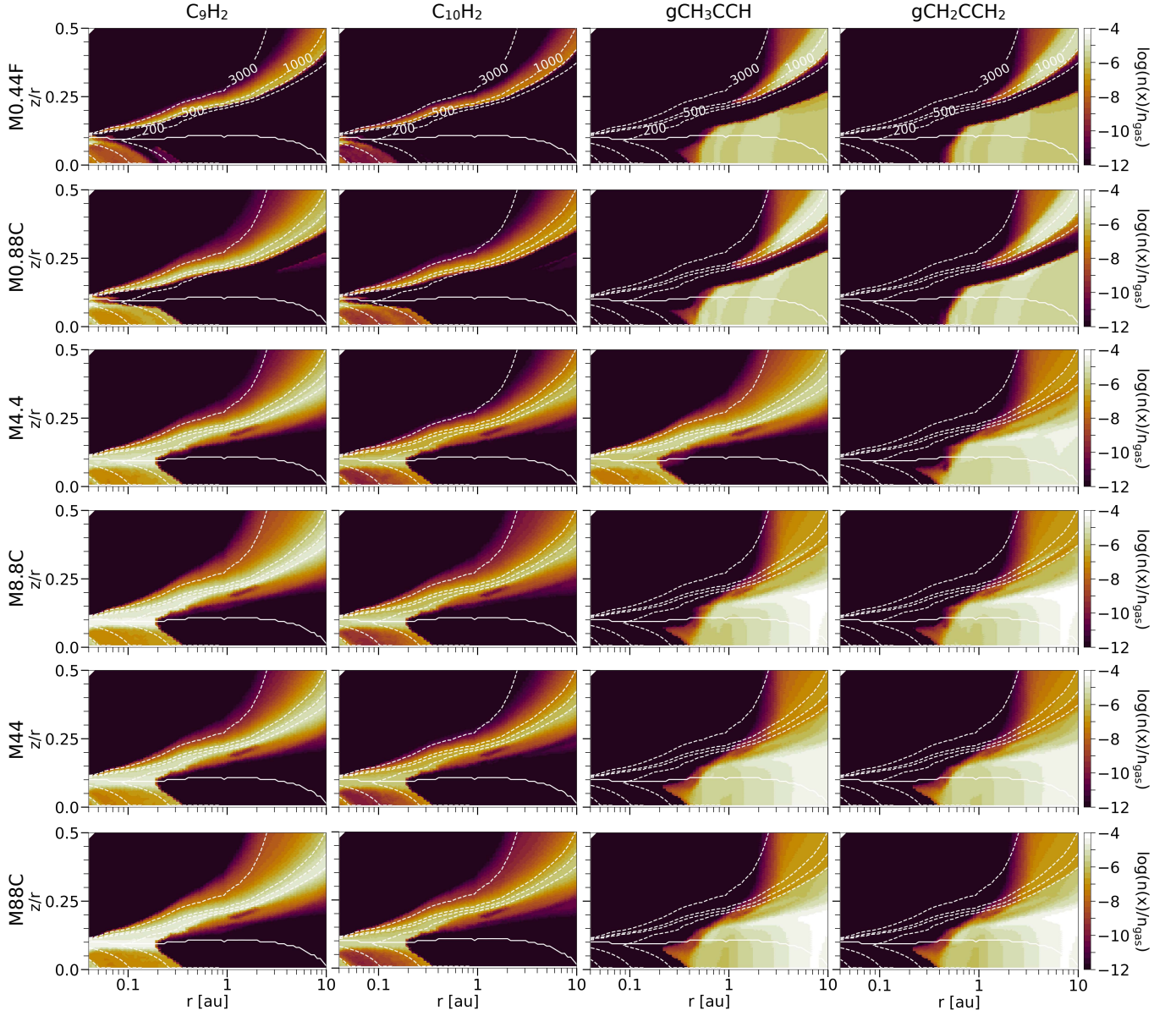


Figure J.2. Same as Fig. 2, but for the LCCs C_9H_2 , $C_{10}H_2$, CH_3CCH ice, and CH_2CCH_2 ice.

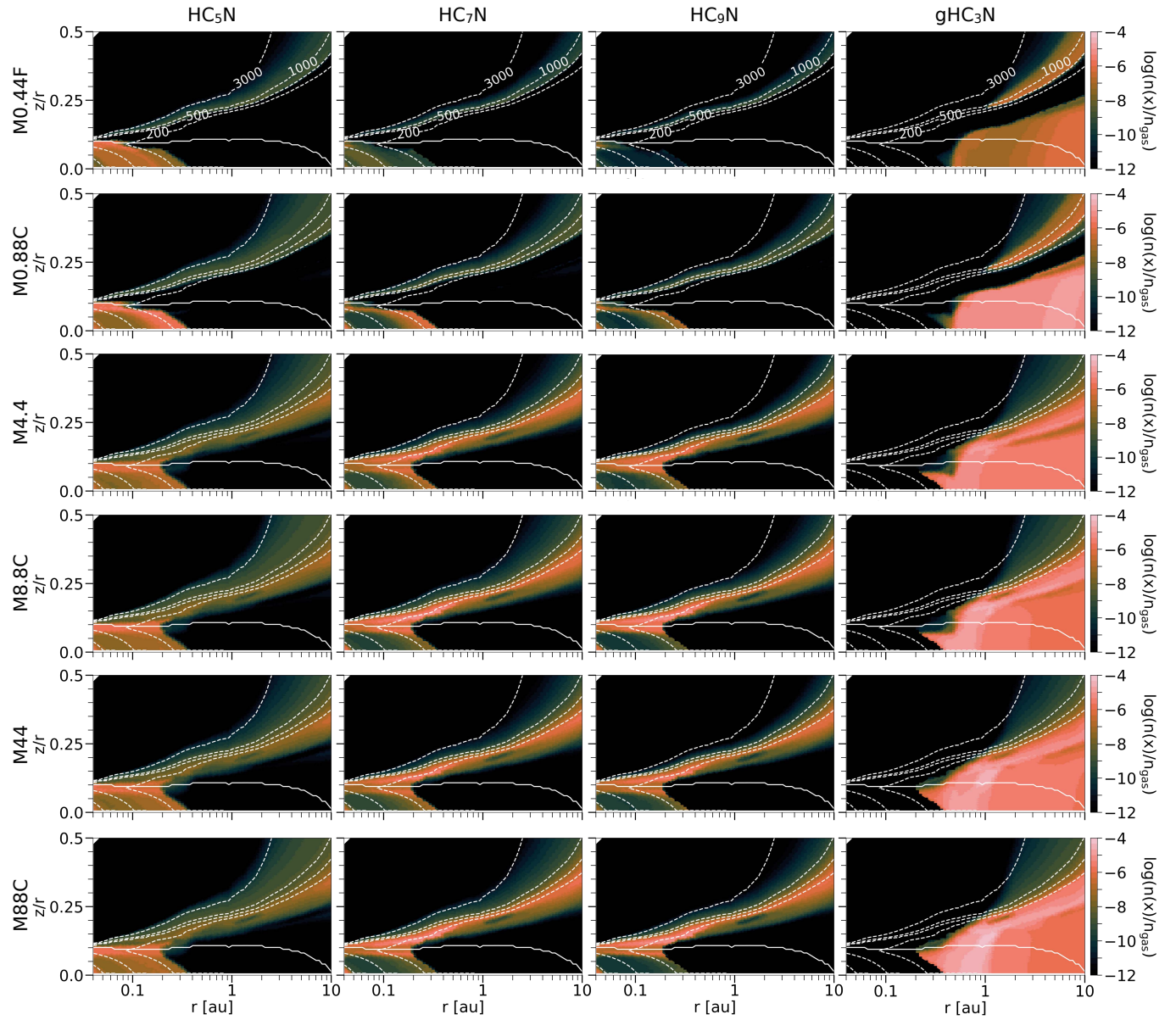


Figure J.3. Same as Fig. 2, but for the LCCs HC₅N, HC₇N, HC₉N, and HC₃N ice.

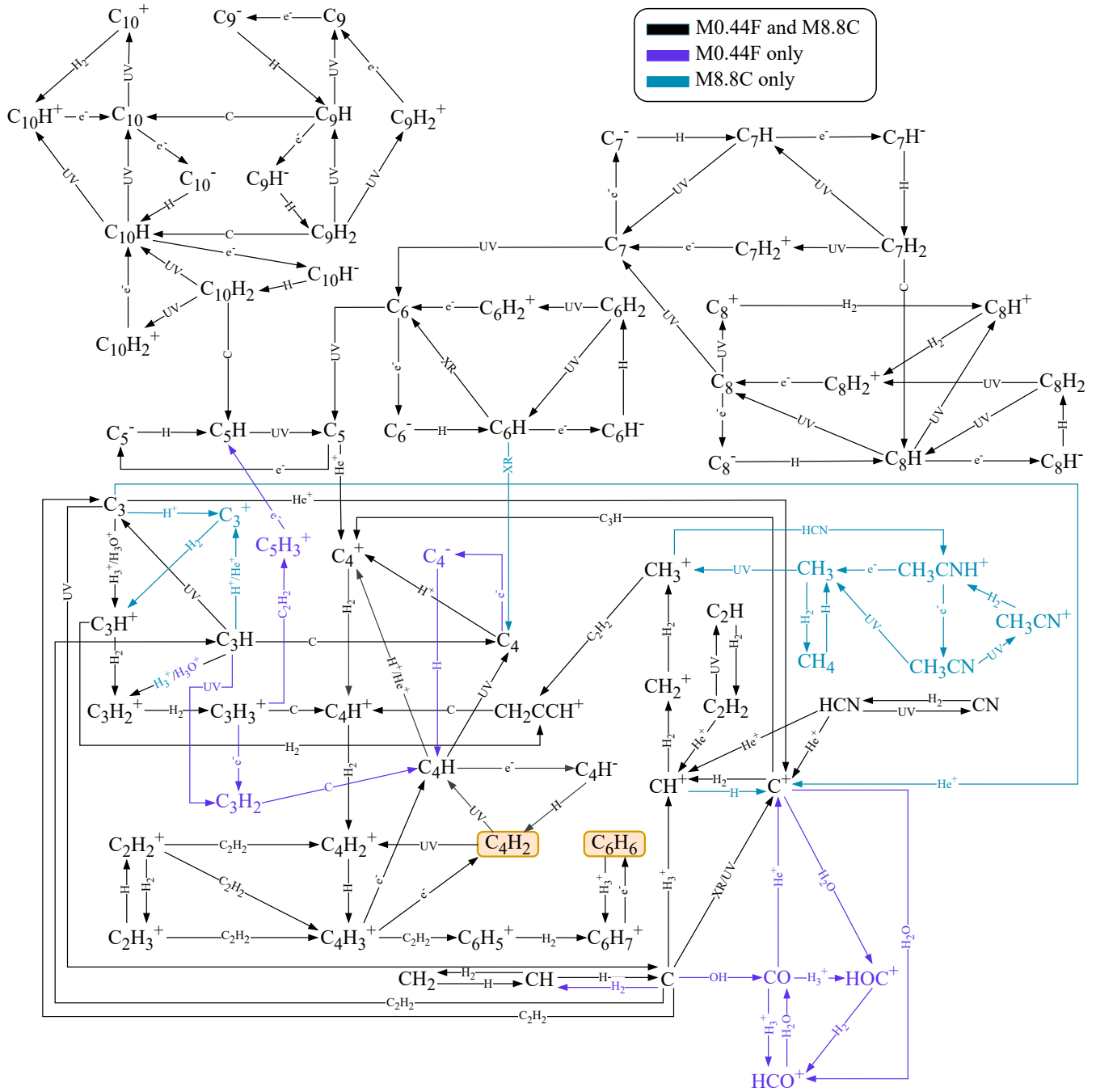


Figure K.1. Main gas-phase formation pathways for C_6H_6 and C_4H_2 at $r = 1$ au and $z/r = 0.23$ in the oxygen-rich and carbon-rich models, M0.44F and M8.8C, respectively. Purple and turquoise lines represent those reactions only dominant in the M0.44F and M8.8C models, respectively. Black lines represent the main formation reactions for both models.